[American Journal of Science, Vol. 304, October/November, 2004, P. 752–810]

AN EQUATION OF STATE FOR SILICATE MELTS. III. ANALYSIS OF STOICHIOMETRIC LIQUIDS AT ELEVATED PRESSURE: SHOCK COMPRESSION DATA, MOLECULAR DYNAMICS SIMULATIONS AND MINERAL FUSION CURVES

MARK S. GHIORSO

Department of Geophysical Sciences, The University of Chicago, 734 S. Ellis Avenue, Chicago, Illinois 60637; ghiorso@geosci.uchicago.edu

ABSTRACT. Experimental data and molecular dynamics simulations that constrain the densities of liquids of "mineral-like" stoichiometry at elevated pressure are evaluated using the liquid Equation of State (EOS) of Ghiorso (2004a). Phase equilibrium constraints on melt density are developed from experimental brackets on mineral fusion curves, specifically congruent melting of albite, anorthite, cristobalite/quartz/stishovite, diopside, enstatite, fayalite, forsterite, jadeite, nepheline, pyrope, sanidine, and titanite. A self consistent thermodynamic analysis of shock compression is applied to experimentally determined brackets on the Hugoniot for the liquid compositions $CaMgSi_2O_6$, $CaAl_2Si_2O_8$, Fe_2SiO_4, and $(CaMgSi_2O_6)_{0.64}(CaAl_2Si_2O_8)_{0.36}$. Molecular dynamics (MD) simulations of both melt density and melt structure are analyzed utilizing the liquid EOS of Ghiorso (2004a) and an ideal associated solution model that accounts explicitly for the effect of pressure and temperature on the oxygen coordination environment of silicon and aluminum. MD data on $Mg_2Si_2O_6$, $CaMgSi_2O_6$, SiO_2, $Na_2Si_4O_9$, $CaAl_2Si_2O_8$, $NaAlSiO_4$, $NaAlSi_2O_6$, and $NaAlSi_3O_8$ liquids are considered in conjunction with the fusion curve and shock compression experimental data sets. An internally consistent assessment of liquid EOS parameters from all available data sources is attempted for each liquid composition considered. Shock compression experiments on more chemically complex liquids of komatiite and MORB bulk composition are also examined.

In support of the analysis of mineral fusion curves, volumetric properties as a function of temperature and pressure of diopside, enstatite (both *Pbca* and *C2/c*), fayalite, forsterite, and pyrope are evaluated from literature data. Experimental observations are parameterized to a Universal EOS (Vinet and others, 1986, 1987, 1989).

It is found that the reference pressure properties derived by Ghiorso and Kress (2004) are internally consistent with the majority of high-pressure constraints on melt density. The notable exceptions are molten SiO_2 and melts in the system MgO-SiO_2. For the latter system, the calibration of Ghiorso and Kress (2004) fails to recover reference pressure volumes.

The effect of configurational collapse (the volumetric response associated with changes in melt structure, such as changing oxygen coordination number about a cation) is systematically assessed from molecular dynamics simulation data. Fully depolymerized melts exhibit an ~11 percent density increase associated with Si and Al transforming from IV- to V-fold coordination with respect to oxygen. Alkali aluminosilicate melts demonstrate ~27 percent increase in melt density and SiO_2 and $Na_2Si_4O_9$ liquids show a density increase of ~17 percent.

INTRODUCTION

This paper is the third in a four part series aimed at describing the development and calibration of a new Equation of State (EOS) for multicomponent silicate liquids. The objective is a predictive model equation for the volumetric properties of magmatic composition silicate melts that is applicable over the temperature and pressure regime of the Earth's upper mantle. The first paper in the series (Ghiorso, 2004a; hereafter Part I) deals with the functional form of the proposed EOS and with application of the EOS to liquids that undergo continuous structural transformation with temperature

and pressure. The second paper in this series (Ghiorso and Kress, 2004; hereafter Part II) develops a model calibration at the reference pressure. In this paper, the suitability of the EOS is demonstrated for modeling high-pressure shock wave experiments, for parameterizing molecular dynamics simulations of melt density and structure, and for thermodynamic analysis of experimental data on mineral fusion curves. The final paper in the series (Ghiorso, 2004b; hereafter Part IV) deals with mixing relations of high-pressure EOS parameters and with the analysis of experimental sink-float density estimates at elevated pressures and temperatures in combination with the data sets discussed here.

While the analysis of shock wave data and molecular dynamics simulations provides direct constraints on EOS parameters, the modeling of mineral fusion curves requires additional information including an appropriate EOS for the solid phase and an assessment of the energetics of the solid-liquid transformation along the reference isobar. To support this modeling exercise, parameterizations of the Universal EOS (Vinet and others, 1986, 1987, 1989) are developed below for a number of minerals relevant to the fusion curve analysis.

There are two primary reasons for undertaking here a systematic assessment of data on the shock compression and molecular dynamics of melts and on the melting behavior of minerals at elevated pressure. Firstly, it is important to establish that the functional form of the proposed EOS is flexible enough to model these data sets, and by focusing on liquids of simple mineral like stoichiometry taken to high pressure, the opportunity is afforded to examine a wide range of compression behaviors. Secondly, as these data sets constitute important constraints for calibration of a multicomponent mixing model for the high-pressure parameters of the proposed EOS (the subject of Part IV), it is imperative that the merit and internal consistency of each data source be evaluated prior to combining the data sets to derive a final model. In this context it is especially important to understand the systematics of variation of melt structure with composition so that the configurational contribution (Part I) to the volumetric properties can be properly assessed. Without this understanding the combined mixing model will tend to accommodate data inconsistencies and structural effects on melt density by attributing both falsely to compositional variation or the effects of temperature and pressure, resulting in a spurious calibration.

CONSTRAINTS ON VOLUMETRIC PROPERTIES AT HIGH PRESSURE

There are four major kinds of constraints on the volumetric properties of silicate liquids at pressures above ambient conditions. First, there are direct estimates of melt density obtained from experimental determinations of mineral buoyancy. These experiments are commonly referred to as sink-float experiments, and melt density is constrained relative to a known EOS for the mineral. Second, there are direct determinations of melt density from shock compression measurements. Third, there are estimates of melt density and derivative thermodynamic properties computed from molecular dynamics simulations. These data sets also provide information on microscopic melt structure that can be correlated to variation in macroscopic bulk properties. And fourth, there are indirect constraints on melt density obtained from thermodynamic analysis of mineral fusion curves.

The majority of mineral-liquid sink-float experiments have been performed on basaltic or ultramafic bulk compositions. With the exception of the work by Agee (1992a, 1992b) on molten Fe_2SiO_4 liquid, these data sets will be analyzed in Part IV. The emphasis in this paper is on the remaining three sources of data identified above. In the next few subsections analysis methods and procedures are developed for applying the liquid EOS to each of the data types examined in this paper.

Analysis of Shock Compression Measurements

Experimental results from shock compression studies on silicate liquids of composition $CaMgSi_2O_6$ and $CaAl_2Si_2O_8$ are reported by Rigden and others (1989), on liquid Fe_2SiO_4 by Chen and others (2002), and on mixed liquids of composition $(CaMgSi_2O_6)_{0.64}$-$(CaAl_2Si_2O_8)_{0.36}$ by Rigden and others (1984, 1988). Miller and others (1991) report shock compression data for a multicomponent silicate melt of komatiitic composition. Data for a MORB-composition liquid are provided by Rowan (ms, 1993).

A Hugoniot[1] establishes a relation between pressure and density for the dynamic conditions that ideally characterize the shock experiment. Measured values of the shock (v_s) and particle (v) velocity can be directly converted to estimates of density (ρ) and pressure (P) by application of mass and momentum conservation equations (Hugoniot, 1889; Anderson, 1989):

$$\rho_0 v_s = \rho(v_s - v) \tag{1}$$

$$P = \rho_0 v_s v \tag{2}$$

where the subscript zero denotes the initial conditions of the experiment. Application of the principle of conservation of energy provides an additional relation (Anderson, 1989)

$$Pv = \rho_0 v_s \left(\frac{1}{2} v^2 + e - e_0\right) \tag{3}$$

which can be written with the aid of equations (1) and (2) entirely in terms of thermodynamic quantities

$$e - e_0 = \frac{1}{2}(P - P_0)\left(\frac{1}{\rho_0} - \frac{1}{\rho}\right) \tag{4}$$

or more conveniently as

$$\hat{E} - \hat{E}_0 = \frac{1}{2} MW(P - P_0)\left(\frac{1}{\rho_0} - \frac{1}{\rho}\right) \tag{5}$$

where e refers to the specific internal energy, MW is the molar mass, and $\hat{E}$ is the corresponding molar internal energy. The molar internal energy can in turn be calculated from an equation of state. Starting from the thermodynamic identity,

$$d\hat{E} = Td\hat{S} - Pd\hat{V} \tag{6}$$

where T is the absolute temperature, $\hat{S}$ is the molar entropy and $\hat{V}$ is the molar volume, the first partial derivatives of the internal energy with respect to temperature and pressure are readily derived

$$\frac{d\hat{E}}{\partial T} = T\frac{\partial \hat{S}}{\partial T} - P\frac{\partial \hat{V}}{\partial T} = \hat{C}_P - P\hat{V}\alpha \tag{7}$$

$$\frac{\partial \hat{E}}{\partial P} = T\frac{\partial \hat{S}}{\partial P} - P\frac{\partial \hat{V}}{\partial P} = -T\frac{\partial \hat{V}}{\partial T} - P\frac{\partial \hat{V}}{\partial P} = -T\hat{V}\alpha + P\hat{V}\beta \tag{8}$$

[1] For H. Hugoniot. Shock compression drives material to a point on the principal Hugoniot, which is the locus of all final states characterized by (ρ,P,T) that can be achieved by a single shock wave passing through the material of interest.

In equations (7) and (8) $\hat{C}_P$, α, and β are the molar heat capacity, the coefficient of thermal expansion and the compressibility, respectively. Integrating equation (7) along the reference isobar and equation (8) along the final isotherm gives an expression for the change in internal energy

$$\hat{E} - \hat{E}_0 = \int_{T_0}^{T} \hat{C}_{P_0} dT - P_0 \int_{T_0}^{T} \hat{V}_{P_0} \alpha_{P_0} dT - T \int_{P_0}^{P} \hat{V} \alpha dP + \int_{P_0}^{P} P \hat{V} \beta dP \tag{9}$$

or equivalently

$$\hat{E} - \hat{E}_0 = \int_{T_0}^{T} \hat{C}_{P_r} dT + \int_{P_0}^{P} \hat{V}(1 - T\alpha) dP + P_0 \hat{V}_{T_0,P_0} - P\hat{V} \tag{10}$$

The shock Hugoniot curve may be calculated by simultaneous solution of the pair of expressions

$$\rho = \frac{MW}{\hat{V}} \tag{11}$$

and

$$\frac{1}{2} MW(P - P_0)\left(\frac{1}{\rho_0} - \frac{1}{\rho}\right) = \int_{T_0}^{T} \hat{C}_{P_0} dT + \int_{P_0}^{P} \hat{V}(1 - T\alpha) dP + P_0 \hat{V}_{T_0,P_0} - P\hat{V} \tag{12}$$

obtained by combining equations (5) and (10), where $\hat{V}$ is a function of T and P and is modeled by an EOS formulation. This calculation depends only on the EOS and reference pressure heat capacity. The temperature of the shock is calculated implicitly in the course of solution (Yoneda, 1996).

The usual method of interpreting shock measurements for the purposes of EOS calibration is to transform the Hugoniot to an adiabat (isentrope) using an EOS formulation that avoids explicit reference to temperature (T), such as Mie-Grüneisen theory[2]. Once the isentrope is obtained, results are typically parameterized with a third-order Burch-Murnaghan EOS. The extracted parameters (K_S, the isentropic bulk modulus, and K'_S, its pressure derivative) are then converted to isothermal equivalents utilizing ancillary data (for example, reference pressure thermal expansion, α; isochoric heat capacity, C_V; *et cetera*). Finally shock temperatures are calculated by combining the extracted isothermal bulk modulus (K) and its pressure derivative (K') with another EOS formulation that affords estimation of temperatures (Duffy and Wang, 1998). As a consequence of this multi-step procedure, the resultant estimates of shock temperatures are not necessarily internally consistent with any one EOS expression. In particular reported (P, ρ, T) – tuples may not be used as calibrants for parameterizing a different EOS then those employed in the various stages of data reduction.

[2] An equation that "relates the difference in pressure at fixed volume between the initial low temperature and a high temperature state of specified thermal energy: $P - P_0 = \frac{\gamma}{V}(E - E_0)$" (Anderson, 1989,p 101). γ is the Gruneisen parameter $\left(\equiv \frac{\alpha K_T}{\rho C_V}\right)$, and the pressure along the adiabat is given by $P_S = P\left[1 - \frac{\gamma}{2}\left(\frac{V}{V_0} - 1\right)\right] - \frac{\gamma}{V}\int_{V_c}^{V} P_S dV$ (Anderson, 1989).

Inconsistencies associated with the reduction of Hugoniot data via a combination of EOS formulations can be avoided if a single, temperature-explicit equation of state is utilized in the analysis. Adopting the EOS proposed in Part I,

$$V = \frac{V_0 + (V_1 + V_0 a)(P - P_r) + \left(\frac{V_2}{2} + V_1 a + V_0 b\right)(P - P_r)^2}{1 + a(P - P_r) + b(P - P_r)^2} \tag{13}$$

along with reference pressure parameters calibrated in Part II (V_0, V_1), shock compression data sets may be evaluated. Noting that a and b in equation (13) are functions of the second (V_2), third (V_3) and fourth (V_4) order derivatives of volume with respect to pressure (for example,

$$a = \frac{V_2 V_3 - \frac{1}{2} V_1 V_4}{2V_1 V_3 - 3V_2^2} \tag{14}$$

$$b = \frac{\frac{1}{4} V_2 V_4 - \frac{1}{3} V_3^2}{2V_1 V_3 - 3V_2^2} \tag{15}$$

Part I), the parameters V_2, V_3, and V_4 may be fitted utilizing equations (11) and (12) from the (P, ρ)-data sets to model shock Hugoniots.

Analysis of Phase Equilibrium Constraints from Mineral Fusion Curves

Thermodynamic analysis of mineral fusion curves has been the subject of numerous studies (Morse, 1980, chapter 18; Richet and others, 1982; Bottinga, 1985; Richet and Bottinga, 1986; Herzberg, 1987a, 1987b; Lange and Carmichael, 1987, 1990; Kress and others, 1988; Walker and others, 1988; Agee, 1998; Anovitz and Blencoe, 1999; Lange 2003). The procedures adopted here are based on this previous work.

If a mineral melts congruently to a liquid at some specified T and P, the Gibbs free energy change associated with the melting reaction is given by[3]

$$\Delta G^o = 0 = \Delta H^o_{P_r} - T\Delta S^o_{P_r} + \int_{P_r}^{P} V^{liq} dP - \int_{P_r}^{P} V^{sol} dP \tag{16}$$

where $\Delta H^o_{P_r}$ is the enthalpy change of the reaction at T along the reference isobar (P_r),

$$\Delta H^o_{P_r} = T_{fus}\Delta S^{o,fus}_{T_{fus},P_r} + \int_{T_{fus}}^{T} C^{liq}_{P_r} dT - \int_{T_{fus}}^{T} C^{sol}_{P_r} dT \tag{17}$$

and $\Delta S^o_{P_r}$ is the entropy change of the reaction under the same conditions

$$\Delta S^o_{P_r} = \Delta S^{o,fus}_{T_{fus},P_r} + \int_{T_{fus}}^{T} \frac{C^{liq}_{P_r}}{T} dT - \int_{T_{fus}}^{T} \frac{C^{sol}_{P_r}}{T} dT \tag{18}$$

In equations (17) and (18), $C^{phase}_{P_r}$ is the heat capacity of the phase, T_{fus} is the fusion temperature, and $\Delta S^{o,fus}_{T_{fus},P_r}$ is the entropy of fusion, all evaluated at the reference

[3] The superscript zero denotes the standard state, which for this paper is taken to be unit activity of the pure solid or the pure liquid at any T and P.

pressure. The volume integrals in equation (16) require an EOS for both the liquid and the solid. The integral is evaluated for the proposed liquid EOS in Part I (equations A-24 through A-28). In most work on fusion curves, a third order Birch-Murnaghan EOS is adopted for the solid. In this paper, the Universal EOS of Vinet and coworkers (Vinet and others, 1986, 1987, 1989) is utilized instead. The Universal EOS has the form

$$P = \frac{3K(1-x)e^{\eta(1-x)}}{x^2} + \alpha K(T - T_r) \tag{19}$$

where η and x are defined as

$$\eta = \frac{3}{2}(K' - 1) \tag{20}$$

and

$$x = \left(\frac{V}{V_0}\right)^{1/3} \tag{21}$$

In these expressions V_0 is the reference volume, α is the coefficient of thermal expansion, K is the bulk modulus, and K' is its pressure derivative, all at zero pressure and temperature T_r. The required integral of the Universal EOS (19) is evaluated by parts,

$$\int_{P_r}^{P} VdP = PV - P_rV_{P_r} - \int_{V_{P_r}}^{V} PdV \tag{22}$$

to give

$$\int_{P_r}^{P} V^{sol}dP = PV - P_rV_{P_r} + \frac{9V_0K}{\eta}[(1-x)e^{\eta(1-x)} - (1-x_{P_r})e^{\eta(1-x_{P_r})} - (T - T_r)K\alpha(V - V_{P_r}) \tag{23}$$

where $x_{P_r} = \left(\frac{V_{P_r}}{V_0}\right)^{1/3}$.

Experimental data on mineral fusion curves typically take the form of all-liquid or all-solid brackets on the *P-T* conditions of melting. These are typically referred to as bound constraints on the melting curve. More rarely, mixed liquid-solid assemblages are documented experimentally. These are referred to in this paper as reversal constraints. The fitting of liquid EOS parameters to data sets of this kind is best accomplished by constructing a least squares function that simultaneously minimizes the departure from the equilibrium condition (16) for the reversal constraints while maintaining feasibility of the bound constraints, imposing a penalty function that raises the sum-of-squares when these constraints are violated. In this paper, a penalty function is adopted that corresponds to the square of the calculated free energy change of the right-hand-side of equation (16) when the sign of this quantity indicates stability of the incorrect phase at the *P-T* conditions of the bracket. Estimated errors on the *P-T* coordinates of the bound and reversal constraints are accounted for by weighting with the inverse standard deviation of the temperature measurement, if this quantity is reported. Fusion curves are calculated by solving equation (16) for T iteratively at fixed pressure.

Analysis of Data from Molecular Dynamics Simulations

Molecular dynamics (MD) simulations provide a means of computing thermodynamic and structural properties of a system. Typically, MD calculations generate estimates of T, P, ρ, E, the isochoric heat capacity (C_V), K and α as well as some measure of the geometric organization of atoms, such as bond lengths, bond angles, nearest neighbor coordination numbers, *et cetera*. These quantities are calculated using methods of statistical mechanics from an equilibrium ensemble average of the positions and momenta of atomic particles. The inter-atomic forces are modeled using either first principles quantum mechanics-based methods or classical potential theory. Once forces between the atoms are specified the system evolves following Newton's laws of motion for a brief time step, the forces are recomputed, the atoms displaced again according to Newton's laws, and the process repeated until the system reaches an equilibrium state. The vast majority of MD simulations of silicate melts are based on a classical description of atomic forces, which is primarily motivated by the desire to do the calculations with large numbers of particles (~10,000 – 100,000 atoms) in a reasonable amount of computer time. Large ensemble size is necessary in order to achieve accurate structural characteristics and thermodynamic properties in complex chemical systems, especially when one or more components are dilute. As is demonstrated below, modern MD simulation work with classical inter-atomic potentials generates estimates of melt density of comparable quality to traditional experimental methods like shock compression and sink-float experiments.

Not all MD studies on silicate melts provide data that are suitable to constrain an EOS model parameterization. Many studies fail to report melt density, while others do so but neglect to report an estimate of T or $\hat{E}$. From the perspective of EOS calibration, the most useful MD work takes the form of a systematic T-P-grid of calculations with at least the density and some measure of melt structure reported at each grid point. Melt structure can be described in various ways and generally takes the form of a radial distribution function (RDF) – a description of the likelihood of finding an atom at some distance about another atom. The RDF can be made more specific by computing the pair distribution function (PDF) which focuses on the probability of finding a particular kind of atom (say O) at some distance about another (say Si). Optimally, the most useful measure of the structure is a complete counting and geometric description of the nearest neighbor coordination polyhedra; one way to perform this analysis is by a method called Voronoi tessellation (Allen and Tildesely, 1987), and the technique has been applied quite successfully to molten SiO_2 by Rustad and others (1991a). In principle, from such a description the configurational entropy can be calculated for the assemblage. In practice, some averaging of the diversity of polyhedra is made and the liquid is often described in terms of the predominance of a particular kind of atom with a certain number of nearest neighbors of another kind. This quantity is referred to as the coordination number (CN). For example, the number of nearest O neighbors about a Si may be four (CN = IV), five (CN = V) or higher, or some mixture of coordination states. What is lost in the coordination number description of melt structure is the different geometric configurations that are consistent with a given CN. Ignoring this variation discards configurations and under predicts the entropy, but the effects are likely to be of second order if bond covalency dictates specific geometrical arrangements for a given CN. For example, the coordination of four oxygens around silicon predominantly gives rise to tetrahedral geometrical arrangements in molten SiO_2 and only a minor fraction of planar or more irregular arrangements (Rustad and others, 1991a). By contrast, the number of geometrical arrangements of equal probability of seven and eight-fold coordinated Si in molten SiO_2 at very high pressure (~100 GPa, Rustad and others, 1991a) is great enough to seriously compromise an entropic description solely in terms of Si-O CN. Nevertheless, as a first order measure of melt

structure, CN is a robust descriptor that can be correlated to variation in bulk macroscopic thermodynamic properties like density for IV-, V-, and VI-CN Si in molten SiO_2 (for example, Part I).

The effect of CN changes on the density of silicate melts has been argued from experimental measurements on certain Ti-rich silicate liquids (for example, Dingwell, 1992; Liu and Lange, 2001) and can be quantitatively assessed from MD studies on molten SiO_2 (Rustad and others, 1990, 1991a, 1991b), $Na_2Si_4O_9$ liquid (Diefenbacher and others, 1998), molten $CaAl_2Si_2O_8$ (Nevins and Spera, 1998; Morgan and Spera, 2001a, 2001b), and liquids in the system $NaAlO_2$-SiO_2 (Stein and Spera, 1995, 1996; Bryce and others, 1997, 1999). As noted in Part I, a thermodynamic model can be developed that explicitly partitions the volumetric contributions associated with configurational changes in melt structure from the volumetric changes in T and P attributable to an "isostructural" material (that is, a metastable liquid with fixed CN). This latter contribution is termed here the *vibrational* component of the Gibbs free energy of solution. The liquid EOS is taken to describe the pressure dependence of the vibrational energy while the configurational contribution derives from the entropy of mixing (Part I). A thermodynamic model for the liquid is constructed by generalizing these concepts utilizing the formalism of Tanaka (2000). The Gibbs free energy of solution is separated into configurational (G^{conf}) and vibrational (G^{vib}) contributions

$$G = G^{conf} + G^{vib} \tag{24}$$

The configurational part is written as an entropy of mixing of stoichiometric units of different coordination number

$$G^{conf} = n^{CN} RT \sum_{CN} X^{CN} \ln X^{CN} \tag{25}$$

where X^{CN} is the mole fraction of a liquid component in coordination state CN, and n^{CN} is the multiplicity factor for the system. For example, consider SiO_2 liquid with Si in IV, V and VI CN with respect to O. The system can be thought of as a mixture of $Si^{IV}O_2$, $Si^{V}O_2$, and $Si^{VI}O_2$ species and a mole fraction of SiO_2 can be defined for the fraction of SiO_2 with Si in each CN. The multiplicity factor in this case is one, as there is one Si per formula unit. By contrast, consider molten $CaAl_2Si_2O_8$. Nevins and Spera (1998) have determined that to an excellent approximation Al and Si share similar O CN's in this liquid, so again considering only IV-, V- and VI-fold coordinated (Al, Si), the melt species become $CaAl_2^{IV}Si_2^{IV}O_8$, $CaAl_2^{V}Si_2^{V}O_8$, and $CaAl_2^{VI}Si_2^{VI}O_8$. The appropriate X^{CN} are the mole fractions of these three species, and n^{CN} has the value four, as there are four atoms per formula unit changing coordination state. This second example immediately raises an important point. Why ignore the variation of CN of Ca with respect to O or for that matter the CN of O with respect to Ca and Al? The only justification for doing so must be made on a case-by-case basis by establishing a correlation between the coordination states of different atoms as the system changes composition, T and P. For the example involving SiO_2 this issue did not arise because the correlation of the CN of O about Si is obviously related to that of Si about O. But in the second example involving $CaAl_2Si_2O_8$ liquid that relation is not obvious and must be demonstrated. From the work of Nevins and Spera (1998) and Morgan and Spera (2001a) it can be shown that stipulating the CN of O about (Al,Si) is sufficient to predict with acceptable accuracy the CN of (Al,Si) about O or O about Ca. This fortuitous dependence supports the description of the configurational entropy solely in terms of (Al, Si) coordination for this liquid.

The vibrational contribution to the Gibbs free energy, G^{vib} in equation (24), is expressed as

$$G^{vib} = \sum_{CN} X^{CN} G^{CN} + G^{excess} \tag{26}$$

where the first term is a weighted average of the Gibbs free energies of the liquid species in each end-member structural configuration and the second term (G^{excess}) is an excess free energy which is associated with non-ideal effects both entropic (polymerization) and enthalpic (short range electrostatic) in origin. The G^{CN} in equation (26) is the Gibbs free energy of a liquid in a fixed coordination state. The pressure dependence of G^{CN} is described by an EOS (V^{CN}) that is *suitably parameterized for liquids of fixed CN*,

$$G^{CN} = G^{CN}_{P_r} + \int_{P_r}^{P} V^{CN} dP \tag{27}$$

where P_r is the reference pressure. Combining equations (24), (25), and (26) results in a thermodynamic model for the liquid

$$G^{vib} = n^{CN} RT \sum_{CN} X^{CN} \ln X^{CN} + \sum_{CN} X^{CN} \left(G^{CN}_{P_r} + \int_{P_r}^{P} V^{CN} dP \right) + G^{excess} \tag{28}$$

where the entropic effects of changing melt structure have been decoupled from the EOS. The clear advantage of this model is that EOS parameters are independent of variations in melt structure; the disadvantage of this model is that a separate EOS parameterization must be posited for each coordination state, which can lead to a very large number of parameters that need to be calibrated from data relating melt structure to liquid density. With few exceptions, these data are generally lacking. Fortunately, there are a number of simplifications to (28) that can be made to facilitate practical application of the model. If the focus is placed on silicate liquids, where the principal effect on melt volume with pressure is expected to be related to the CN of O about Si and Al, then it might be reasonable to expect that higher coordination states induce a *configurational collapse* of the structure and a reduction in volume. This reduction in volume can be approximated as a fractional coefficient (f^{CN}) on some reference state volume:

$$V^{CN} = f^{CN} V^{ref} \tag{29}$$

For example, if the reference state for molten silica is taken to be $Si^{IV}O_2$ with all Si in IV-fold O coordination, then

$$0 \le f^{VIII} \le f^{VII} \le f^{VI} \le f^{V} \le f^{IV} = 1 \tag{30}$$

assuming Si can form in IV, V, VI, VII, and VIII-fold coordination with O. The advantage of (29) is that the number of EOS parameters that need be specified has been reduced to only those that characterize one structural state of the liquid. The number of additional parameters (the f^{CN}) introduced by this approximation is much smaller than the number discarded. Furthermore, it should be possible to determine experimentally or compute theoretically (MD simulations) the volume collapse attributable to changing coordination state and therefore determine the f^{CN} directly.

Combining equations (28) and (29) gives

$$G = n^{CN} RT \sum_{CN} X^{CN} \ln X^{CN} + \sum_{CN} X^{CN} G^{CN}_{P_r} + \left(\sum_{CN} f^{CN} X^{CN} \right) \int_{P_r}^{P} V^{ref} dP + G^{excess} \tag{31}$$

One further simplification can be made to the model that is unnecessary but proves justifiable in the application developed in this paper. If the energetics of *mixing* of melt species in differing coordination states is assumed to be ideal, then the excess Gibbs free energy of solution vanishes, which gives the expression

$$G = n^{CN} RT \sum_{CN} X^{CN} \ln X^{CN} + \sum_{CN} X^{CN} G^{CN}_{P_r} + \left(\sum_{CN} f^{CN} X^{CN} \right) \int_{P_r}^{P} V^{ref} dP \tag{32}$$

In order to use the thermodynamic model embodied in equation (32) for analysis of data obtained from molecular dynamics simulations of melts, expressions must be obtained to describe (1) the state of homogenous equilibrium between melt species, that is the equilibrium distribution of coordination states in the melt as a function of T and P, and (2) the volume (or density) of the melt in that state of homogeneous equilibrium. The condition of homogeneous equilibrium can be uniquely specified by demanding that the melt species in the reference coordination state be in equilibrium with all melt species in alternate coordination states

$$(species)^{ref} \rightleftarrows (species)^{CN} \tag{33}$$

The Gibbs free energy change associated with (33) is

$$\Delta G^{CN}_{P_r} = G^{CN}_{P_r} - G^{ref}_{P_r} \tag{34}$$

and when equation (34) is inserted into equation (32) the result is

$$G = n^{CN} RT \left(X^{ref} \ln X^{ref} + \sum_{CN \neq ref} X^{CN} \ln X^{CN} \right) + G^{ref}_{P_r} + \sum_{CN \neq ref} X^{CN} \Delta G^{CN}_{P_r} + \left[1 + \sum_{CN \neq ref} (f^{CN} - 1) X^{CN} \right] \int_{P_r}^{P} V^{ref} dP \tag{35}$$

Homogeneous equilibrium is satisfied when, for all CN not equal to *ref* the expression

$$\frac{\partial G}{\partial X^{CN}} = 0 = n^{CN} RT \ln \frac{X^{CN}}{X^{ref}} + \Delta G^{CN}_{P_r} + (f^{CN} - 1) \int_{P_r}^{P} V^{ref} dP \tag{36}$$

holds. Equation (36) is a *mass action* equation and there is one instance of this expression for every alternate coordination state in the liquid. It may be written in more familiar terms by defining the equilibrium constant (K^{CN}) for reaction (33) in terms of the ratio of species mole fractions

$$RT \ln K^{CN} \equiv n^{CN} RT \ln \frac{X^{CN}}{X^{ref}} = -\Delta G^{CN}_{P_r} - (f^{CN} - 1) \int_{P_r}^{P} V^{ref} dP \tag{37}$$

Equations (36) and (37) are convenient because either may be used to compute a value for $\Delta G^{CN}_{P_r}$. Defining P^{CN} as the pressure where $X^{CN} = X^{ref}$, that is the pressure at which there are equal abundances of melt species in coordination states CN and *ref*, then $\Delta G^{CN}_{P_r}$ is determined from P^{CN}, the reference state EOS (V^{ref}), and configuration collapse fraction (f^{CN})

$$\Delta G_{P_r}^{CN} = -(f^{CN} - 1) \int_{P_r}^{P^{CN}} V^{ref} dP \tag{38}$$

Substitution of equation (38) into equation (37) gives

$$RT \ln K^{CN} = -(f^{CN} - 1) \int_{P^{CN}}^{P} V^{ref} dP \tag{39}$$

Because of the simplicity of the ideal solution model, the species mole fractions may be solved for analytically from the set of mass action expressions solely in terms of the equilibrium constant for each homogeneous reaction. This solution is

$$X^{ref} = \frac{1}{1 + \sum\limits_{CN \neq ref} (K^{CN})^{\left(\frac{1}{n^{CN}}\right)}} \tag{40}$$

and

$$X^{CN} = (K^{CN})^{\left(\frac{1}{n^{CN}}\right)} X^{ref} \tag{41}$$

Equations (40) and (41) give the solution to the condition of homogenous equilibrium between melt species of different coordination state. The mole fractions of each species (X^{CN}) can be computed at specified pressure solely in terms of the free parameters in equation (39), which are the reference EOS parameters defining V^{ref}, and a set of (f^{CN}, P^{CN})-pairs for each species.

An expression for the volume of the melt in a state of homogeneous equilibrium can be obtained by differentiating equation (32) with respect to pressure. Some care must be taken in performing this differentiation however, since the mole fractions of melt species are themselves functions of pressure. At constant T, the pressure derivative of the Gibbs free energy of solution is given formally by

$$\frac{dG}{dP} = \frac{\partial G}{\partial P} + \sum_{CN \neq ref} \frac{\partial G}{\partial X^{CN}} \frac{dX^{CN}}{dP} \tag{42}$$

where the left hand side of the expression $\left(\frac{dG}{dP}\right)$ is the volume of the system. The first partial derivative in the right-hand-side of (42) is taken holding all the X^{CN} constant. The other partial derivatives $\left(\frac{\partial G}{\partial X^{CN}}\right)$ in the right-hand-side of (42) are taken holding P constant. But, the important thing to realize is that these partial derivatives are all equal to zero if the liquid is in a state of homogeneous equilibrium, see equation (36). Therefore, in an equilibrium state the volume of the liquid is given simply by $\left.\frac{\partial G}{\partial P}\right|_{T, X^{ref}, X^{CN}, CN \neq ref}$, which can be readily obtained by taking the partial derivative of equation (32)

$$V = \left(\sum_{CN} X^{CN} f^{CN} \right) V^{ref} \tag{43}$$

The physical interpretation of equation (43) is that the volume of the liquid is a weighted average of the intrinsic volumes of all possible coordination states, with the weights being the proportion of the liquid in each of these states. To use equation (43) to calculate the volume of the liquid, the *T*- and *P*-dependence of the volume in a reference structural state must be known and this implies a parameterization of the reference structural state EOS. In addition, the mole fractions of melt species must be known and that further requires information on the extent of configurational collapse (f^{CN}) and on the variation of species abundances with pressure (P^{CN}). Alternatively, information on melt density and speciation at known *T* and *P* obtained from molecular dynamics simulations can be used to calibrate relevant reference state EOS parameters and the additional f^{CN} and P^{CN}. This is the application that will be followed in the remainder of this paper for analysis of molecular dynamics constraints on stoichiometric liquids of interest.

ANALYSIS OF DATA SETS ON STOICHIOMETRIC LIQUIDS

The objective of the discussion developed in this section, which forms the body of the paper, is two-fold. First, data sets are summarized that constrain densities of stoichiometric (mostly mineral-like) compositions of silicate melts at pressures above ambient. Second, the internal consistency of each of these data sets is assessed with respect to the reference pressure EOS calibration developed in Part II. This entire section is organized by liquid composition to facilitate evaluation of consistent and or conflicting data from the various sources. From this discussion will emerge criteria for utilizing each of these data sets in combination so that constraints on density can be applied across a broad range of silicate liquid compositions. Establishing these criteria is a necessary prelude to the calibration of an EOS parameter mixing-model for magmatic liquids at pressure. That effort is taken up in Part IV.

Mg_2SiO_4 (Forsterite liquid)

The fusion curve of forsterite provides constraints on the volumetric properties of Mg_2SiO_4 liquid at pressures to 15 GPa. Molecular dynamics simulations of liquids of this bulk composition have been performed at pressures to 200 GPa and over a temperature range 1000 to 6000 K (Belonoshko and Dubrovinsky, 1996). These data sets in combination provide tight bounds on EOS parameters for Mg_2SiO_4 liquid.

The fusion temperature and entropy of fusion of forsterite are reported by Richet (1993). Data on the heat capacity of the solid have been evaluated by Berman and Brown (1985) and their parameterized expression is utilized in this study. The heat capacity of liquid Mg_2SiO_4 is calculated from the constants reported by Lange and Navrotsky (1992); their model was also utilized in Part II for the reduction of sound speed data to model melt compressibility. The EOS for the solid is parameterized from an extensive data set of volumetric measurements. Data sources and fit residuals to the derived solid EOS are displayed in figure 1. Universal EOS parameters for the solid are listed in table 1.

Experimental data that constrain the fusion curve of forsterite are displayed in figure 2. The earlier piston cylinder studies of Davis and England (1964) are supplemented by the higher-pressure multianvil studies of Ohtani and Kumazawa (1981), Kato and Kumazawa (1985b) and Presnall and Walter (1993). The latter authors determined that the melting of forsterite becomes incongruent at 10.1 GPa (and 2250 °C), melting above that pressure to periclase (MgO) plus liquid.

Molecular dynamics simulations of the density of Mg_2SiO_4 liquid are reported by Wasserman and others (1993a), Belonoshko and Dubrovinsky (1996), and Zhou and Miller (1997). The most extensive studies are by Belonoshko and Dubrovinsky (1996) who performed simulations over the *T-P* range of 1000 to 6000 K and 0 to 200 GPa, respectively. These authors fitted their results to a modified 3rd order Birch Mur-

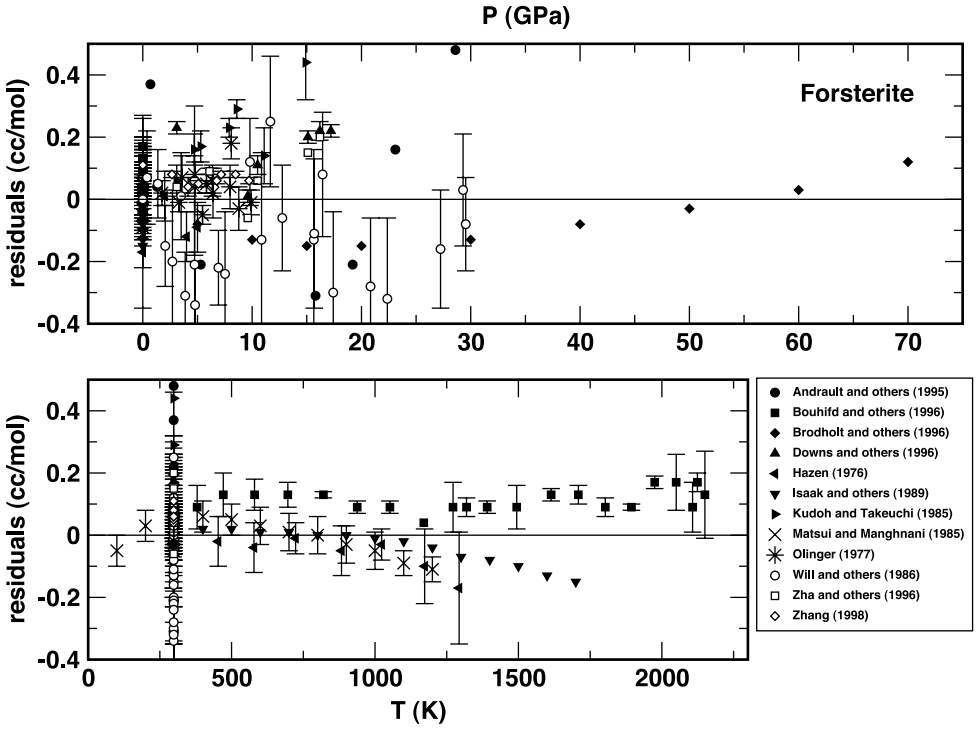

Fig. 1. Residuals (cc/mol) associated with a Universal EOS parameterization of volumetric data on forsterite (Mg_2SiO_4) as a function of temperature (lower panel) and pressure (upper panel). A residual of ± 0.44 cc/mol corresponds to a 1% relative error in the reference volume. EOS parameters are listed in table 1.

naghan EOS with explicit temperature dependent parameters (Saxena and others, 1993). A calibration data set was generated from the parameterized EOS of Belonoshko and Dubrovinsky (1996) along a representative isotherm at 1673 K, and this data set is plotted in figure 3. Also plotted are the results of simulations at 3500 K and 5000 K from Wasserman and others (1993) and Zhou and Miller (1997). The MD simulation results of Belonoshko and Dubrovinsky (1996) are internally consistent with the results of Zhou and Miller (1997). By contrast, Wasserman and others (1993) report densities higher by ~3 to 5 percent. Presumably these differences in density can be attributed to the more accurate interatomic potentials utilized in the more recent MD work.

The initial slope of the fusion curve (as defined by the tight brackets of Davis and England, 1964) is consistent with the reported entropy of fusion and a volume of fusion that is calculated from the solid Universal EOS (table 1) and the reference pressure MD volume from Belonoshko and Dubrovinsky (1996). It is inconsistent with a volume of fusion calculated from the parameters reported in Part II. The latter is found to be 7.35 cc/mol, while the value from the Clapyron slope of the fusion curve (1.58 GPa/100 K) is 3.84 cc/mol. The source of this discrepancy results primarily from the model value (Part II) for the thermal expansion, which is about a factor of two larger than that obtained by Belonoshko and Dubrovinsky (1996). These MD studies also indicate that the compressibility of the melt is a factor of 2 to 3 smaller than the model value for this bulk composition from Part II, with the implication that the model sound speed (c) is underpredicted by a factor of $\sqrt{2}$ to $\sqrt{3}$. An acceptable EOS

TABLE 1

Recommended EOS parameters for the Universal EOS

Phase - state - (formula)	V (cc/mol)	$\alpha \times 10^5$	K (GPa)	K'
Albite ($NaAlSi_3O_8$)	100.83[1]	2.7883	53.118	5[2]
Anorthite ($CaAl_2Si_2O_8$)	100.75[1]	1.4102	78.570	5.2772
Coesite (SiO_2)	20.64[1]	0.73960[1]	107.46	4.4382
Diopside ($CaMgSi_2O_6$)	66.200[1]	3.3080	103.23	7.1349
Enstatite - $C\frac{2}{c}$ ($Mg_2Si_2O_6$)	61.758	4.4706	70.018	10.864
Enstatite - $Pbca$ ($Mg_2Si_2O_6$)	62.660[1]	3.1219	108.51	7.7568
Fayalite (Fe_2SiO_4)	46.300[1]	2.9447	127.96	5.0170
Forsterite (Mg_2SiO_4)	43.660[1]	3.1393	125.10	5.0580
Jadeite ($NaAlSi_2O_6$)	60.340[1]	2.4040	119.73	5[2]
Nepheline ($NaAlSiO_4$)	49.00[3]	3.1802	48.78	2.5[2]
Pyrope ($Mg_3Al_2Si_3O_{12}$)	113.16[1]	2.4226	164.87	5.2915
Quartz (SiO_2)	23.700[1]	0[1]	82.247	5[2]
Sanidine ($KAlSi_3O_8$)	108.96[1]	2.1209	53.440	5[2]
Titanite ($CaTiSiO_5$)	55.65[1]	2.52	58.0	5[2]

[1]Fixed value from Berman (1988).
[2]Estimate.
[3]Estimate. Value reported by Waterweise and others (1995) is 54.13 cc/mol.

parameterization is obtained that accommodates both the fusion curve and MD constraints if the reference pressure $\left(V_{0,T_r}, \alpha, c, \frac{dc}{dT}\right)$ and the high-pressure (V_2, V_3, V_4) parameters are fitted simultaneously. Parameter values obtained from this fit are listed in table 2 and compared to reference pressure parameters calculated from the model of Part II where applicable. The calculated fusion curve for forsterite is plotted in figure 2 and calculated densities from the model EOS are compared to MD results in figure 3. No data set is given preferential weight in constructing the fit to the model EOS.

A critical constraint that develops from the higher-pressure MD density estimates is in regard to the pressure dependence of α. In Part I it is shown that the relation

$$\alpha_{T_r,P} \approx \alpha_{T_r,P_r} + \left(\frac{V_1\alpha}{V_0} + \frac{V_0}{Mc^3}\frac{dc}{dT} - \frac{V_0\alpha^2}{C_p}\right)\Bigg|_{T_r,P_r}(P - P_r) \tag{44}$$

represents a truncated Taylor expansion of the thermal expansivity, from which it is apparent that the temperature-dependence of the sound speed $\left(\frac{dc}{dT}\right)$ is a critical EOS parameter for defining $\frac{\partial\alpha}{\partial P}$. The value for this parameter given in table 1 is refined largely from the MD studies; the model value from Part II is obtained from sound speed measurements made on multicomponent silicate liquids over a narrow temperature range. The two values are in good agreement (within 20%) considering the uncertainty of either estimate.

Analysis of the internal consistency of the high-pressure data sets with the reference pressure calibration reveals that the EOS parameters from Part II do not extrapolate well to Mg_2SiO_4 liquid. This fact is not surprising, as there are no density or

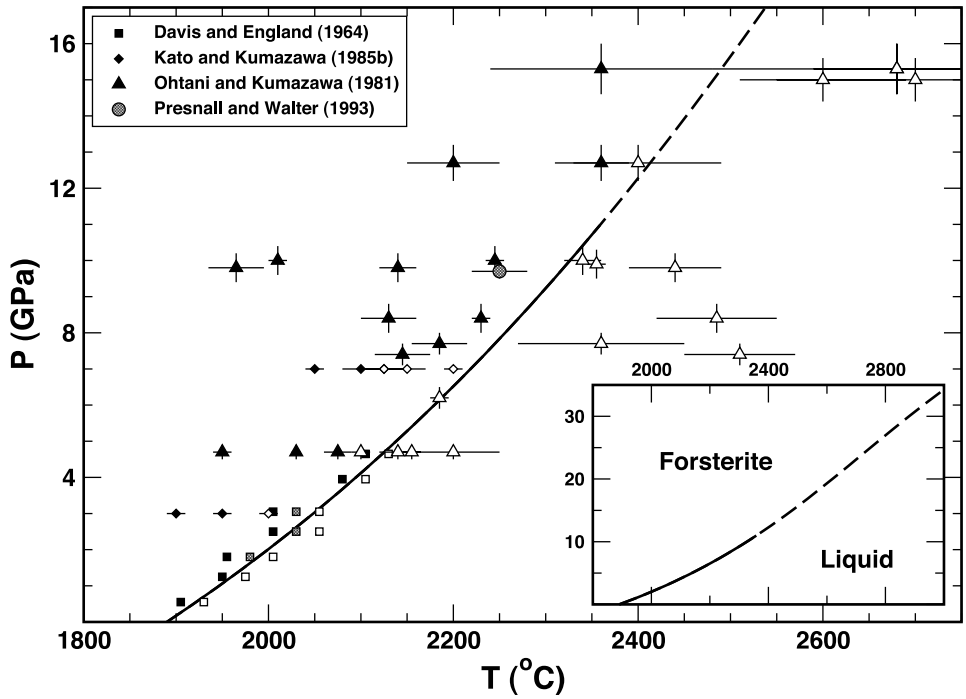

Fig. 2. Experimental data delimiting the fusion curve of forsterite (Mg_2SiO_4). Filled symbols indicate no melting, open symbols indicate complete melting, and gray-filled symbols the onset of melting. The solid curve is the calculated fusion curve based on the liquid EOS parameters and ancillary thermodynamic properties listed in table 2. The dashed curve represents the metastable extension of the fusion curve above the pressure where forsterite melts incongruently to periclase + liquid. The inset shows an extrapolation of the fusion curve to elevated pressure.

sound speed measurements with excess molar MgO over SiO_2 in the calibration database of Part II. The most significant discrepancies appear to be in the thermal expansion and the sound speed. The Part II reference temperature/pressure volume is ~3 percent larger than the optimal one derived here.

It should also be noted that because information on melt structure is not available from published MD simulations, no attempt is made to incorporate configurational effects in developing an EOS calibration for this system.

Fe_2SiO_4 (Fayalite liquid)

Fayalite is one of the few Fe-bearing phases for which the melting curve has been determined. Experimental measurements of liquid properties are especially difficult to undertake because of the reactive nature of Fe-bearing liquids and because control of the oxidation state is critical to maintaining the Fe^{2+}/Fe^{3+} ratio of the liquid. These difficulties are especially important at low pressure, where the concentration of Fe_2O_3 in nominal-"Fe_2SiO_4" liquid can be as high as 11.6 weight percent at f_{O_2} corresponding to equilibrium with metallic iron (Lindsley, 1967). At higher pressures, because the molar volume of Fe_2O_3 is larger than that of FeO (see Part II), oxygen is expelled from the liquid and most of the Fe is present as FeO over a wide range of f_{O_2} (Carmichael and Ghiorso, 1986). As a consequence, comparison of reference pressure density properties of molten Fe_2SiO_4 (Shiraishi and others, 1978; Lange and Carmichael, 1987) with high-pressure measurements (Agee 1992a, 1992b) is problematic, relying on the

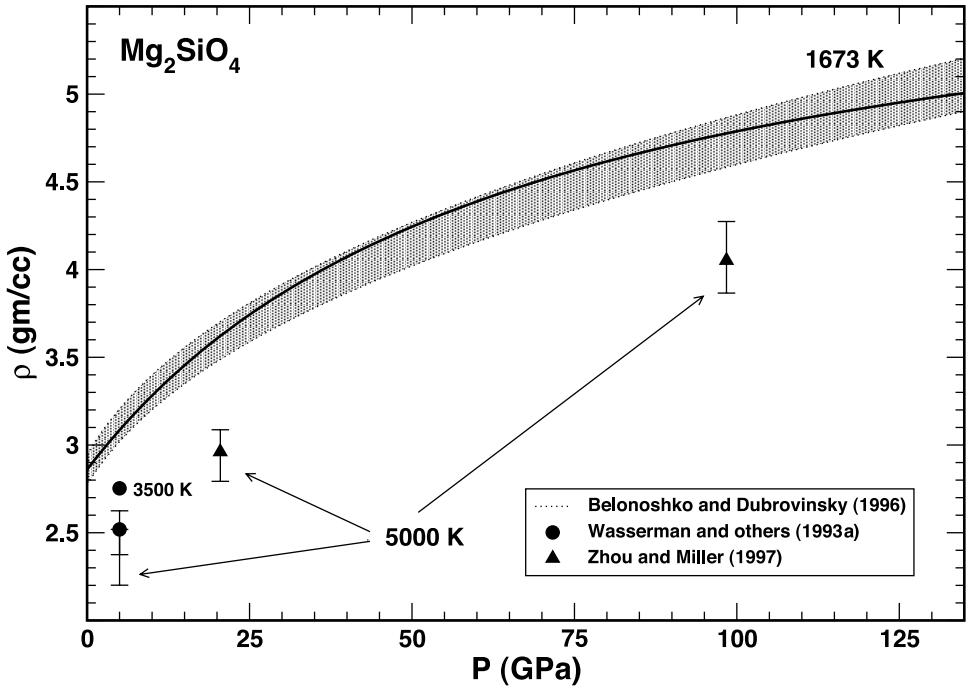

Fig. 3. Analysis of molecular dynamics simulations of melt density of Mg_2SiO_4 liquid. The gray band represents density estimates (± 3%) computed at 1673 K from the parameterization of Belonoshko and Dubrovinsky (1996). Brackets are estimates from Wasserman and others (1993a) and Zhou and Miller (1997). Values represented by the circles, triangles and heavy solid line are computed from the liquid EOS parameters listed in table 2.

accurate estimate of FeO and Fe_2O_3 contents of low-pressure liquids and the assumption that liquids at higher pressure are dominantly ferrous. Unfortunately, there are no molecular dynamics simulations of Fe_2SiO_4 liquid that can assist in the interpretation of experimental results.

Stebbins and others (1984) report experimental data on the temperature and entropy of fusion of fayalite (Fe_2SiO_4). Data on the heat capacity of the solid have been evaluated by Berman and Brown (1985) and are utilized here. The heat capacity of the liquid is from Lange and Navrotsky (1992). Fabrichnaya and Sundman (1997) have reviewed data on the volumetric properties of the solid at high T and P. Their sources are utilized and supplemented with the work of Zhang (1998) to construct a Universal EOS model for the solid. Constants are reported in table 1. Data sources and fit residuals are given in figure 4.

Data on the fusion curve of fayalite are reported by Lindsley (1967), Akimoto and others (1967), Hsu (1967) and Ohtani (1979) and are plotted in figure 5. Lindsley's (1967) experiments were performed in solid-media piston-cylinder apparatus using Fe-capsules. He found experimental products consisting of quenched fayalite crystals, small amounts of brownish glass ($< 1\%$; Fe_2O_3-bearing?), and metallic iron. Akimoto and others (1967) utilized Fe-capsules for runs below 1500 °C and no capsules (the sample was encased in the graphite furnace) at higher temperatures. They concluded that fayalite melts congruently over the entire pressure range. By contrast Hsu (1967), who conducted piston-cylinder experiments in Fe-capsules, found ubiquitous quenched metallic Fe and glass, which he interpreted as indicating incongruent melting behavior

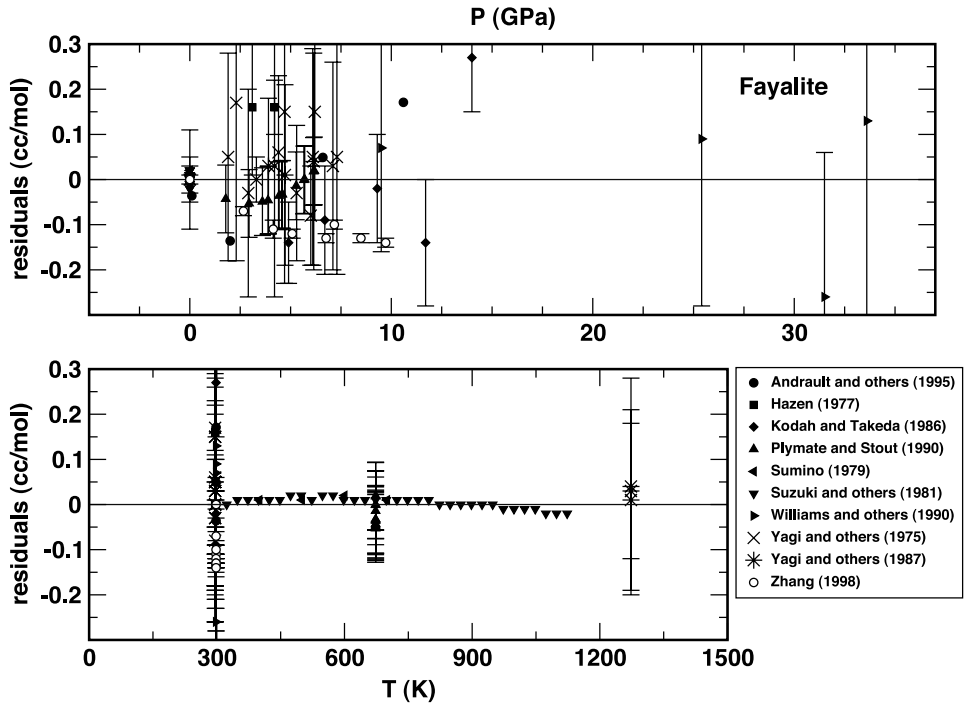

Fig. 4. Residuals (cc/mol) associated with a Universal EOS parameterization of volumetric data on fayalite (Fe_2SiO_4) as a function of temperature (lower panel) and pressure (upper panel). A residual of ± 0.46 cc/mol corresponds to a 1% relative error in the reference volume. EOS parameters are listed in table 1.

over the entire range of measurements. He regarded the presence of Fe metal and glass in experimental run products as evidence of Fe_2O_3 in the melt. The measurements of Ohtani (1979) were performed in multi-anvil apparatus using graphite as a pressure medium. No evidence of quenched Fe was detected in his experimental run products.

Fe_2SiO_4-liquid density estimates obtained from the "sink-float" measurements of Agee (1992a, 1992b) are plotted in figure 6. In figure 7 are plotted results from the shock-compression measurements of Chen and others (2002). Utilizing EOS parameter values calculated for the reference pressure properties of Fe_2SiO_4 from Part II[4] (see table 2), high-pressure EOS parameters (V_2, V_3, V_4) are extracted by simultaneously fitting the fusion curve, sink-float and shock compression measurements. Resulting parameter values are reported in table 2. A fusion curve calculated from these parameters is drawn in figure 5. Model estimates of melt density are plotted in figure 6. The calculated Hugoniot curve is given in figure 7 along with internally consistent estimates of shock temperatures.

The reference pressure calibration of Part II is consistent with the higher-pressure data sets. The reversal brackets of Akimoto and others (1967) and Ohtani (1979) correspond most closely to the theoretical fusion curve (fig. 5). Both sets of experiments were performed in graphite capsules and as noted above, showed no evidence of incongruent melting behavior. The theoretical Hugoniot curve (fig. 7) is in excellent

[4] It is assumed that at the pressures of the shock experiments, the concentration of Fe_2O_3 in the melt is insignificant.

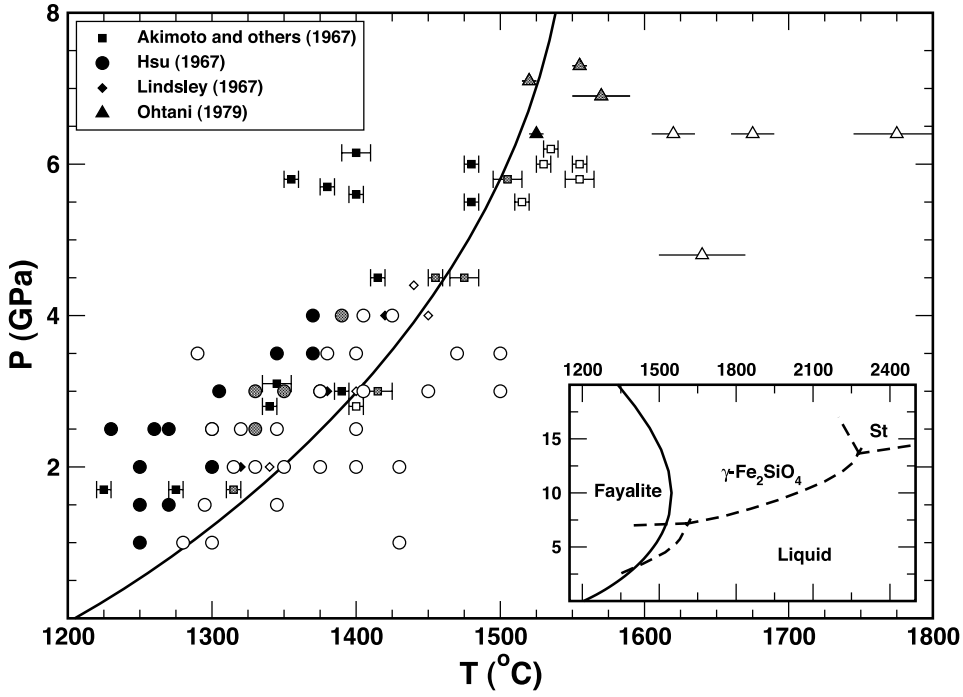

Fig. 5. Experimental data delimiting the fusion curve of fayalite (Fe_2SiO_4). Filled symbols indicate no melting, open symbols indicate complete melting, and gray-filled symbols the onset of melting. The solid curve is the calculated fusion curve based on the liquid EOS parameters and ancillary thermodynamic properties listed in table 2. The inset shows an extrapolation of the fusion curve to elevated pressure (solid curve). The dashed curve represents equilibrium melting relations inferred by Ohtani (1979).

agreement with the data. The sink-float experiments of Agee (1992a, 1992b) are modeled within 1 percent of observed values, but the predicted densities are systematically lower for neutral buoyancy experiments (fig. 6). Chen and others (2002) also noted the discrepancy between their density measurements and those of Agee (1992b), and given the agreement at 5 GPa of the experimental brackets and calculated fusion curve, and the calculated Hugoniot with the measured ρ-*P* bracket, the discrepancy in modeling the sink-float measurements may be due to a systematic experimental error. Significantly, the liquid thermal expansion inferred from Agee's sink-float measurements is modeled successfully by the EOS parameterization developed here (fig. 6).

Lastly, it is worth noting that the extrapolated fusion curve (inset in fig. 5) shows strong curvature above 5 GPa, which causes the thermal maximum at approximately 10 GPa. This density turnover is well below the pressure of the γ-spinel transition (Ohtani, 1979).

$Mg_2Si_2O_6$ (Enstatite liquid)

The fusion curve of enstatite provides constraints on the volumetric properties of $Mg_2Si_2O_6$ liquid at pressures to 16 GPa. Molecular dynamics simulations of liquids of this bulk composition have been performed at pressures to 200 GPa and over a temperature range 1000 to 6000 K (Belonoshko and Dubrovinsky, 1996). These data sets in combination provide tight limits on EOS parameters for $Mg_2Si_2O_6$ liquid.

Enstatite melts incongruently (to forsterite plus liquid) at pressures up to ~0.13 GPa (Chen and Presnall, 1975). The stable structural state of solid $Mg_2Si_2O_6$ at fusion

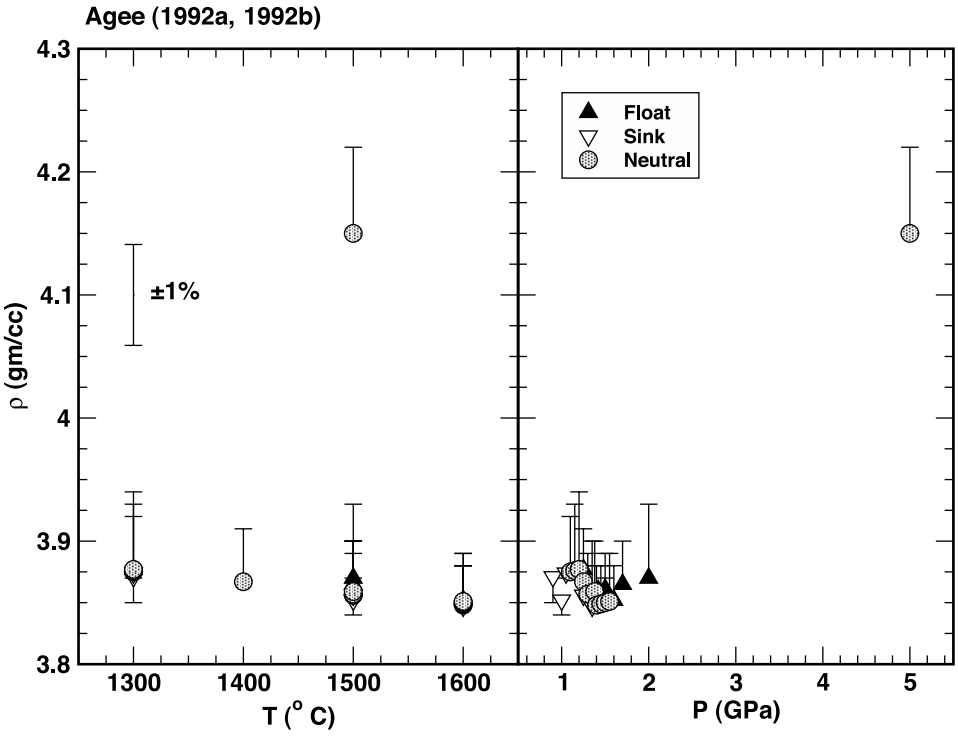

Fig. 6. Analysis of the "sink-float" experimental data of Agee (1992a, 1992b) on Fe_2SiO_4 composition liquids using ruby as a density marker. Density is reported in units of grams/cm^3 and is plotted on the ordinate. Upward pointing filled triangles denote experimental conditions where the index mineral floats in the liquid, unfilled triangles denote experimental conditions where the index mineral sinks in the liquid; the triangles are plotted at the calculated density of the mineral at the T and P of the experiment. Each triangle is connected by a straight line that terminates with a horizontal bracket plotted at a density calculated from the EOS parameters reported in table 2. An uncertainty bracket of ± 1% is displayed for reference.

temperatures and low-pressure is protoenstatite (*Pbcn*). The congruent portion of the fusion curve has two invariant points corresponding to phase transitions in the solid. The first is at 1.6 GPa and 1730 °C (extrapolated from Chen and Presnall, 1975) where protoenstatite transforms to orthoenstatite (*Pbca*), and the second is at 11.9 GPa and a temperature of 2230 °C (Presnall and Gasparik, 1990) where orthoenstatite transforms to clinoenstatite $\left(C\,\frac{2}{c}\right)$. Above 16.4 GPa, clinoenstatite transforms to majorite $\left(I\,\frac{4_1}{a}\right)$.

The metastable congruent fusion temperature and entropy of fusion of enstatite at the reference pressure are taken from Richet and Bottinga (1986). Heat capacities of the low-pressure solid polymorphs are reported by Berman and Brown (1985); the heat capacity of clinoenstatite has not been determined and the equation for orthoenstatite is used here. Volumetric properties of the *Pbca* and $C\frac{2}{c}$ phase are plotted in figures 8 and 9 as residuals to model expressions based upon the Universal EOS, with parameters provided in table 1.

Fusion curve experimental data are plotted in figure 10. The lower-pressure data of Boyd and others (1964) are from piston-cylinder experiments and the higher-pressure results of Presnall and Gasparik (1990) were obtained in multianvil apparatus.

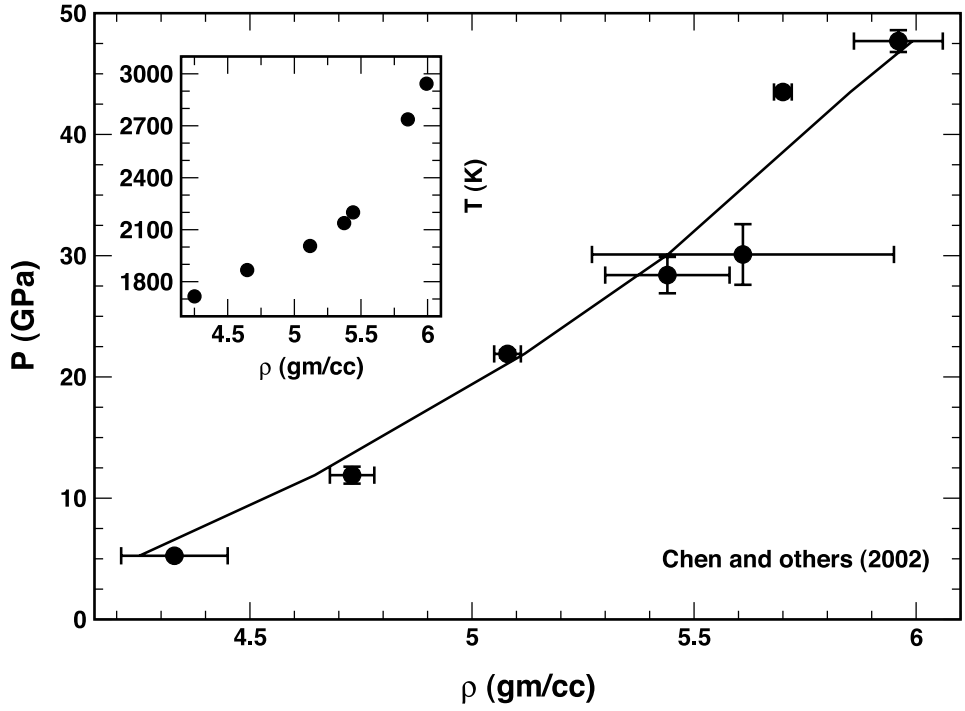

Fig. 7. Shock compression data (Chen and others, 2002) and calculated shock Hugoniot (solid curve; EOS parameters from table 2) for liquid of Fe_2SiO_4 composition. Inset shows calculated shock temperatures plotted against calculated densities.

Experimental data reported by Kato and Kumazawa (1985a, 1986) are not plotted because of possible contamination of their samples with Al_2O_3, CaO and H_2O.

Estimates of the density of $Mg_2Si_2O_6$ liquid obtained by molecular dynamics simulations are plotted in figures 11 and 12. Data from Belonoshko and Dubrovinsky (1996) are computed from their parameterized EOS analogous to the procedure used for Mg_2SiO_4 liquid described above. Estimates of the average CN of O about Si are plotted in the inset of figure 11. These data are from Wasserman and others (1993b) and Kubicki and Lasaga (1991), but the latter are less reliable because the structure simulations were run at temperatures below the glass transition. The initial Clapyron slope of the fusion curve inferred from Boyd and others's (1964) results is 0.798 GPa/100 °C, which gives a volume of fusion of 9.61 cc/mol and requires a correction to V_{0,T_r} from Part II of –2.68 cc/mol or ~ –3.5 percent. The thermal expansion at the reference pressure computed from the model of Part II is consistent with the MD results of Belonoshko and Dubrovinsky (1996) and Matsui (1996) as is the reference pressure compressibility (sound speed). The corrected V_{0,T_r} obtained from the Clapyron slope analysis is within 1 percent of the number derived from Matsui's (1996) reference pressure simulations. The value of V_{0,T_r} reported in table 2 is the one fitted from Matsui's (1996) reference pressure data set.

The high-pressure EOS parameters (V_2, V_3, V_4) can be extracted from the fusion curve and remaining MD data along with model parameters (f^V, P^V, f^{VI}, P^{VI}) that account for CN variation (for example, fig. 11). The thermodynamic model developed above (for example, eq 35) is utilized for this purpose with n^{CN} taken to be two; the assumption is made that coordination changes associated with Mg and O are corre-

TABLE 2

EOS parameters for analyzed experimental datasets

Liquid	V_{T_r,P_r} $\left(\frac{cc}{mol}\right)$	ΔS_{fus} $\left(\frac{J}{K-mol}\right)$	$\alpha \times 10^4$ $\left(\frac{1}{K}\right)$	$c \times 10^{-3}$ $\left(\frac{cm}{s-gfw}\right)$	$\frac{dc}{dT}$ $\left(\frac{cm}{s-K-gfw}\right)$	MW $\left(\frac{gm}{mol}\right)$	C_P $\left(\frac{J}{K-mol}\right)$	$\left.\frac{\partial V}{\partial P}\right\|_{T_r,P_r}$ $\left(\frac{cc}{GPa-mol}\right)$
Mg_2SiO_4	**49.20**	65.3[a]	**0.600**	**4.700**	**0.3867**	140.71	271.00	**–0.8326**
	(*50.74*)		(*1.336*)	(*3.007*)	(*0.3169*)			(*–2.307*)
Fe_2SiO_4	*54.46*	59.9[b]	*0.7470*	*2.374*	*0.06161*	*203.78*	*240.20*	*–2.703*
$Mg_2Si_2O_6$	**74.77**	76.7[c]	*1.005*	*2.836*	*0.3375*	*200.79*	*353.60*	**–3.730**
	(*77.45*)							(*–4.002*)
$CaMgSi_2O_6$	*82.11*	82.5[d]	*0.9796*	*2.990*	*0.2173*	*216.56*	*349.20*	*–3.791*
SiO_2	***28.10***	5.53[e]	***0.1165***	***5.227***	***0.04157***	60.08	82.60	***–0.4832***
	(*26.71*)		(*0.3770*)	(*2.322*)	(*0.3993*)			(*–2.223*)
$Na_2Si_4O_9$	*135.96*		*0.7432*	*2.474*	*–0.1140*	*302.32*	*428.00*	*–10.39*
$CaAl_2Si_2O_8$	**113.90**	73.4[f]	*0.4185*	*2.837*	*0.2743*	*278.2*	*425.3*	**–5.882**
	(*107.71*)							(*–5.260*)
$NaAlSi_3O_8$	*113.50*	46[g]	*0.5053*	*2.559*	*0.09155*	*262.22*	*381.75*	*–7.644*
$NaAlSi_2O_6$	*86.79*	53.9[h]	*0.5448*	*2.679*	*–0.01104*	*202.14*	*299.15*	*–5.317*
$NaAlSiO_4$	*60.08*	21.74[i]	*0.6194*	*2.978*	*–0.2162*	*142.05*	*216.55*	*–2.972*
$Mg_3Al_2Si_3O_{12}$	*157.79*	154[j]	*0.7173*	*2.822*	*0.3613*	*403.15*	*700.70*	*–7.658*
$KAlSi_3O_8$	*122.14*	39.2[k]	*0.6478*	*2.294*	*0.06949*	*278.34*	*382.20*	*–10.46*
$CaTiSiO_5$	*66.83*	73.85[l]	*1.639*	*2.661*	*0.3354*	*196.06*	*281.60*	*–3.930*
$(CaMgSi_2O_6)_{0.64}$-$(CaAl_2Si_2O_8)_{0.36}$	*38.26*		*0.7414*	*2.935*	*0.2378*	*100.03*	*157.77*	*–1.784*
Komatiite	*36.29*		*0.9514*	*2.861*	*0.2524*	*99.52*	*164.92*	*–1.737*
MORB	*37.27*		*0.6960*	*2.756*	*0.1949*	*99.26*	*148.94*	*–1.918*

Source: Part I (***in bold italics***), Part II (*in italics*), this paper (**in bold**), or footnoted.

TABLE 2

(continued)

Liquid	$\left.\frac{\partial^2 V}{\partial P^2}\right\|_{T_r,P_r}$ $\left[\frac{cc}{(GPa)^2 - mol}\right]$	$\left.\frac{\partial^3 V}{\partial P^3}\right\|_{T_r,P_r}$ $\left[\frac{cc}{(GPa)^3 - mol}\right]$	$\left.\frac{\partial^4 V}{\partial P^4}\right\|_{T_r,P_r}$ $\left[\frac{cc}{(GPa)^4 - mol}\right]$	a $\left(\frac{1}{GPa}\right)$	b $\left[\frac{1}{(GPa)^2}\right]$	P^V (GPa)	f^V	P^{VI} (GPa)	f^{VI}
Mg_2SiO_4	**0.05235**	**–0.004842**	**0.0005880**	**0.05472**	**0.0007510**				
Fe_2SiO_4	**2.215**	**–4.305**	**11.63**	**0.7229**	**0.03081**				
$Mg_2Si_2O_6$	**0.9639**	**–0.3662**	**0.1820**	**0.2450**	**0.01529**	**55.24**	**0.8853**	**84.17**	**0.7849**
$CaMgSi_2O_6$	**1.084**	**–0.4635**	**0.2637**	**0.2169**	**0.01064**	**15.92**	**0.8882**	**50[m]**	**0.7933**
SiO_2	***0.02220***	***–0.0005021***	***–0.0002267***	***0.06638***	***0.001352***	***9.225[n]***	***0.8346***	***9.807***	***0.7811***
$Na_2Si_4O_9$	**–4.049**	**44.00**	**–199.2**	**1.259**	**0.4605**	**10.57**	**0.8280**	**25.06**	**0.6744**
$CaAl_2Si_2O_8$	**1.237**	**–0.4238**	**0.1880**	**0.2284**	**0.01342**	**2.097[o]**	**0.8990**	**11.43**	**0.7933**
$NaAlSi_3O_8$	**2.704**	**7.315**	**–45.39**	**1.149**	**0.3627**				
$NaAlSi_2O_6$	**4.074**	**8.325**	**–28.26**	**0.8058**	**0.2918**	**16.37[p]**	**0.7156**	**22.75**	**0.6333**
$NaAlSiO_4$	**–2.024**	**9.571**	**–10.64**	**0.5087**	**0.3636**				
$Mg_3Al_2Si_3O_{12}$	**–7.002**	**17.28**	**–29.15**	**0.5649**	**0.1179**				
$KAlSi_3O_8$	**6.317**	**–3.307**	**–8.037**	**1.245**	**0.3233**				
$CaTiSiO_5$	**0.4504**	**–0.001733**	**-6.747×10^{-6}**	**0.001334**	**2.959×10^{-6}**				
$(CaMgSi_2O_6)_{0.64}$-$(CaAl_2Si_2O_8)_{0.36}$	**0.4772**	**–0.1882**	**0.09905**	**0.1230**	**–0.001133**	**10.94**	**0.8918**	**36.12**	**0.7933**
Komatiite	**1.177**	**–2.968**	**11.06**	**0.9927**	**0.05135**	**55.24**	**0.8589**	**84.17**	**0.7849**
MORB	**–0.1047**	**0.6206**	**–0.7346**	**0.3188**	**0.04522**	**10.94**	**0.8918**	**36.12**	**0.7933**

[a] Forsterite, Richet (1993), ±6.0. T_{fus} = 2163 K. [b] Fayalite, Stebbins and others (1984), ±0.7. T_{fus} = 1478 K. [c] *Pbca* enstatite, Richet and Bottinga (1986), ±6.6. T_{fus} = 1832 K. [d] Diopside, Richet and Bottinga (1984a), ±1.2. Lange and others (1990) give 82.7 ± 1.4. T_{fus} = 1670 K. [e] Quartz, Richet and others (1982), ±0.56; internally consistent values for Coesite and Stishovite are developed in Part I. T_{fus} = 1700 K. [f] Average for anorthite of Weill and others (1980), 74.1 ± 4.8 and Richet and Bottinga (1984a), 72.7 ± 2.2. T_{fus} = 1830 K. [g] Albite, Richet and Bottinga (1984b, 1986), ±2.2. T_{fus} = 1373 K. [h] Jadeite, Richet and Bottinga (1984b, 1986), ±2.7. T_{fus} = **820 K.** [i] Nepheline, Stebbins and others (1983), β-phase, their eq (15). T_{fus} = 1373 K, estimated from Smith (2002). [j] Pyrope, Tequi and others (1991), ±7.6. T_{fus} = 1535 K. [k] Estimated by Stebbins and others (1984), ±2.8. T_{fus} = 1473 K. [l] Tangeman and Xirouchakis (1999) ±0.1. T_{fus} = 1655 K. [m] P^{VI} estimated as the *minimum* pressure permitted by the data. f^V is an estimate, as it is unconstrained by data; the value chosen is taken to be identical to $CaAl_2Si_2O_8$. [n] Values at 900 K; values at 4000 K (Part I) are P^V = 9.692 and P^{VI} = 16.49. [o] Additionally, P^{VII} = 21.19, f^{VII} = 0.7636, P^{VIII} = 40.08, f^{VIII} = 0.6678. [p] Values of P^V, f^V, P^{VI}, and f^{VI} applicable to the entire $NaAlO_2$-SiO_2 binary join. High-pressure EOS parameters for $NaAlSi_3O_8$, $NaAlSi_2O_6$, and $NaAlSiO_4$ are dependent, linear-combinations of $NaAlO_2$ and SiO_2 endmember properties.

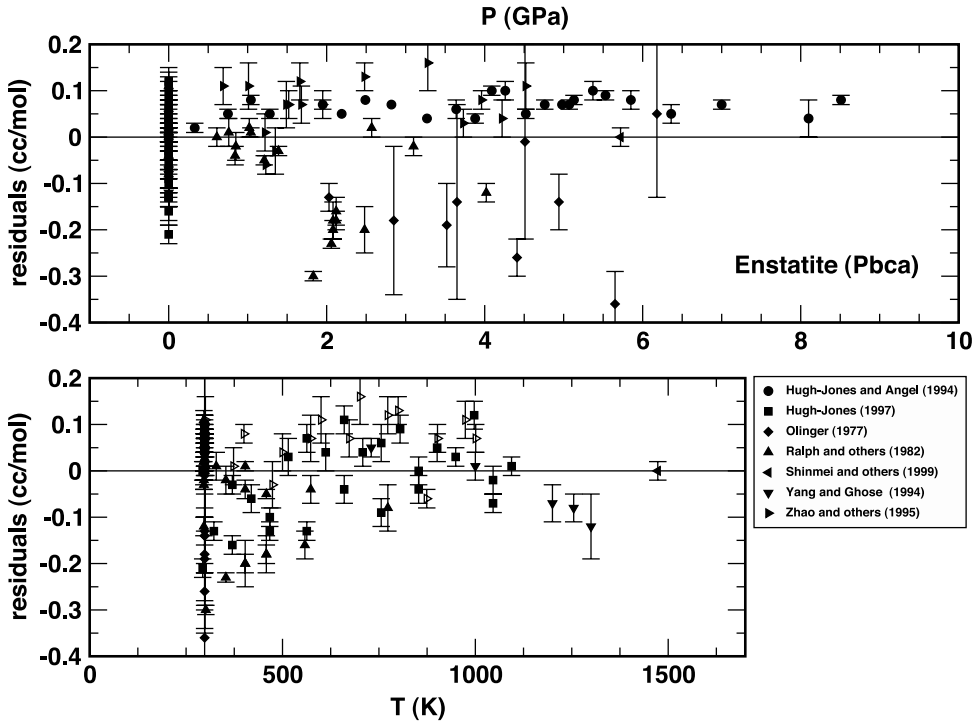

Fig. 8. Residuals (cc/mol) associated with a Universal EOS parameterization of volumetric data on orthorhombic enstatite ($Mg_2Si_2O_6$) as a function of temperature (lower panel) and pressure (upper panel). A residual of ± 0.63 cc/mol corresponds to a 1% relative error in the reference volume. EOS parameters are listed in table 1.

lated to those of Si and O. Fits to the data sets are optimized by the parameter values given in table 2. The calculated fusion curve is plotted in figure 10. Density estimates are compared to MD values in figures 11 and 12. Average CNs for Si are calculated for three isotherms and plotted in figure 11.

The model fusion curve gives an excellent fit to the data of Boyd and others (1964), but fails to recover the experiments of Presnall and Gasparik (1990) above 9 GPa. The model makes the solid too stable at these pressures and this result implies that the liquid density is too low[5]. But, the MD data at similar pressures and temperatures indicates that model density values are ~2 to 3 percent too high (figs. 11 and 12). The two data sets are clearly drawing the EOS parameter values into a compromise. The resolution may be (1) a problem with the volumetric properties of the solid at high pressure or (2) a systematic temperature/pressure offset in the multianvil experiments, or perhaps (3) a problem with the interatomic potentials utilized in the MD simulations. The last is unlikely however as the same potentials were used by Belonoshko and Dubrovinsky (1996) to model Mg_2SiO_4 liquid and by Matsui to successfully model a number of liquids in the system CMAS including $CaMgSi_2O_6$ (see below).

[5] The liquid is not stable enough, which means its Gibbs free energy is not negative enough. As the Gibbs free energy changes with the pressure integral of the volume, if the volume were smaller, the Gibbs free energy would be more negative. A smaller volume implies a larger density, therefore the density of the liquid is too low.

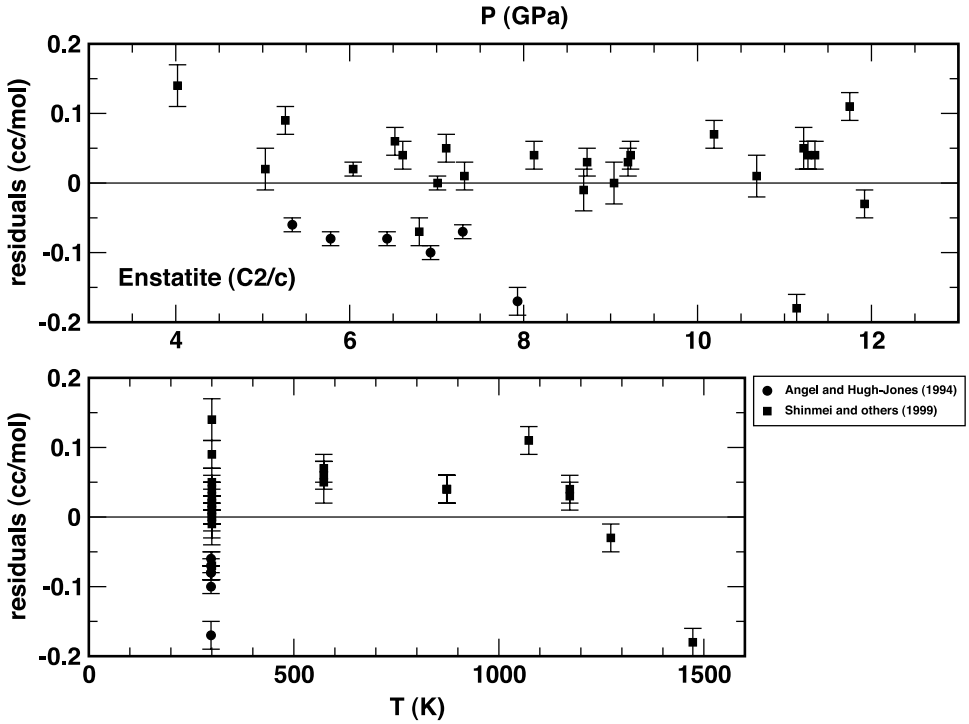

Fig. 9. Residuals (cc/mol) associated with a Universal EOS parameterization of volumetric data on monoclinic enstatite ($Mg_2Si_2O_6$) as a function of temperature (lower panel) and pressure (upper panel). A residual of ± 0.62 cc/mol corresponds to a 1% relative error in the reference volume. EOS parameters are listed in table 1.

There does appear to be an inconsistency between the MD simulations of Wassermann and others (1993b) and the other studies (fig. 12). This inconsistency is especially apparent in figure 12B, where it can be seen that the problem appears to involve the high-pressure (5 GPa) thermal expansion of the liquid. The Wasserman and others' (1993b) data imply a value for α at 5 GPa that is approximately equivalent to the reference pressure number. However, a larger value for the thermal expansion at pressure is not consistent with Belonoshko and Dubrovinsky's (1996) simulations nor can it be reconciled with the $\frac{dc}{dT}$ value computed from the calibration of Part II. Another inconsistency is noted above between the simulation results of Wasserman and others (1993) and the work of Belonoshko and Dubrovinsky (1996) and Zhou and Miller (1997) for Mg_2SiO_4 liquid. It appears likely, that the interatomic potentials utilized by Wasserman and others (1993b) fail to capture an important aspect of the atomic forces in the $MgO\text{-}SiO_2$ system.

The model density curve in figure 11 undergoes two changes in slope, one at approximately 50 GPa and another at approximately 100 GPa. These changes in slope are due to the configurational collapse of the liquid that is expressed over pressure intervals where there are rapid changes in the Si CN (see figure inset). The model parameters f^V and f^{VI} give the fraction of collapse in terms of the volume in the reference state, which is taken here to be the volume of $Mg_2Si_2^{IV}O_6$ liquid (that is, all Si in [IV] coordination) at all T and P. The dashed curve in the figure (labeled Si[IV])

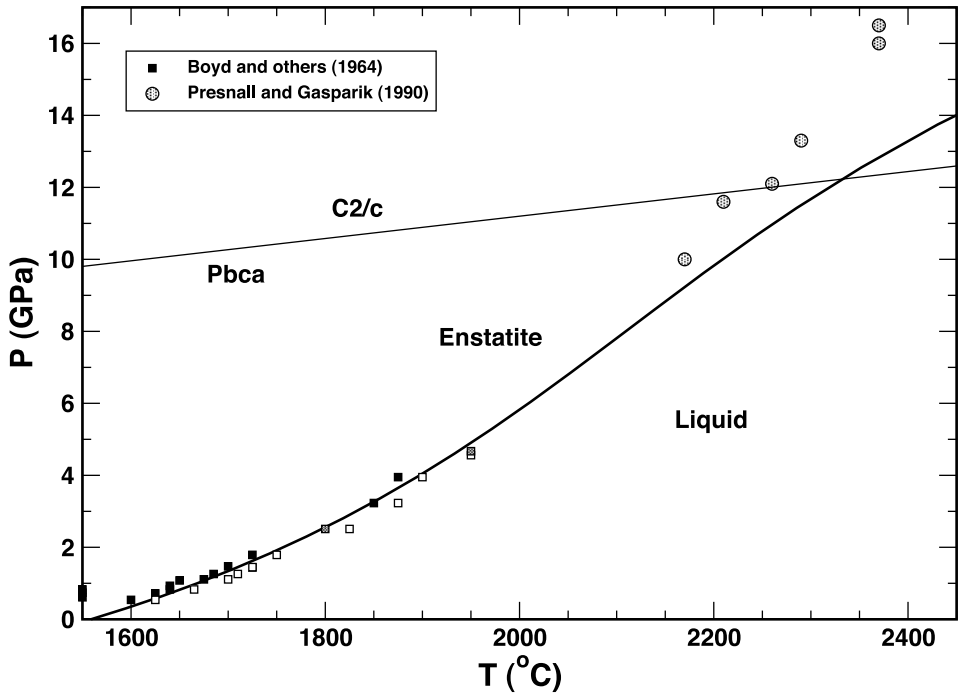

Fig. 10. Experimental data delimiting the fusion curve of enstatite ($Mg_2Si_2O_6$). Filled symbols indicate no melting, open symbols indicate complete melting, and gray-filled symbols the onset of melting. The solid curve is the calculated fusion curve of the *Pbca* structure based on the liquid EOS parameters and ancillary thermodynamic properties listed in table 2. The orthoenstatite-clinoenstatite transition curve is taken from Pacalo and Gasparik (1989).

gives the modeled density variation of the metastable reference state liquid. At elevated temperatures the CN variation is a more continuous function of pressure and the density-pressure curve would have a more constant slope. It should be borne in mind that the slope of the density-pressure curve is inversely proportional to the bulk modulus of the liquid. Figure 11 makes apparent that pressure-induced CN transformations render the pressure dependence of the bulk modulus (K' in the standard EOS models) a complex non-linear function of pressure.

Combined analysis of the enstatite fusion curve and MD results for $Mg_2Si_2O_6$ liquid demonstrate that the reference pressure parameter values of Part II are internally consistent with these data sets except for the reference temperature volume. Significantly, the thermal expansion and sound speed calculated from the Part II parameterization appear to be applicable to this magnesium silicate composition, which is not the case for Mg_2SiO_4 liquid. These observations suggest some non-linear mixing behavior with respect to volume and its temperature and pressure derivatives is present in the Mg-rich end of the system MgO-SiO_2. Along this binary join, liquidus temperatures for compositions where the molar ratio of MgO/SiO_2 exceeds unity, are high enough that reference pressure experimental measurements of density and sound speed are extremely difficult. A systematic molecular dynamics study aimed at resolving the nature of volumetric mixing relations in MgO-SiO_2 would shed light on the issue and resolve the compositional restrictions on extrapolating the Part II parameters to liquids in this simple system.

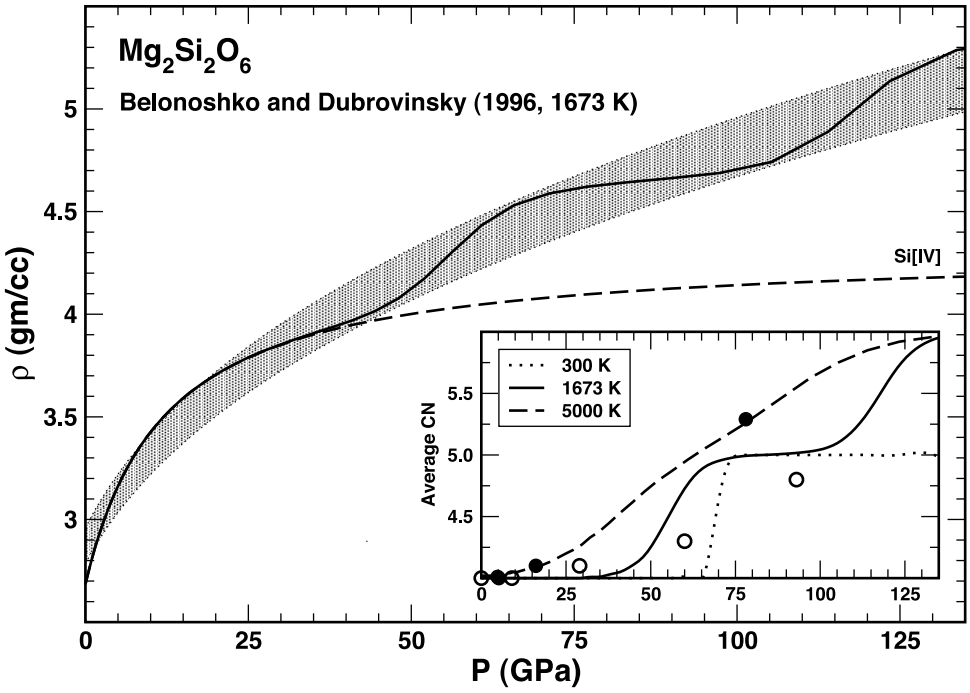

Fig. 11. Analysis of molecular dynamics simulations of melt density of $Mg_2Si_2O_6$ liquid. The gray band represents density estimates (± 3%) computed at 1673 K from the parameterization of Belonoshko and Dubrovinsky (1996). Values represented by the heavy solid line are computed for an equilibrium state of Si CN from the liquid EOS parameters listed in table 2; the dashed line gives density variation with pressure in a metastable CN state of Si[IV]. The inset shows average CN of Si computed at three different temperatures; solid circles correspond to average Si CN estimates from Wasserman and others (1993) at 4500-5000 K and the open circles are estimates from Kubicki and Lasaga (1991) at 300 K.

$CaMgSi_2O_6$ (Diopside liquid)

Three kinds of data are available to constrain the density of $CaMgSi_2O_6$ liquid at pressures above ambient: (1) the experimentally determined fusion curve of diopside to 15 GPa, (2) the liquid shock compression Hugoniot which has been determined to 36 GPa, and (3) molecular dynamic simulations which have been performed at pressures up to 28 GPa and at temperatures to 6000 K. Additionally, the molecular dynamics simulations of Matsui (1996) provide estimates of the CN of Si in $CaMgSi_2O_6$ liquid to pressures of 20 GPa.

The temperature and entropy of fusion of diopside ($CaMgSi_2O_6$) are adopted from Richet and Bottinga (1984a) for analysis of the fusion curve; the value for the entropy is within error of that reported by Lange and others (1991). The heat capacity of the solid phase is taken from Berman and Brown (1985) and that of the liquid is from Lange and Navrotsky (1992). Volumetric properties of the solid are compiled and fitted to a Universal EOS. Constants are reported in table 1 and data sources and residuals are indicated in figure 13.

Experimental data on the fusion curve are plotted in figure 14. The measurements of Boyd and England (1963), Williams and Kennedy (1969) and Boettcher and others (1982) were performed in piston-cylinder apparatus. The data set of Williams and Kennedy (1969) are plotted using two sets of temperatures. The solid black squares are raw data and the open squares are data corrected for the effect of pressure

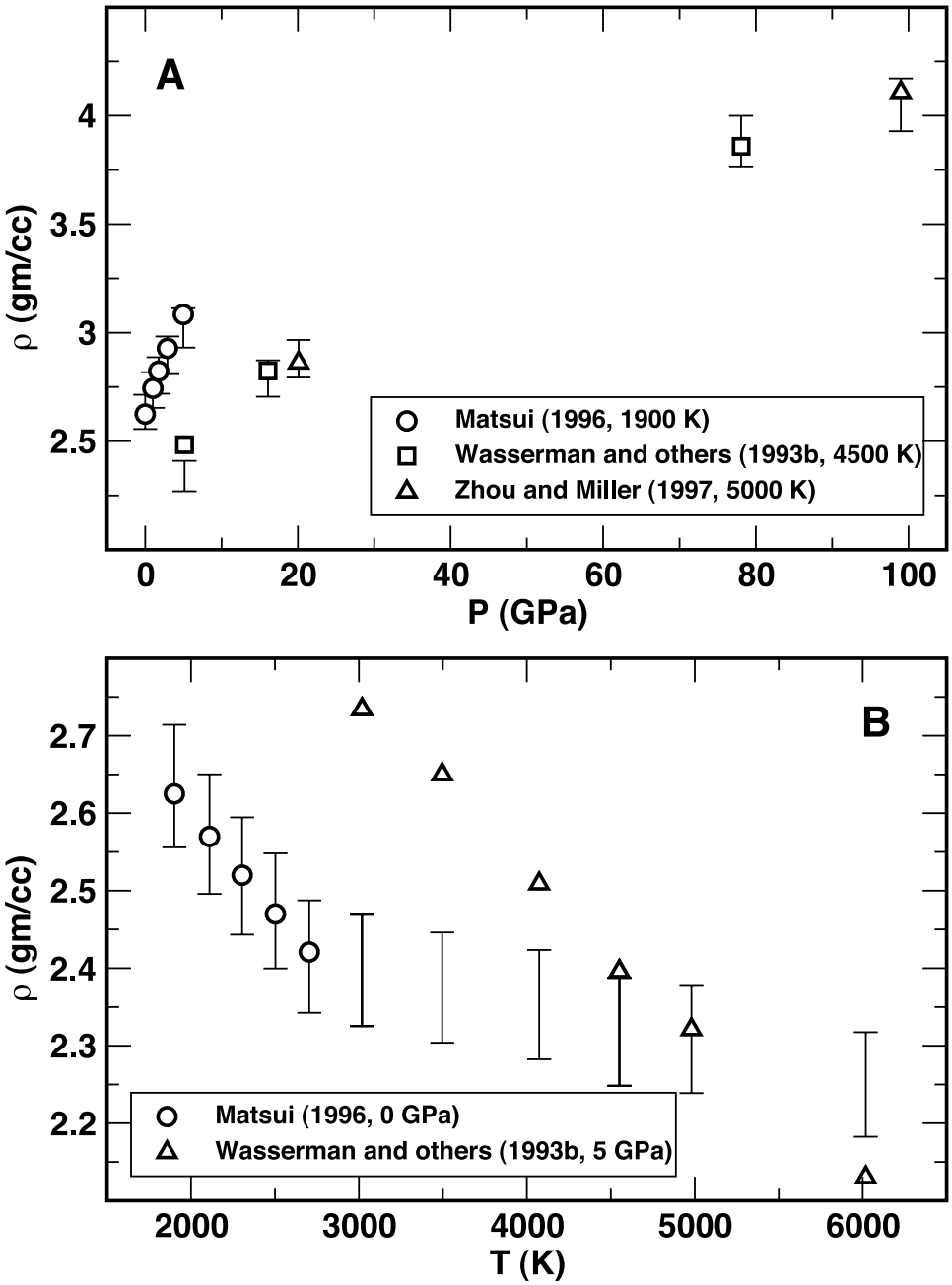

Fig. 12. Analysis of molecular dynamics simulations of melt density of $Mg_2Si_2O_6$ liquid. Brackets are density estimates from molecular dynamics simulations. Symbols are plotted at densities corresponding to an equilibrium state of Si CN from the liquid EOS parameters listed in table 2.

on the thermocouple. At the highest pressures the discrepancy between Boyd and England (1963) and Williams and Kennedy (1969) is most apparent; the main difference between the two sets of measurements is that the latter authors corrected

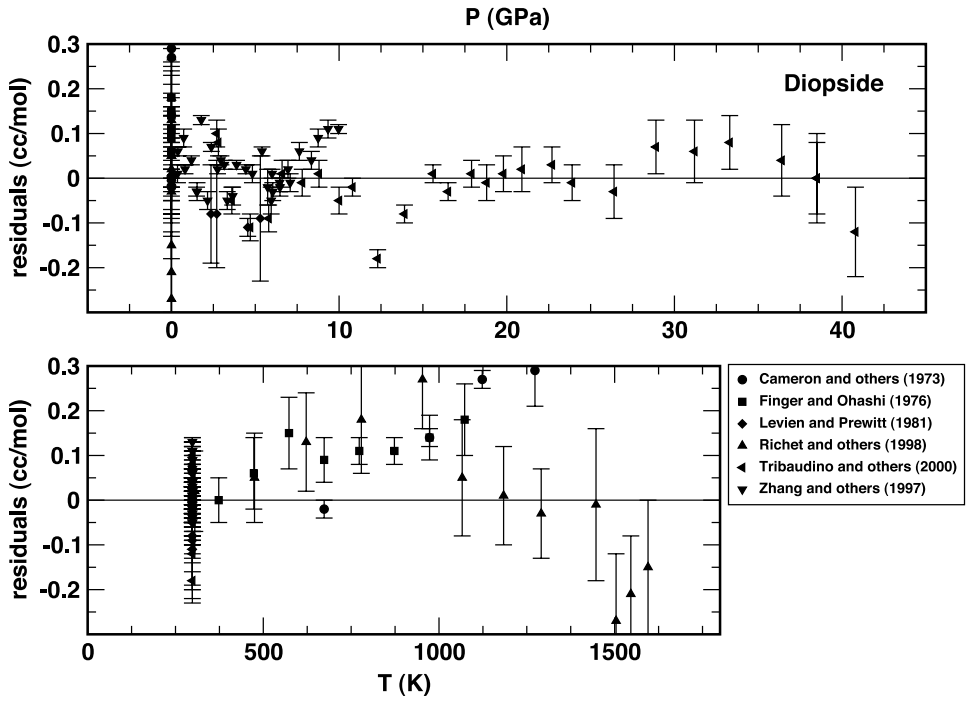

Fig. 13. Residuals (cc/mol) associated with a Universal EOS parameterization of volumetric data on diopside ($CaMgSi_2O_6$) as a function of temperature (lower panel) and pressure (upper panel). A residual of $\pm$ 0.66 cc/mol corresponds to a 1% relative error in the reference volume. EOS parameters are listed in table 1.

pressures for frictional losses. The data of Boettcher and others (1982) and Boyd and England (1963) are in agreement at pressures up to 2.5 GPa. The melting curve determinations of Scarfe and Takahashi (1986) were performed in multianvil type apparatus and seem to indicate that the fusion curve becomes vertical at temperatures on the order of 2000 °C. These observations should be compared to the measurements of Gasparik (1996) that indicate that the solid phase is stable to much higher temperatures. Gasparik (1996) also determined that the onset of incongruent melting of diopside (to Ca-perovskite) takes place at about 16 GPa.

Molecular dynamics simulations of melt density are reported in figure 15. In figure 16 the shock compression data of Rigden and others (1989) on the Hugoniot for $CaMgSi_2O_6$ liquid are plotted. Adopting reference pressure EOS parameters calculated from Part II, high-pressure parameters are optimized from the MD and shock wave measurements. To do this calibration two additional model parameters (f^V and P^V) are extracted that account for the CN change of Si from IV to V over the pressure range of interest (fig. 15). Resulting model parameters are reported in table 2[6]. Calculated densities and average Si CN are plotted in figure 15. The theoretical Hugoniot and an internally consistent set of shock temperatures are plotted in figure 16. The calculated fusion curve is plotted in figure 14.

[6] Parameter values for P^{VI} and f^{VI} are included for completeness. They have not been calibrated from any MD data set. P^{VI} is chosen at 50 GPa as the minmum pressure that prevents the formation of more than 1% Si[VI] in the 0-50 GPa range. f^{VI} is chosen to be identical to $CaAl_2Si_2O_8$ liquid so that intermediate binary liquids would exhibit no dependence of f^{VI} on composition.

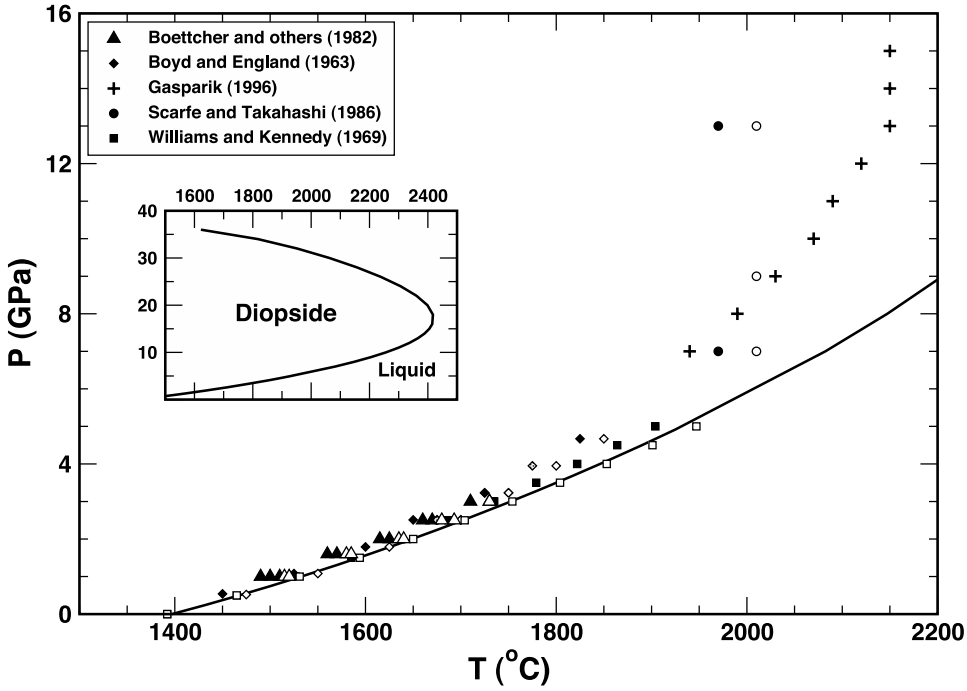

Fig. 14. Experimental data delimiting the fusion curve of diopside ($CaMgSi_2O_6$). Filled symbols indicate no melting, open symbols indicate complete melting, and gray-filled symbols the onset of melting. The curve is the calculated fusion curve based on the liquid EOS parameters and ancillary thermodynamic properties listed in table 2. The inset shows an extrapolation of the fusion curve to elevated pressure. The fusion curve is independent of the experimental data shown in this figure, and is calculated from parameters obtained in Part II and the analysis of shock compression data (fig. 16) and molecular dynamics simulations (fig. 15).

Recovery of the shock Hugoniot is excellent (fig. 16). The slope of the calculated Hugoniot increases at pressures above 19 GPa and Rigden and others (1989) speculated that this increase might reflect a "densification limit" in the liquid. The model developed here supports this interpretation. Densification of the liquid is enhanced by the continuous conversion of Si[IV] to Si [V] and this conversion takes place largely between ~10 and ~20 GPa (fig. 15C). Above these pressures, V-fold Si predominates, and by analogy with $Mg_2Si_2O_6$ liquid, VI-fold coordinated Si probably becomes abundant above the pressure range of available MD simulations and shock measurements. The slope of the Hugoniot in the high-pressure region reflects the vibrational bulk modulus, whereas the slope of the Hugoniot at lower pressure reflects an "enhanced" bulk modulus that includes the effects of configurational collapse. It could be argued that the high-pressure slope of the Hugoniot of $CaMgSi_2O_6$ liquid is "normal" and that the low-pressure slope reflects a "super-densification" regime.

The molecular dynamics simulations of Matsui (1996) are consistent with the reference pressure volume and thermal expansion (fig. 15B) and with the sound speed (compressibility, fig. 15A) derived from Part II. Recovery of the simulation results of Angell and others (1987) is more problematic. Model residuals show no systematic trends except for systematic underprediction of the density at extreme temperature. Whether this effect is real or an artifact of the interatomic potentials utilized in this study remains to be investigated.

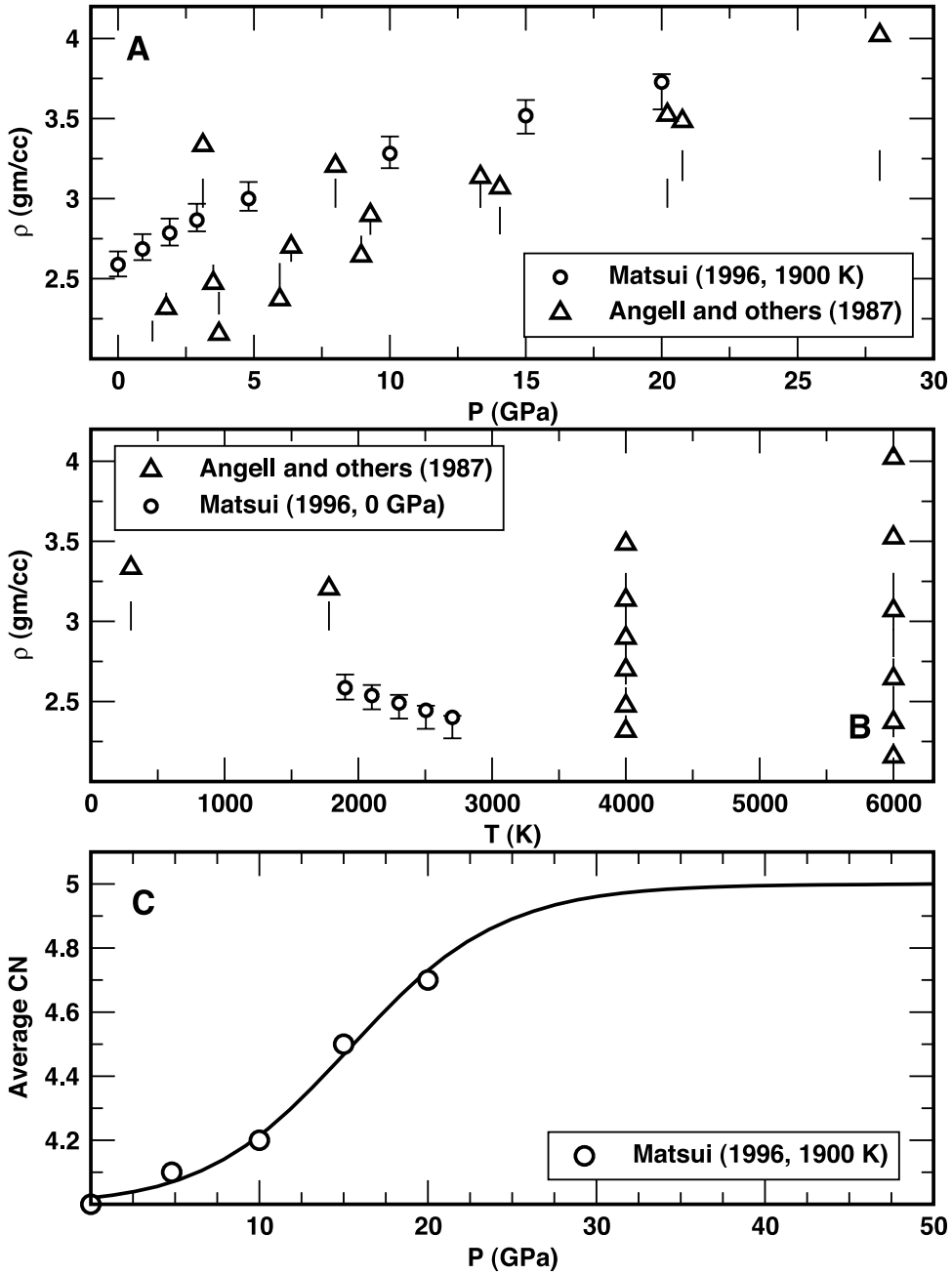

Fig. 15. Analysis of molecular dynamics simulations of melt density of $CaMgSi_2O_6$ liquid. Brackets in (A) and (B) are density estimates from molecular dynamics simulations. Symbols in (A) and (B) are plotted at densities corresponding to an equilibrium state of Si CN from the liquid EOS parameters listed in table 2. The solid curve in (C) shows average equilibrium CN of Si at 1900 K computed from the liquid EOS parameters listed in table 2.

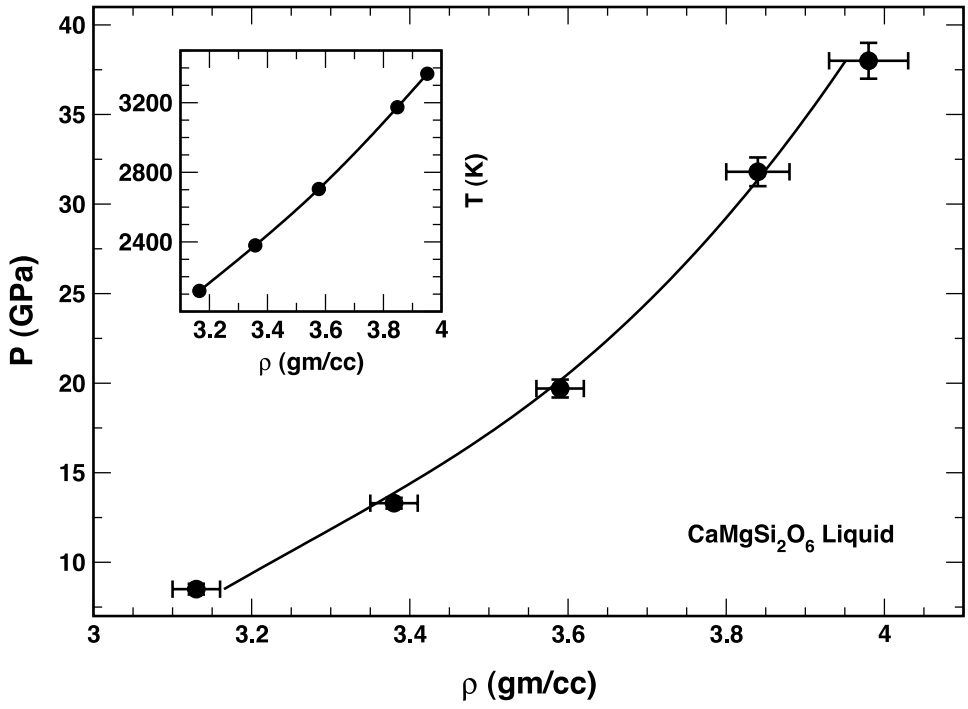

Fig. 16. Shock compression data (Rigden and others, 1989) and calculated shock Hugoniot (solid curve) for liquid of bulk composition $CaMgSi_2O_6$. Inset shows calculated shock temperatures plotted against calculated densities.

The model curve displayed in figure 14 is not fitted from the fusion curve data. It is calculated from the reference pressure properties of Part II (table 2) and the high-pressure EOS parameters obtained from the analysis of the shock compression and MD data. The model fusion curve agrees well with the "adjusted" brackets of Williams and Kennedy (1969) and with the lower pressure measurements of Boyd and England (1963). It is displaced to higher temperatures by ~10 to 15 °C from the experimental brackets of Boettcher and others (1982). Disagreement is found with the measurements of Scarfe and Takahashi (1986) and with those of Gasparik (1996). The calculated stability of the solid phase extends to a maximum T of 2417 °C at a pressure of 18 GPa (see inset in fig. 14). Gasparik (1996) reports a maximum on the diopside melting curve at 14 GPa and 2155 °C with a melt density determined at this T and P to be 3.40 ± 0.02 gm/cc. The model density calculated under the same conditions is 3.21 gm/cc, about 6 percent lower, indicating that the liquid is not dense enough to satisfy the phase equilibrium constraints. Adjusting the EOS calibration to satisfy the Gasparik (1996) reversals would compromise the fit to the Hugoniot and lead to unacceptable recovery of the shock compression data. There appears to be no resolution to this dilemma. Further molecular dynamics simulations may illuminate the problem if focused on the T-P range of interest.

SiO_2

As an illustrative example in Part I, a detailed analysis is undertaken to construct a thermodynamic model for SiO_2 liquid. This example was done to demonstrate application of the new EOS model to a well characterized liquid whose volumetric

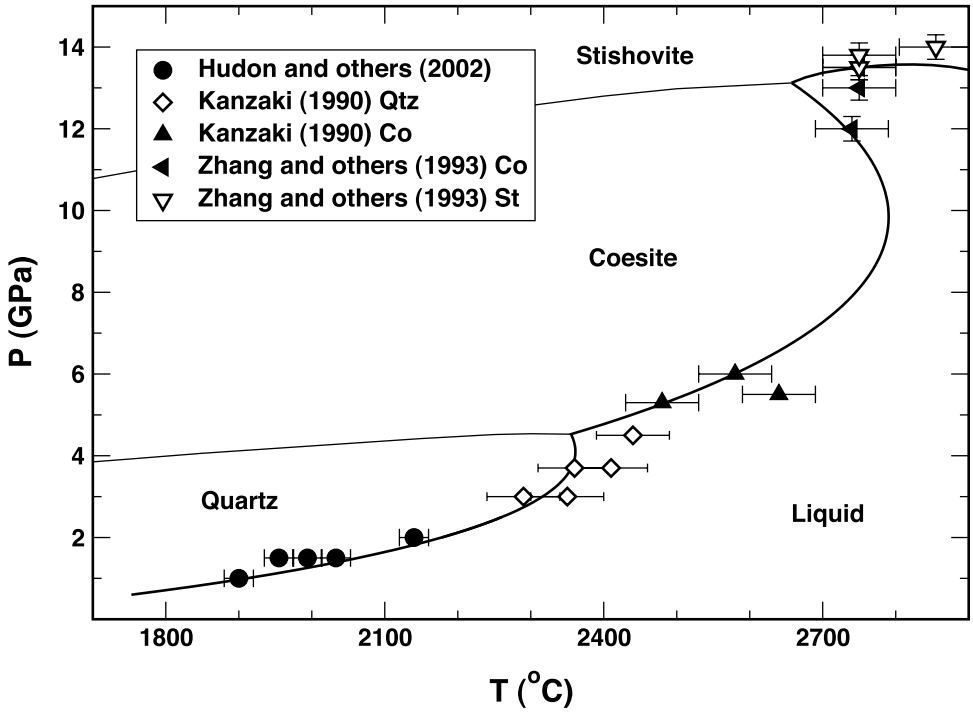

Fig. 17. Experimental data delimiting the fusion curve of the silica (SiO_2) polymorphs, quartz, coesite, and stishovite. This figure is a simplified version of the one presented in Part I; only reversal brackets are shown. The solid curve is the calculated fusion curve based on the liquid EOS parameters and ancillary thermodynamic properties listed in table 2.

properties are strongly influenced by configurational effects. Data on the fusion curves of cristobalite, quartz, coesite and stishovite are summarized in Part I and molecular dynamics simulations of the properties of molten silica at both high-temperatures and high-pressures are reviewed. A thermodynamic model for speciation of IV-, V-, VI, VII- and VIII-coordinated Si is constructed and EOS parameters for the IV-CN reference state are extracted. The model in Part I is calibrated on the molecular dynamics data and the initial slope of the quartz fusion curve. The model derived reference pressure volume is found to be consistent within error of the experimentally determined density of molten SiO_2 liquid (Bacon and others, 1960). The resulting EOS parameter values from Part I are reported in table 2.

Fusion curves of the silica minerals may be predicted from the liquid model, the known entropy of fusion of quartz, and internally consistent thermodynamic properties of the other solid polymorphs. The result from Part I is replotted in figure 17. The only data shown in the figure are solid-liquid coexistence experiments.

Reference pressure properties of molten SiO_2 obtained in Part I are inconsistent with values calculated from the calibration of Part II. This inconsistency implies that the volumetric properties of SiO_2 liquid are not a good proxy for the equivalent partial molar properties of silica in a multicomponent silicate liquid. At present, it is not possible to determine the mole fraction of SiO_2 at which the calibration of Part II breaks down. Further experimental and molecular dynamical studies are necessary to give a quantitative answer to this question.

$Na_2Si_4O_9$

Diefenbacher and others (1998) performed molecular dynamics simulations of the density of $Na_2Si_4O_9$ liquid at 6000 K over the pressure range 0 to 115 GPa. They also provide data on the proportions of $Na_2Si_4^{IV}O_9$, $Na_2Si_4^{V}O_9$, and $Na_2Si_4^{VI}O_9$ over the pressure range 0 to 30 GPa. These results are plotted in figure 18. Adopting EOS parameter values for reference pressure properties of $Na_2Si_4O_9$ liquid from Part II, the density is calculated to be 1.61 gm/cc at 6000 K, which should be compared to the MD value of 1.40 gm/cc. Assuming that the partial molar volume of SiO_2 from Part II represents largely Si[IV], it might be argued that appreciable concentrations of Si[V] in this liquid at these temperatures (fig. 18A) makes extrapolation of the Part II calibration problematic. However, as the presence of Si[V] would most likely densify the melt, this effect would exacerbate the difference rather than explain it. Most likely, the discrepancy arises from extrapolating the Part II model some 4000 K above the range of calibration. On the assumption that the MD results are systematically offset by the same amount along the entire isotherm, MD densities are adjusted upwards by 0.21 gm/cc to bring the reference pressure datum into agreement with the Part II calibration. Alternatively V_{0,T_r} or α_{T_r} could be adjusted from their Part II values to achieve the same agreement. As the focus is on the pressure dependence of the density of the liquid, and as the MD data all fall along an isotherm, the choice of which correction procedure to use is arbitrary. The simpler of the two is chosen here.

High-pressure (V_2, V_3, V_4) and thermodynamic (f^V, P^V, f^{VI}, P^{VI}) parameters are optimized from the density-adjusted MD data. The resulting values are given in table 2 and model results are plotted in figure 18.

The CN speciation model for the liquid is extrapolated in figure 18B to elevated pressure (dashed curves). At pressures above 80 GPa, most of the Si is predicted to be in VI-fold coordination with O. At higher pressures the model density systematically under predicts the MD results, and this result suggests that Si[VII] or Si[VIII] may constitute a significant fraction of the Si under these conditions, analogous to molten SiO_2 (Rustad and others 1991a). The MD data demonstrate that $Na_2Si_4O_9$ liquid doubles its density in the first 10 GPa of compression. This increase in density gives rise to a large and negative value for V_2 which implies a negative K' at 0 pressure (the model value is -0.73). With increasing pressure, the model K' becomes positive reaching large values (> 25) at pressures above 20 Gpa. As the EOS parameters apply to the reference liquid structure ($Na_2Si_4^{IV}O_9$) these effects cannot be attributed to a proxy for configurational collapse and probably represent a value for the compressibility (K) at zero pressure that is too small.

$CaAl_2Si_2O_8$ (Anorthite liquid)

An extensive data set of molecular dynamical simulations of melt density and structure are available for $CaAl_2Si_2O_8$ liquid. Si and Al coordination environments have been investigated as a function of both pressure (Nevins and Spera, 1998) and temperature (Morgan and Spera, 2001b). Data generated from these simulations are plotted in figure 19. The coordination statistics of $CaAl_2Si_2O_8$ liquid show a number of remarkable features. Firstly, Si and Al share common coordination states over the entire pressure-temperature range investigated. Secondly, at low pressures (1 GPa) and near the temperature of anorthite fusion, (Si, Al) exist primarily in V-fold coordination in the melt. Thirdly, unlike molten silica (Rustad and others, 1991a) and alkali aluminosilicates (Stebbins, 1991; Stebbins and Farnan, 1992), $CaAl_2Si_2O_8$ melts show an increase in the abundance of (Al,Si)[IV] over (Al,Si)[V] with increasing temperature. Fourthly, at low pressure (1 GPa) there is a significant fraction of (Al,Si)[VI] in the melt, and finally at moderate pressure ($\sim$30 GPa) more than 10 percent of (Al,Si) exists in CN $>$ VI. From these observations it can be anticipated that

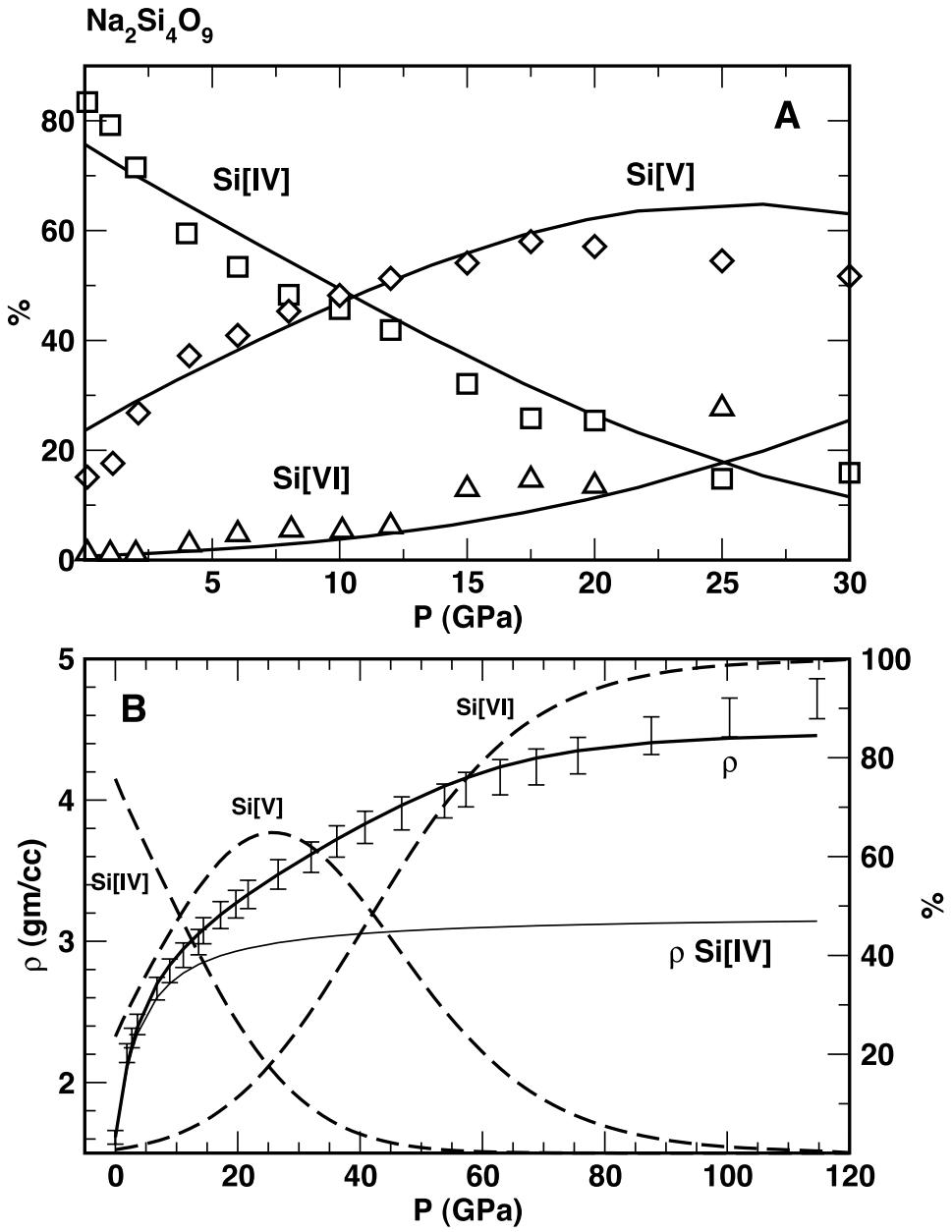

Fig. 18. Analysis of molecular dynamics simulations of melt density of $Na_2Si_4O_9$ liquid. (A) Symbols are estimates at 6000 K of Si CN calculated by Diefenbacher and others (1998). The solid curve is the calculated equilibrium distribution of Si CN based on the liquid EOS parameters listed in table 2. (B) Brackets denote adjusted (see text) estimates of density (± 3%) at 6000 K calculated by Diefenbacher and others (1998). Model derived equilibrium distribution of Si CN are indicated by the dashed curves. Density values given by the heavy solid line are computed for an equilibrium state of Si CN from the liquid EOS parameters listed in table 2; the light solid line gives density variation with pressure in a metastable CN state of Si[IV].

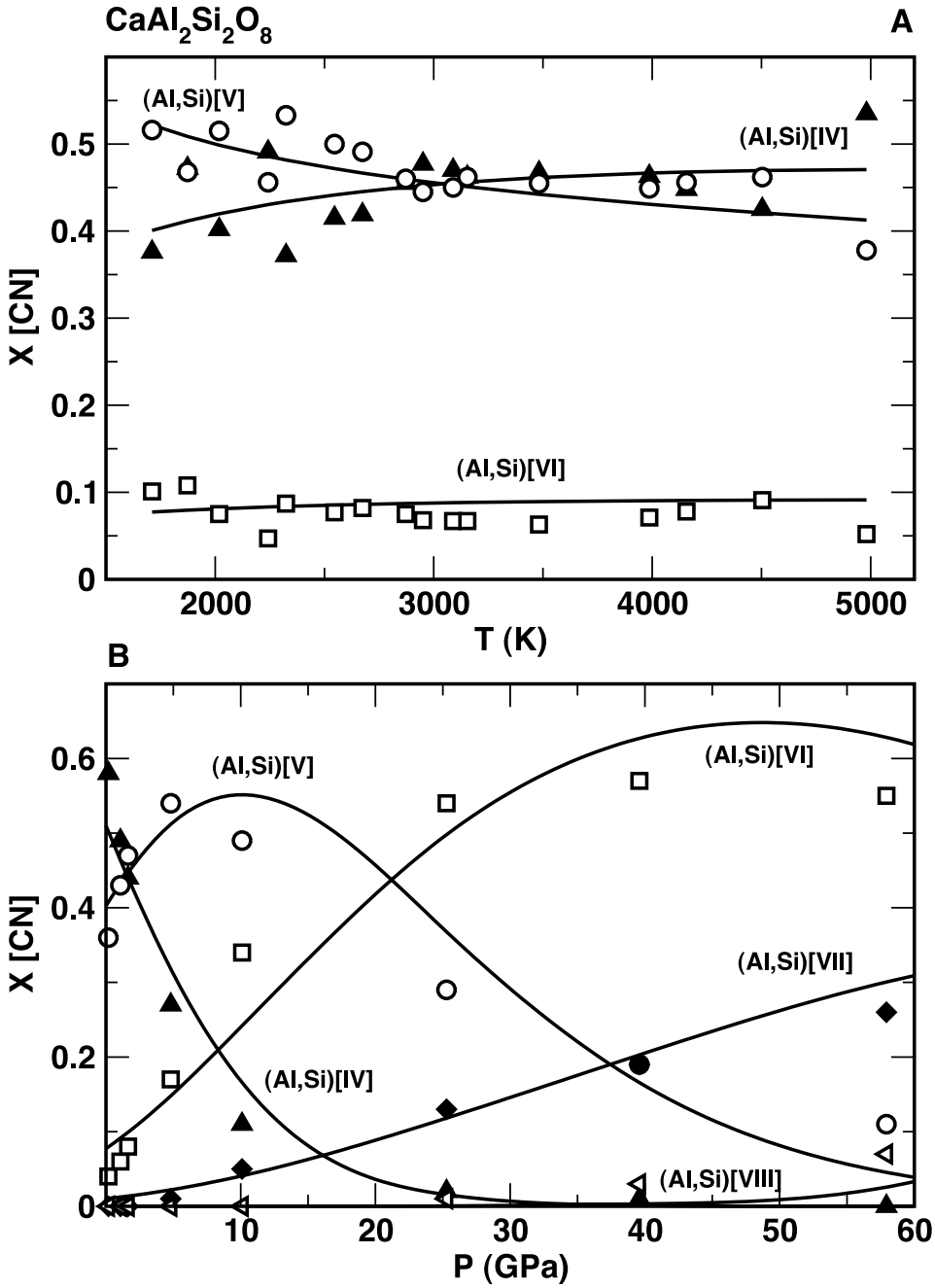

Fig. 19. Analysis of molecular dynamics simulations of cation coordination in $CaAl_2Si_2O_8$ liquid. The solid curves are the calculated equilibrium distribution of (Al,Si) CN based on the liquid EOS parameters listed in table 2. (A) Symbols are estimates at 1 GPa of (Al,Si) CN calculated by Morgan and Spera (2001b). (B) Symbols are estimates at 4000 K of Si CN calculated by Nevins and Spera (1998).

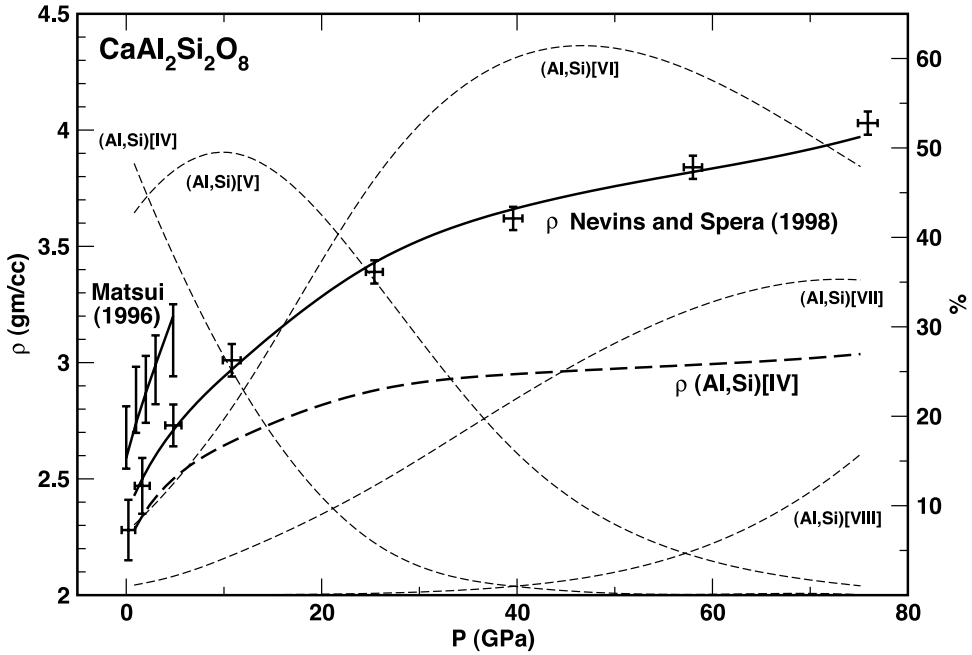

Fig. 20. Analysis of molecular dynamics simulations of melt density of $CaAl_2Si_2O_8$ liquid. Brackets denote density estimates at 4000 K calculated by Nevins and Spera (1998) and at 1900 K calculated by Matsui (1996); error brackets for the former are reported by the authors, otherwise errors are estimated at ± 3%. Model derived equilibrium distribution of (Al,Si) CN at 4000 K are indicated by the light dashed curves. Density values given by the heavy solid line are computed for an equilibrium state of (Al,Si) CN at the appropriate temperature from the liquid EOS parameters listed in table 2; the heavy dashed line gives density variation with pressure in a metastable CN state of (Al,Si) [IV].

configurational contributions to the volumetric properties of $CaAl_2Si_2O_8$ liquids should be of first order consequence.

Available results from molecular dynamics simulations of melt density are plotted in figures 20 and 21. In addition to the work of Spera and coauthors, Matsui (1996) reports density along an isotherm at 1900 K to 5 GPa and along the reference pressure isobar from the anorthite fusion temperature to 2700 K.

Shock compression data on $CaAl_2Si_2O_8$-liquid from Rigden and others (1989) are reported in figure 22.

The remaining high-pressure density constraint derives from data on the fusion of anorthite, which melts congruently from reference pressure to about 0.9 GPa and above that to the assemblage corundum plus liquid (Hariya and Kennedy, 1968). Available data on congruent melting of anorthite are plotted in figure 23. In order to model these data, volumetric properties of the solid are extracted from the parameterization of Berman (1988). He fitted volumetric measurements with a simple "polynomial" EOS of the form

$$V = V_{T_r,P_r}[1 + \nu_1(T - T_r) + \nu_2(T - T_r)^2 + \nu_3(P - P_r) + \nu_4(P - P_r)^2] \qquad (45)$$

In order to maintain consistency with the treatment for other solids in this paper, parameter values from Berman's EOS are recast into values for parameters of the

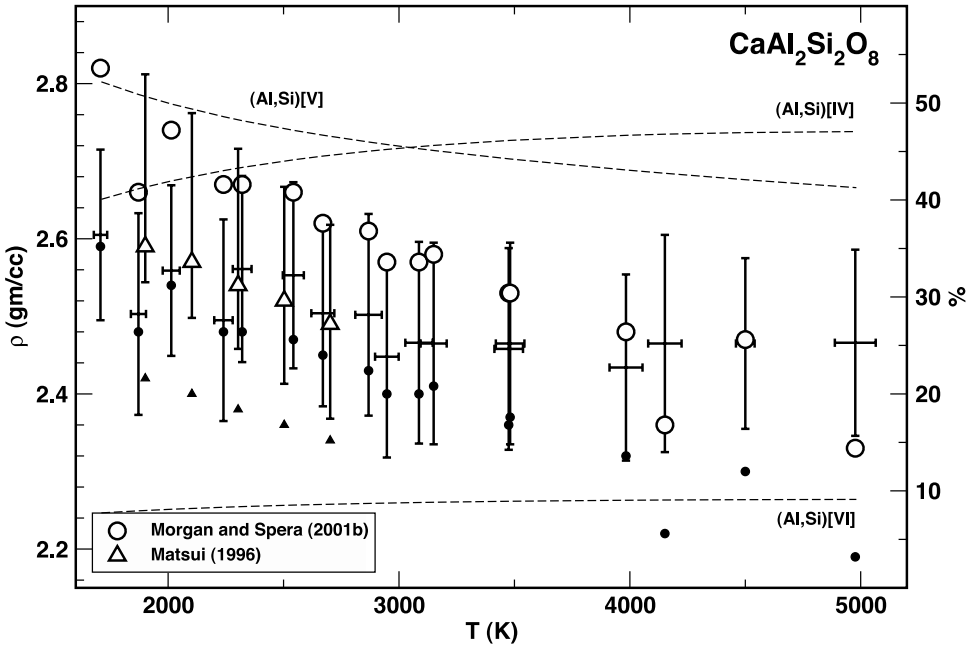

Fig. 21. Analysis of molecular dynamics simulations of melt density of $CaAl_2Si_2O_8$ liquid. Brackets denote density estimates at 1 GPa calculated by Morgan and Spera (2001) and at 0 GPa calculated by Matsui (1996); error brackets for the former are reported by the authors, otherwise errors are estimated at ± 3%. Model derived equilibrium distribution of (Al,Si) CN at 1 GPa are indicated by the light dashed curves. Density values given by the open symbols are computed for an equilibrium state of (Al,Si) CN at the appropriate pressure from the liquid EOS parameters listed in table 2; the smaller solid symbols give density in a metastable CN state of (Al,Si) [IV].

Universal EOS using a functional least squares approximation. The method involves constructing a functional squared residual (SR) that spans the calibration space of the original EOS, that is,

$$SR(\alpha, K, K') = \int_{P_{\min}}^{P_{\max}} \int_{T_{\max}}^{T_{\max}} (V^{Universal} - V^{Berman})^2 dT dP \qquad (46)$$

and minimizing this quantity with respect to α, K, and K'. The EOS parameter values of table 1 for anorthite are arrived at in this manner. The entropy of fusion of anorthite is taken as the average of the calorimetric values reported by Weill and others (1980) and Richet and Bottinga (1984a).

Reference pressure properties of $CaAl_2Si_2O_8$ liquid are obtained from the calibration of Part II and are listed in table 2. As the concentration of (Al,Si) [V] is appreciable at the reference temperature and pressure conditions (fig. 19A) it is unlikely that V_{0,T_r} computed from Part II will be applicable to this liquid composition. Consequently, in performing the analysis of the high-pressure data, this parameter is allowed to vary. The first attempt to extract optimal (V_2, V_3, V_4), high-pressure (V_2, V_3, V_4), and thermodynamic (f^V, P^V, f^{VI}, P^{VI}, f^{VII}, P^{VII}, f^{VIII}, P^{VIII}) parameters from the combined molecular dynamics, shock Hugoniot and fusion curve data sets failed to deliver an acceptable solution. The inconsistency is found to be in the shock compression data, specifically in the internal energy constraint derived from the shock Hugoniot,

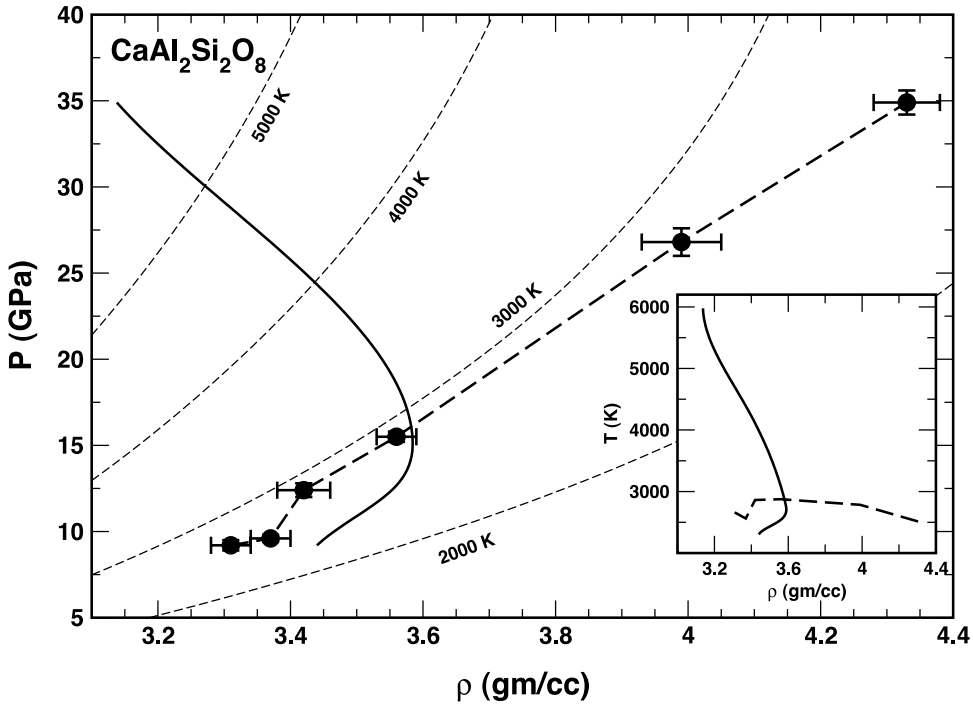

Fig. 22. Shock compression data (Rigden and others, 1989) and calculated shock Hugoniot for liquid of bulk composition $CaAl_2Si_2O_8$. Inset shows calculated shock temperatures plotted against calculated densities. The heavy dashed curve satisfies the shock density constraints *but not the internal energy constraint.* The solid curve attempts to satisfy both sets of constraints by adjusting shock temperature. Both curves utilize the same set of model EOS parameters (table 2), which are derived from the molecular dynamics simulations (figs. 19, 20, 21). The light dashed lines are isotherms consistent with EOS parameters obtained from the molecular dynamics data.

that is equation (12). Deleting this data set from the calibration generates an acceptable solution to the MD and fusion curve measurements. This solution is plotted in figures 19, 20, 21 and 23. Optimal parameter values are reported in table 2.

Recovery of MD density estimates is good both at elevated pressure (fig. 20) and elevated temperature (fig. 21). Matsui's (1996) reference pressure isotherm implies a somewhat smaller value for the thermal coefficient of expansion, but the model estimates are within error of the MD results. Similarly, Matsui's work supports a slightly smaller melt compressibility at low pressure (fig. 20), but the adopted value is consistent with the initial slope of the 4000 K isotherm of Nevins and Spera (1998). The optimized reference pressure volume of $CaAl_2^{IV}Si_2^{IV}O_8$ is 113.9 cc/mol and should be compared to the value computed from the Part II calibration, namely 107.1 cc/mol. A model volume at the same pressure and temperature conditions can be computed for $CaAl_2Si_2O_8$ liquid in an equilibrium distribution of CN states, and this is 106.1 cc/mol, within 1 percent of the Part II number. The agreement may be entirely fortuitous, but it does support the notion that the Part II calibration probably represents partial molar properties of oxide melt components in an average of equilibrium coordination numbers over the composition range of the calibrant density measurements. This is not to imply that the partial molar volume of SiO_2 and Al_2O_3 in part II represents Si and Al in mixed IV-, V-fold coordination. That is unlikely, unless the majority of compositions in the reference pressure density data set reflect this

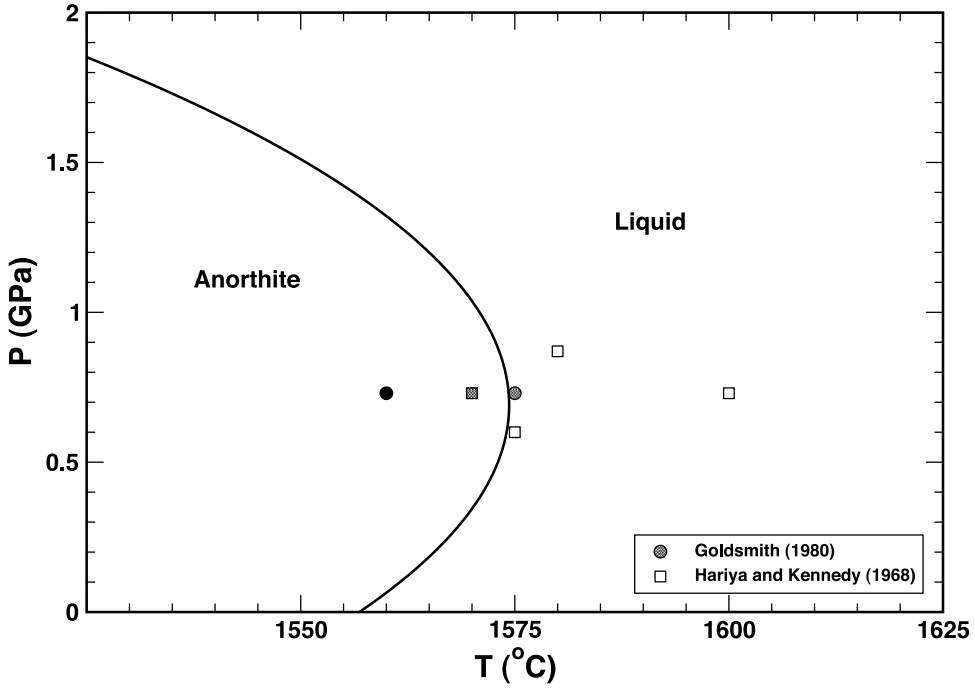

Fig. 23. Experimental data delimiting the fusion curve of anorthite ($CaAl_2Si_2O_8$). Filled symbols indicate no melting, open symbols indicate complete melting, and gray-filled symbols the onset of melting. The solid curve is the calculated fusion curve based on the liquid EOS parameters and ancillary thermodynamic properties listed in table 2.

coordination state of Si and Al in the liquid. More likely, the partial molar volume of CaO – a component that is not present in the majority of liquids in the Part II calibration data set – is compensating somehow for the configurational effects of changing CN of Si and Al. A reference pressure density model that incorporates the effects of composition and temperature on melt structure would be desirable and would help to resolve many of these issues, but data are not yet available to calibrate such a model over a broad composition range.

As noted above, the shock compression data of Rigden and others (1989) are inconsistent with the EOS calibration that satisfies the MD simulations and fusion curve brackets. In figure 22, a hypothetical Hugoniot that best satisfies the combined density and internal energy constraints is constructed from the model calibration. The Hugoniot is calculated by adjusting the shock temperatures to satisfy equations (11) and (12) in a least squares sense for each point on the measured Hugoniot. Effectively, this procedure weights the internal energy in preference to the density. The resulting solid curve plotted in the figure 22 reflects this weighting. The internal energy constraints drive the shock temperature to extreme values at elevated pressure. As is readily apparent in the figure, at these high temperatures the theoretical Hugoniot density is about 25 percent too low. For context the light dashed curves in figure 22 are isotherms calculated from the model calibration. The measured Hugoniot (heavy dashed curve) corresponds roughly to a model isotherm of ~2800 K; model temperatures that satisfy the $\rho - P$ relations *but do not satisfy the internal energy constraints* are shown by the heavy dashed line in the figure inset.

There is no obvious resolution to the misfit of the Hugoniot data of Rigden and others (1989). Either the molecular dynamics density results are in error or the measured Hugoniot documents the properties of a material that is not in an equilibrium structural state, and Rigden and others (1989) discount the possibility of a phase transition during shock propagation through the material. The issue remains unresolved until further MD simulation work or shock compression experiments are conducted.

The $NaAlO_2 - SiO_2$ Binary

Bryce and others (1999) report on a comprehensive set of molecular dynamics simulations of melt structure and density for five liquids along the binary join $NaAlO_2$ – SiO_2, specifically the compositions $NaAlO_2$, $Na_2Al_2SiO_6$, $NaAlSiO_4$, $NaAlSi_2O_6$, and $NaAlSi_3O_8$. The last three liquids have the stoichiometry of the minerals nepheline, jadeite and albite, respectively, and experimental data on the fusion curves of these minerals are available from the literature. The system therefore provides an excellent opportunity to test the internal consistency of a mixing model parameteriztion for the high-pressure volumetric properties of these sodium aluminosilicate liquids.

Two of the more remarkable conclusions of the work of Bryce and others (1999) are that (1) the CN of Al and Si are statistically indistinguishable and that (2) the oxygen CN of either Al or Si varies in a systematic fashion as a function of pressure and is only weakly dependent on the $NaAlO_2/SiO_2$ ratio. Coordination statistics from Bryce and others (1999) for $NaAlSiO_4$, $NaAlSi_2O_6$, and $NaAlSi_3O_8$ liquids are plotted in figure 24. The data correspond to simulation temperatures between 3500 and 6000 K and over this range there are no systematic temperature effects. In figure 25, melt densities are plotted for the same three liquids.

Experimental data delineating the fusion curves of albite ($NaAlSi_3O_8$), jadeite ($NaAlSi_2O_6$), and nepheline ($NaAlSiO_4$) are plotted in figures 26, 27 and 28. For thermodynamic analysis of these data, the volumetric properties of albite and jadeite are refitted to the Universal EOS from parameters reported by Berman (1988) using the functional least-squares method outlined above; results are reported in table 1. The entropy of fusion of albite is taken from the calorimetric measurements of Richet and Bottinga (1986). As jadeite melts incongruently to nepheline+liquid or albite+liquid at pressures below 3 GPa (Bell and Roseboom, 1969), the metastable fusion entropy at the reference pressure is adopted from Richet and Bottinga (1984b). The entropy of fusion of nepheline is taken from Stebbins and others (1983) and corresponds to the β-phase, which is the stable polymorph over the congruent melting interval studied by Smith (ms, 2003). The temperature of fusion of β-nepheline is estimated from Stebbins and others (1983) by extrapolating the fusion curve of Smith (ms, 2003) to reference pressure. Other reference pressure thermodynamic properties for nepheline are taken from Waterweise and others (1995). Their thermodynamic analysis is internally consistent with Berman (1988).

Boettcher and others (1982) observed that their experimental data on the albite fusion curve are inconsistent with those of Birch and LeComte (1960) and Boyd and England (1963) and are also at odds with reference pressure constraints on the Clapyron slope as derived from thermodynamic data. They criticize the experimental results of Boyd and England (1963) as reflecting contamination due to hydrogen (which would lower the melting point) and overstepping of the melting reaction (which would raise the apparent melting point). Boettcher and others (1982) propose a thermodynamic interpretation of their own data that involves reducing the activity of $NaAlSi_3O_8$ in the liquid via pressure dependent melt speciation.

The internal consistency of experimental observations on the albite fusion curve has been recently reviewed by Anovitz and Blencoe (1999) and by Lange (2003). The first authors conclude that none of the experimental data at elevated pressures are

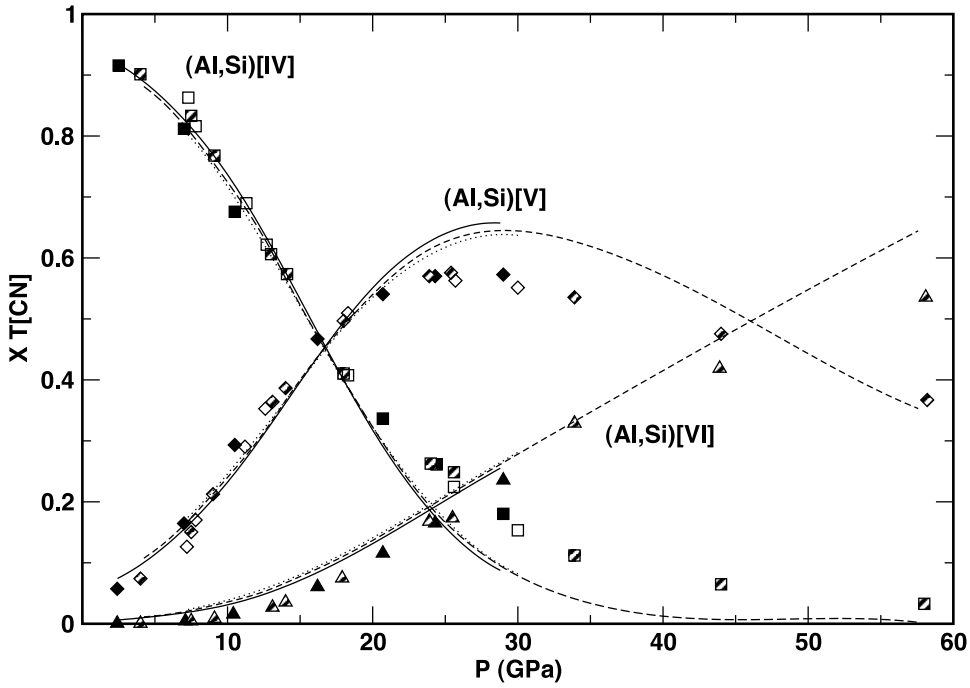

Fig. 24. Analysis of molecular dynamics simulations of (Al,Si) CN in binary liquids along the join $NaAlO_2$-SiO_2 (Bryce and others, 1999). Three compositions are plotted: $NaAlSiO_4$ (solid symbols), $NaAlSi_2O_6$ (diagonal-filled symbols), and $NaAlSi_3O_8$ (open symbols). Curves are fits to these data computed from the model EOS parameters of table 2. The solid line describes equilibrium CN in $NaAlSiO_4$ liquid, the dashed line $NaAlSi_2O_6$ liquid, and the dotted line $NaAlSi_3O_8$ liquid. The temperature range of the molecular dynamics simulations is 4000-6000 K; model curves are calculated at 5000 K.

reversed; at best they represent half reversals that constrain the onset of melting. Alternatively, Lange (2003) argues the veracity of the experimental brackets of both Boyd and England (1963) and Birch and Lecomte (1960). She suggests that the experiments of Boettcher and others (1982) are likely contaminated with water and consequently under predict the temperature of melting, a conclusion that was also suggested by Kress and others (1988). She reaches a similar conclusion regarding the more recent experiments of Nekvasil and Carroll (1996). Significantly, the lowest pressure reversal reported by Boettcher and others (1982; the datum is attributed by these authors to Modreski – see additional discussion in Lange, 2003) is in agreement with the Boyd and England (1963) calibration and is inconsistent with their higher-pressure brackets and reversals, supporting the contention that the Boettcher and others (1982) results are displaced at higher pressure due to the increasing solubility of volatiles in the liquid. Lange's (2003) preferred fusion curve (with Birch-Murnaghan EOS $K' = 10$) is plotted in figure 26.

Rather than use the fusion curve data for albite, jadeite and nepheline as constraints on the high-pressure EOS parameters, the approach to be followed here is to examine after the fact the internal consistency of these measurements with the molecular dynamics data and the reference pressure calibration of Part II. An additional aim of this exercise is to see if simple EOS parameter mixing relations can be devised that work for the silica rich side of the $NaAlO_2$-SiO_2 join.

The logical set of endmember components to choose to model the system are $NaAlO_2$ and SiO_2. Values for reference state EOS parameters of these endmembers

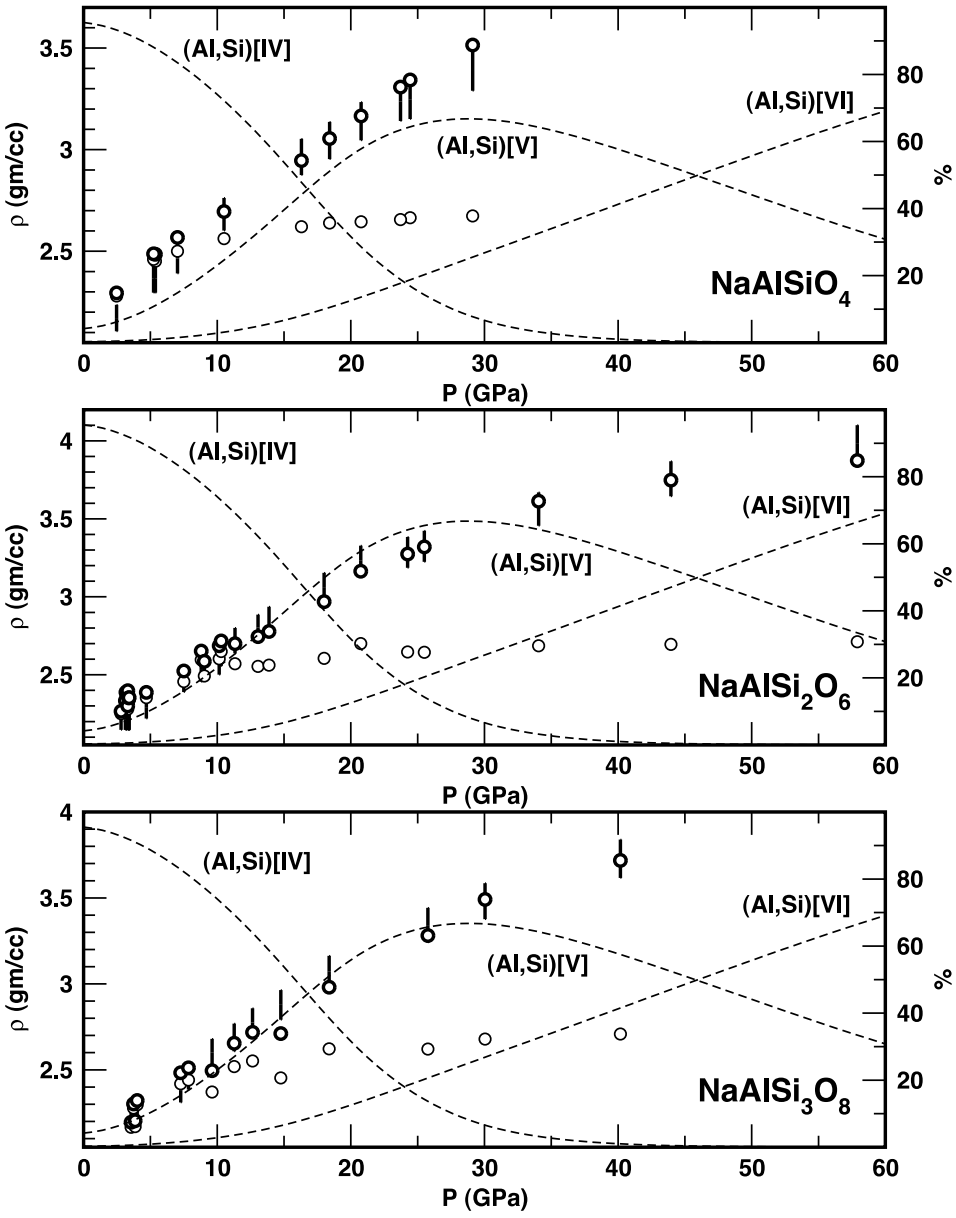

Fig. 25. Analysis of molecular dynamics simulations of density in binary liquids along the join $NaAlO_2$-SiO_2. Density values from Bryce and others (1999) are plotted as vertical chords assuming an uncertainty of ± 3%. Computed density estimates are calculated at the appropriate temperature from the EOS parameters of table 2 on the assumption of an equilibrium state of (Al,Si) CN. These values are denoted by the heavy symbols. The light symbols correspond to density estimates in a metastable state of (Al,Si) [IV] CN. The temperature range of the molecular dynamics simulations is 4000-6000 K; model (Al,Si) CN dashed curves are calculated at 5000 K.

and for intermediate compositions along the join are calculated from Part II. High-pressure EOS parameters (V_2, V_3, V_4) for each endmember component are optimized from the MD results along with a single set of thermodynamic parameters (f^V, P^V,

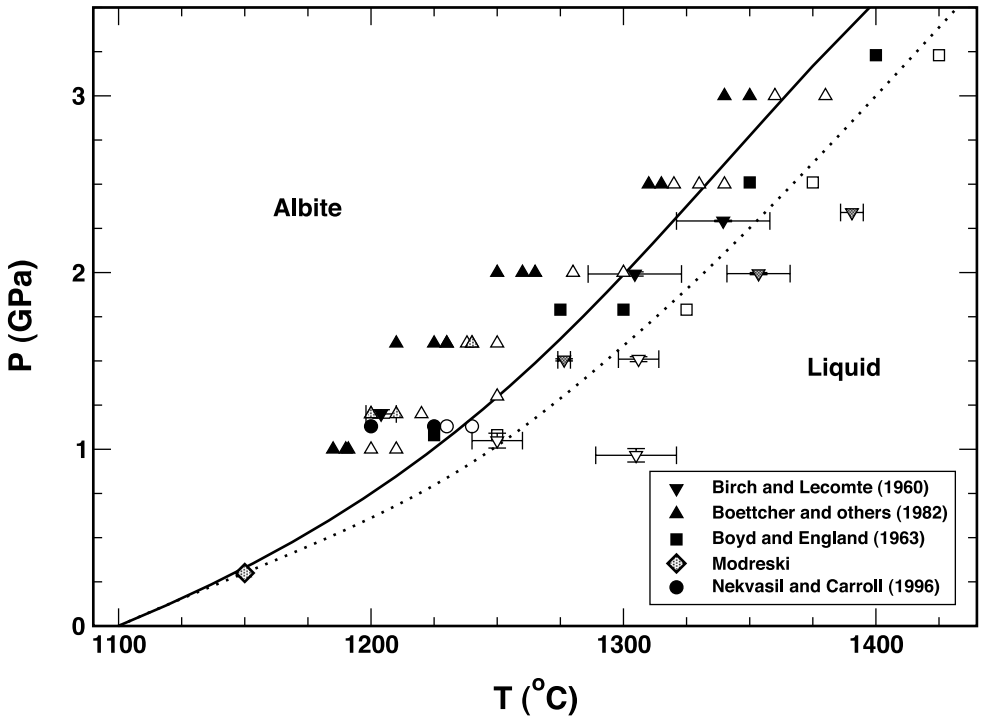

Fig. 26. Experimental data delimiting the fusion curve of albite ($NaAlSi_3O_8$). Filled symbols indicate no melting, open symbols indicate complete melting, and gray-filled symbols the onset of melting. The solid curve is the calculated fusion curve based on the liquid EOS parameters and ancillary thermodynamic properties listed in table 2. The dotted curve is the fusion curve calculated by Lange (2003) utilizing an independent analysis of liquid and solid standard state properties and an estimate of K′ for the liquid of 10.

f^{VI}, P^{VI}) that characterize CN speciation and accompanying configurational collapse in this system. Specific values of V_2, V_3, and V_4 for intermediate compositions are calculated assuming simple linear mixing relations between endmembers. Parameters are optimized from the MD data and are reported in table 2. Model curves are plotted in figures 24 and 25.

Recovery of the CN distribution results is very good to pressures of 25 GPa and above that pressure the amount of (Al,Si)[IV] is under predicted at the expense of (Al,Si)[V] (fig. 24). Densities are recovered within the 3 percent uncertainty level for all three intermediate compositions. Significant CN effects on density are seen above pressures of 5 GPa. These effects are apparent in figure 25 from examination of the displacement of the plotted light and dark circles. The former correspond to metastable (Al,Si)IV-coordinated liquid densities while the latter are densities calculated in an equilibrium state of (Al,Si) CN. Over the range of pressures corresponding to experimental data on the fusion curves of these sodium aluminosilicates the effect of CN on melt density is negligible.

A hypothetical fusion curve for albite is calculated from the EOS parameters reported in table 2 and from thermodynamic data on the solid phase summarized above. The model curve is plotted in figure 26. The initial slope of the fusion curve is very similar to that obtained by Lange (2003), the difference between them results from her use of an experimental measurement of $NaAlSi_3O_8$ liquid volume whereas the one used here is calculated from the multicomponent parameterization of Part II.

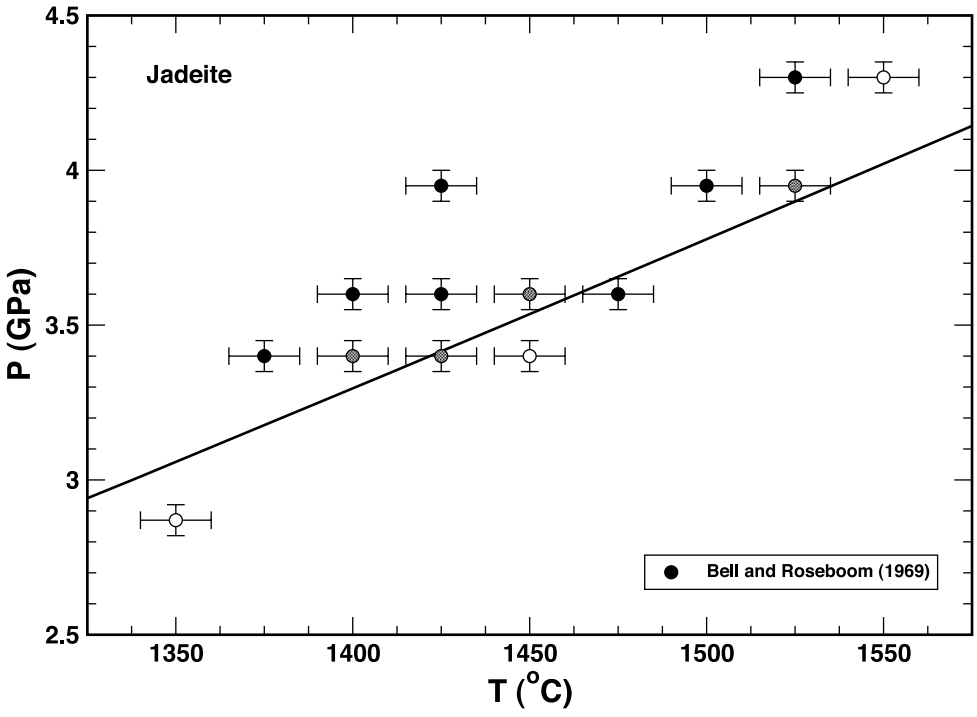

Fig. 27. Experimental data delimiting the fusion curve of jadeite ($NaAlSi_2O_6$). Filled symbols indicate no melting, open symbols indicate complete melting, and gray-filled symbols the onset of melting. The solid curve is the calculated fusion curve based on the liquid EOS parameters and ancillary thermodynamic properties listed in table 2.

The model curve also reflects a smaller effective value of K' at lower pressures than preferred by Lange (2003). At the reference pressure K' is calculated to be 5.3, it increases to a value of ~10 at 0.5 GPa, and climbs to ~20 at 2.5 GPa. The model fusion curve is consistent with the reversal attributed to Modreski (see above) and with reversals at 1 GPa of Nekvasil and Carroll (1996). At higher pressures the slope of the model curve becomes steeper to almost satisfy the brackets of Boettcher and others (1982).

A model fusion curve for jadeite cannot be constructed without first specifying a metastable reference pressure temperature of fusion (T_{fus}). Richet and Bottinga (1984b) estimated a value of 1100 ± 200 K on the basis of a linear extrapolation of the Clapyron slope defined from the experimental brackets of Bell and Roseboom (1969). As the Clapyron slope of the fusion curve is probably not constant over a pressure range of ~3 GPa, an alternative method of determining T_{fus} is adopted here. T_{fus} is optimized by finding a value that causes the model fusion curve to best satisfy the experimental brackets. The resulting T_{fus} is 820 K and the model curve is plotted in figure 27. With the exception of the highest-pressure bracket of Bell and Roseboom (1969), the slope of the model fusion curve accounts correctly for the remaining experimental brackets, from which it can be inferred that the EOS mixing parameters are consistent with the volumetric properties of the melt derived from the fusion curve.

A model fusion curve for nepheline can be constructed given an estimate of the molar volume of the solid. Waterweise and others (1995) report a reference temperature/pressure volume of nepheline and recommend an isobaric thermal expansivity

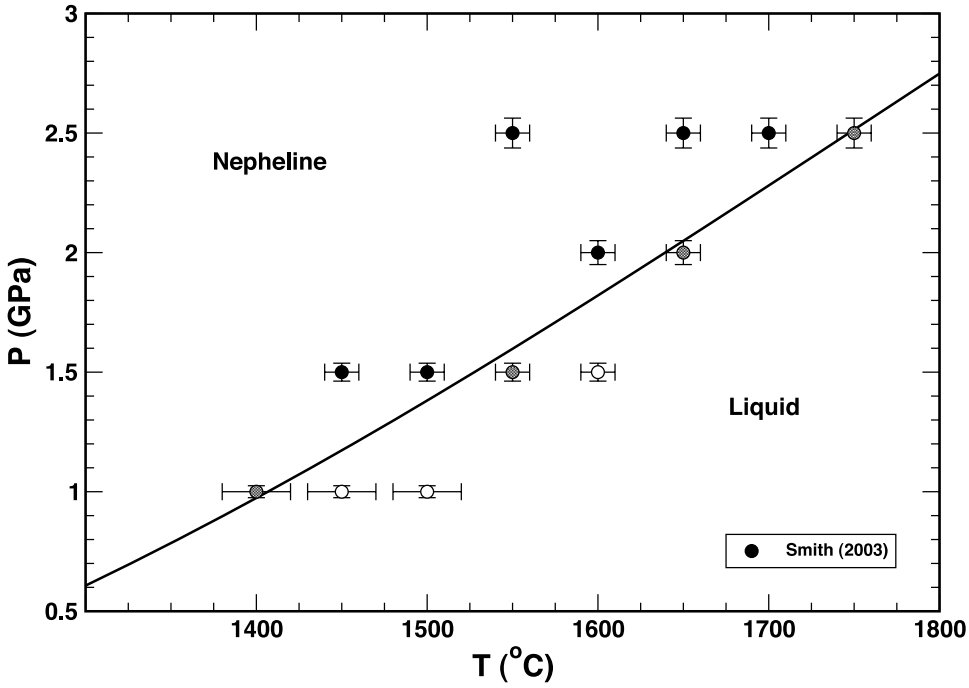

Fig. 28. Experimental data delimiting the fusion curve of nepheline ($NaAlSiO_4$). Filled symbols indicate no melting, open symbols indicate complete melting, and gray-filled symbols the onset of melting. The solid curve is the calculated fusion curve based on the liquid EOS parameters and ancillary thermodynamic properties listed in table 2.

from Skinner (1966) and an isothermal compressibility from Birch (1966). The reference volume was averaged from a number of sources including measurements on naturally occuring nephelines and on material synthesized experimentally in albite+nepheline+jadeite assemblages. Natural nepheline and nepheline grown under these conditions is not likely to be stoichiometric (for example, Sack and Ghiorso, 1998, their fig. 1), and probably contains considerable excess silica. The material on which the thermal expansion data are reported is actually a nepheline-kalsilite solid solution of composition $(NaAlSiO_4)_{0.78}(KalSiO_4)_{0.22}$ (Skinner, 1966) and the value is not applicable to the stoichiometric endmember. Given the cumulative uncertainties on the volume of the solid, a somewhat arbitrary decision is made to adopt Waterweise and others' (1995) thermal expansion and compressibility, and adjust the reference pressure solid volume to optimize the modeled fusion curve to the reversals of Smith (ms, 2003). The resulting fusion curve is shown in figure 28. Alternatively, adjustment to the thermal expansion of the solid or to the extrapolated fusion temperature at reference pressure could produce model curves that similarly match the reversal brackets.

Although each of the mineral fusion curves in the $NaAlO_2$-SiO_2 system poses difficulties to interpretation and analysis, in can be concluded from the results presented above that the molecular dynamics simulations constrain densities of liquids in this system to be broadly consistent with the phase equilibrium data. More importantly, the MD results established that simple mixing models which include melt speciation can be constructed that allow application of the liquid EOS over a broad range of compositions in this binary.

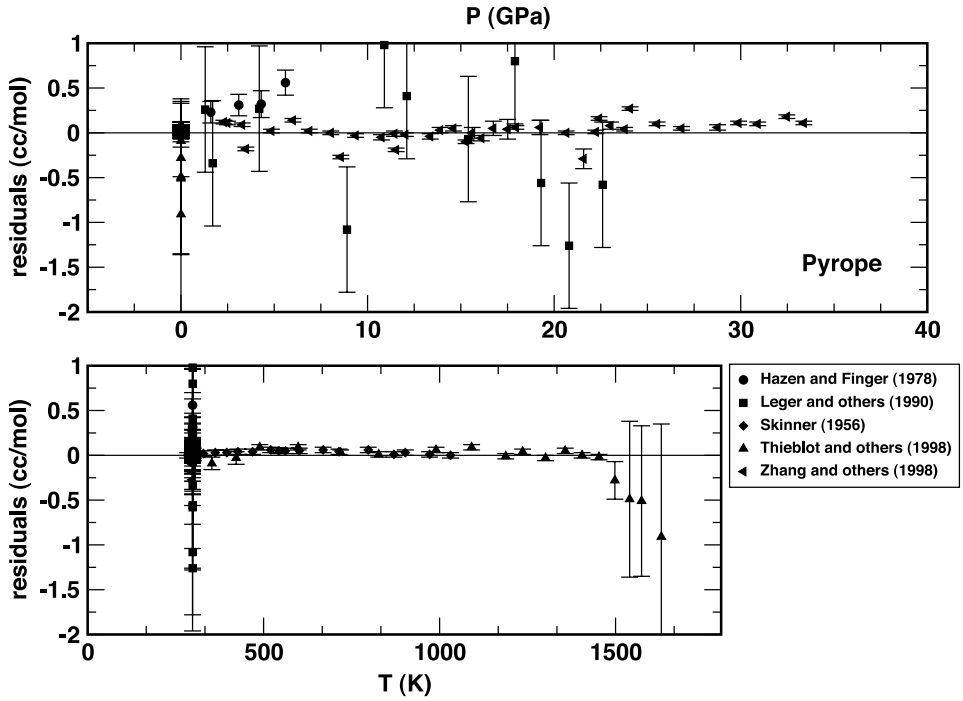

Fig. 29. Residuals (cc/mol) associated with a Universal EOS parameterization of volumetric data on pyrope garnet ($Mg_3Al_2Si_3O_{12}$) as a function of temperature (lower panel) and pressure (upper panel). A residual of ± 1.13 cc/mol corresponds to a 1% relative error in the reference volume. EOS parameters are listed in table 1.

$Mg_3Al_2Si_3O_{12}$ (Pyrope liquid)

There are no direct measurements of melt density nor are there molecular dynamics simulations of $Mg_3Al_2Si_3O_{12}$ liquid at pressure. There are however, experimental constraints on the pyrope fusion curve. Pyrope melts congruently at pressures above 3.5 GPa (Boyd and England, 1962). The metastable fusion temperature and entropy of fusion at the reference pressure are reported by Tequi and others (1991). The heat capacity of the solid is given by Berman and Brown (1985). Newly derived Universal EOS parameters for pyrope are listed in table 1, and model residuals of volumetric properties are summarized in figure 29.

The fusion curve from 3.5 to 5 GPa was determined by Boyd and England (1962) using piston cylinder apparatus. Ohtani and others (1981) extended the curve to 10 GPa using multianvil apparatus and Irifune and Ohtani (1986) performed an extensive series of experiments in both piston cylinder and multianvil apparatus over the pressure range 3.5 to 10 GPa. Results of all three studies are plotted in figure 30.

In the absence of quantitative estimates of the CN of Si and Al in these liquids at pressure, the fusion curve is fitted without making explicit provision for configurational effects. As it is likely that Si and Al are in V- and VI-fold coordination in $Mg_3Al_2Si_3O_{12}$ liquid at pressure, this approach places the burden of absorbing the consequences of configurational collapse onto the high-pressure parameters of the liquid EOS. Adopting reference pressure parameters from Part II, V_2, V_3 and V_4 are fitted from the reversal brackets. The optimized values are reported in table 2 and the model fusion curve is plotted in figure 30.

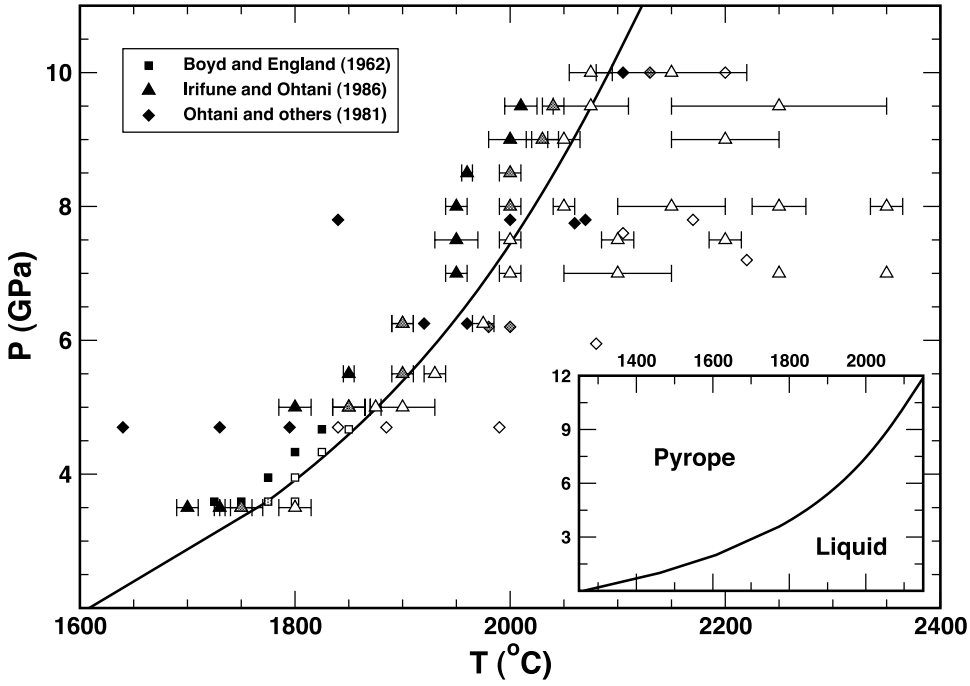

Fig. 30. Experimental data delimiting the fusion curve of pyrope garnet ($Mg_3Al_2Si_3O_{12}$). Filled symbols indicate no melting, open symbols indicate complete melting, and gray-filled symbols the onset of melting. The curve is the calculated fusion curve based on the liquid EOS parameters and ancillary thermodynamic properties listed in table 2. The inset shows an extrapolation of the fusion curve to elevated pressure.

A satisfactory fit to the fusion curve requires a negative value for V_2. This requirement implies that the compressibility is initially enhanced with increasing pressure and continues until some pressure is reached where the positive V_3 term dominates. The V_2 parameter induces a strong curvature to the fusion curve in the 6 to 7 GPa range, and this curvature is reflected in the high-pressure data sets. Irifune and Ohtani (1986) attribute this curvature to a coordination change of aluminum in the melt induced by pressure, with a tetrahedral to octahedral transition taking place in the 6 to 7 GPa range. The configurational collapse associated with this CN change would enhance the effective melt compressibility and in the absence of a speciation model, a negative V_2 EOS parameter value would be required. So, Irifune and Ohtani's (1986) interpretation is consistent with the analysis developed here, but it is also possible that the high-pressure EOS parameters are compensating for inaccuracies in the reference pressure properties of the liquid computed from Part II. If V_{0,T_r} were too large, for example, the compressibility of the melt would need to be enhanced in order to match the Clapyron slope of the fusion curve, effectively inducing a negative value for V_2. Low pressure experimental constraints on the density of $Mg_3Al_2Si_3O_{12}$ liquid or molecular dynamics simulations of melt structure are required in order to resolve this issue. The fusion curve fit at $P > 5$ GPa is a compromise between the data set of Ohtani and others (1981) and that of Irifune and Ohtani (1986). The curvature (and magnitude of V_3) is exaggerated if the earlier studies are down weighted in the analysis.

$KAlSi_3O_8$ (Sanidine liquid)

The partial molar volume of K_2O in multicomponent silicate liquids at elevated pressures is largely constrained by experimental data on the fusion curve of sanidine;

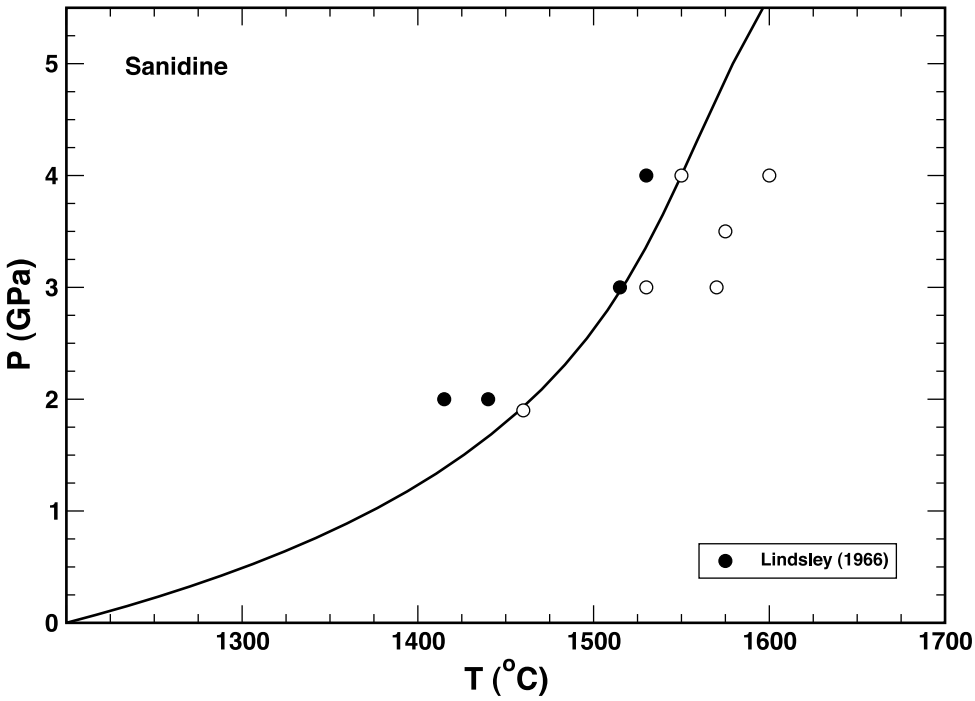

Fig. 31. Experimental data delimiting the fusion curve of sanidine ($KAlSi_3O_8$). Filled symbols indicate no melting, open symbols indicate complete melting, and gray-filled symbols the onset of melting. The solid curve is the calculated fusion curve based on the liquid EOS parameters and ancillary thermodynamic properties listed in table 2.

results of phase equilibrium studies by Lindsley (1966) are plotted in figure 31. Sanidine melts incongruently to leucite ($KAlSi_2O_6$) plus liquid at pressures below 2 GPa (Lindsley, 1966). To model the fusion curve, estimates of the reference pressure fusion temperature and entropy made by Stebbins and others (1984) are adopted.

By analogy with spectroscopic observations made on alkali-silicate glasses quenched from high pressure (for example, Wolf and McMillan, 1995), it is likely that $KAlSi_3O_8$ liquid will have (Al,Si) coordination states broadly consistent with $NaAlSi_3O_8$ liquid. *If that assumption holds* then the MD results of Bryce and others (1999; fig. 25) support the notion that the effect of configurational collapse (essentially the % of Si[>IV]) is negligible on melt density up to pressures of 5 GPa. Following on with this assumption, it should be possible to model the sanidine fusion curve below this pressure without accounting explicitly for configurational contributions to the liquid volume. The modeled fusion curve in figure 31 is obtained by optimizing the high-pressure EOS parameters of the liquid and by adopting reference pressure properties from Part II. The optimized value of V_2 is positive, which supports the assumption to ignore configuration effects in treating these data.

$CaTiSiO_5$ (Titanite liquid)

The fusion curve of titanite provides constraints on the volumetric properties of Ti-bearing melts at pressure. In order to evaluate the fusion curve, the temperature and entropy of fusion, and the high-temperature heat capacity of titanite are adopted from Tangeman and Xirouchakis (1999). Volumetric properties are taken from

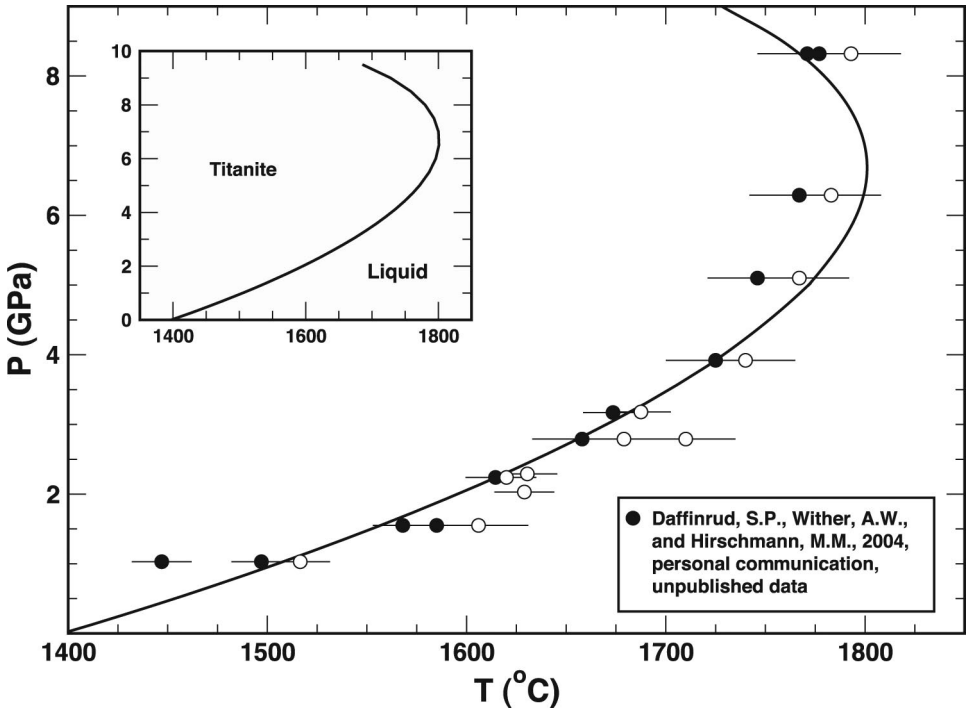

Fig. 32. Experimental data delimiting the fusion curve of titanite ($CaTiSiO_5$). Filled symbols indicate no melting, open symbols indicate complete melting, and gray-filled symbols the onset of melting. The solid curve is the calculated fusion curve based on the liquid EOS parameters and ancillary thermodynamic properties listed in table 2. The inset shows an extrapolation of the fusion curve to elevated pressure.

Berman (1988) and refitted (as described above) to a Universal EOS form (table 1), but the bulk modulus is corrected to reconcile the discrepancies between the Berman (1988) model and newer volume measurements at pressure (Tangeman and Xirouchakis, 1999).

The CN of Ti in glass of composition $CaTiSiO_5$ is [VI] (Farges, 1997) and presumably the coordination state of Ti^{4+} in the corresponding liquid is similar. The effect of pressure on the CN of Ti and Si in $CaTiSiO_5$ liquid is not known.

Fusion curve determinations for titanite are plotted in figure 32 and include the piston cylinder and the multi-anvil studies of S.P. Daffinrud, A.W. Wither, and M.M. Hirschmann (2004, personal communication, unpublished ms). The data are modeled by adopting reference pressure liquid properties from Part II. Higher-order EOS parameters are optimized and configurational volume effects are neglected. A model fusion curve is shown in figure 32. EOS parameters are reported in table 2. As both the reference pressure volume and the sound speed for $CaTiSiO_5$ liquid are well constrained in the Part II calibration, the fit to the fusion curve brackets at low pressures is excellent. The fit near the region of maximum curvature is not as good at higher pressures as it is at lower pressures. This fact suggests that some structural modification in either the liquid or solid is not being accounted for. Alternatively, there could be a volumetric effect accompanying reduction of Ti^{4+} to Ti^{3+}; with Ti^{3+} being stabilized in the melt at elevated temperature. These possibilities warrant further investigation and suggest a prime target for future molecular dynamics simulations of Ti-bearing melts.

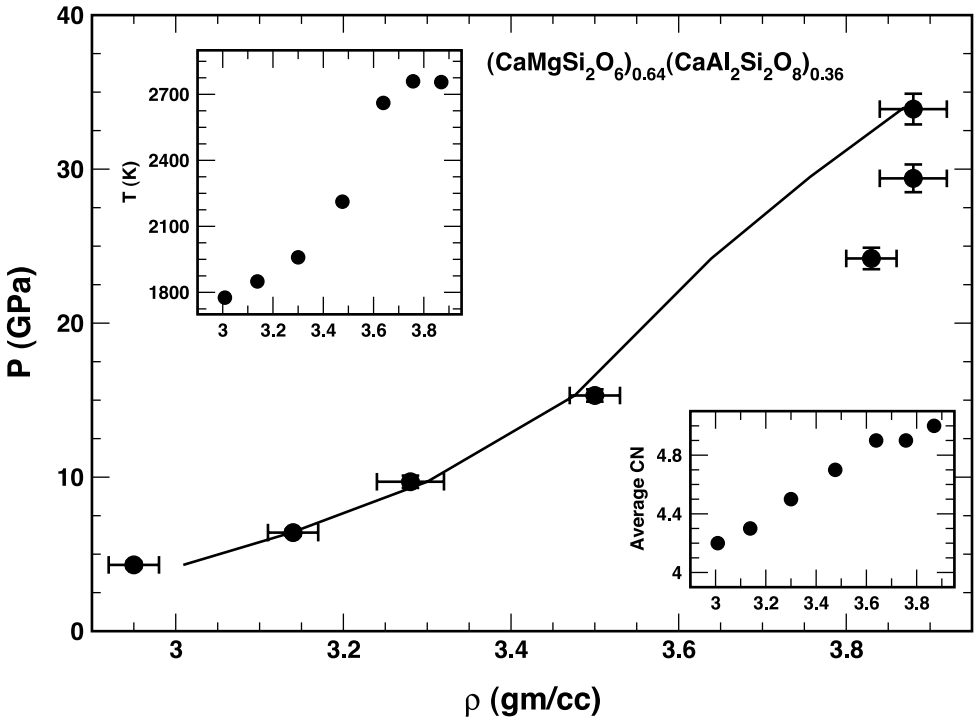

Fig. 33. Shock compression data (Rigden and others, 1984, 1988) and calculated shock Hugoniot (solid curve) for liquid of bulk composition $(CaMgSi_2O_6)_{0.64}(CaAl_2Si_2O_8)_{0.36}$. Left inset shows calculated shock temperatures plotted against calculated densities. Right inset shows calculated average (Al, Si) CN plotted against calculated density.

Shock Compression Studies on Chemically Complex Liquids

In the remainder of this section, shock compression studies on three chemically complex liquids are analyzed. Although these data will be treated again in Part IV along with sink-float measurements on melts of similar composition in the context of a mixing model for high-pressure EOS parameters, the pressure-temperature systematics of each composition are worth exploring here so that comparison can be drawn between these compositions and the simpler system "mineral-like" stoichiometric liquids discussed above.

64% $CaMgSi_2O_6$ – 36% $CaAl_2Si_2O_8$.—Shock compression measurements of Rigden and others (1984, 1988) on liquids of composition $(CaMgSi_2O_6)_{0.64}$-$(CaAl_2Si_2O_8)_{0.36}$ are plotted in figure 33. This composition corresponds to eutectic melting along the diopside-anorthite join, and is often taken as a simple analogue melt for basaltic magma. The data points define a Hugoniot that exhibits a behavior unlike that of either the $CaMgSi_2O_6$ (fig. 16) or $CaAl_2Si_2O_8$ (fig. 22) endmember. The "stiffening" of the melt suggested by the Hugoniot for $CaMgSi_2O_6$-liquid above 25 GPa is exaggerated in this mixed composition with the *experimentally determined* bulk modulus becoming indistinguishable from infinity at high pressure. None of the "densification" seen in the Hugoniot for $CaAl_2Si_2O_8$-liquid is manifest in this intermediate composition.

A theoretical Hugoniot is calculated with the following procedure. Reference pressure EOS parameters are obtained from Part II. High-pressure EOS parameters (namely V_2, V_3, V_4) for $CaMgSi_2O_6$ and $CaAl_2Si_2O_8$ liquid calibrated previously are

adopted (table 2). A linear mixing model is applied to these parameters in order to calculate coefficients for the mixed liquid. These are reported in table 2; note that the extensive parameters are scaled to adjust for the gram-formula-weight of the mixed composition.[7] The *modified* reference pressure/temperature volume for $CaAl_2Si_2O_8$ liquid is not adopted for the mixed composition on the assumption that (Al,Si)[IV] is the principal coordination state at reference pressure. A CN speciation model for the mixed liquid is imposed by constructing a linear combination of f^V, P^V, f^{VI}, and P^{VI} from the previous analysis of the endmember liquids (table 2). The Hugoniot is obtained by optimizing shock temperatures to satisfy simultaneous constraints on melt density and internal energy. The resultant curve is plotted in figure 33. Also shown are derived shock temperatures and inferred average (Al,Si) CN for homogeneous equilibrium along the *T-P* path of the Hugoniot.

Agreement between the measured and the calculated Hugoniot is very encouraging, and in this context it is worth restating that the theoretical curve is not fitted to these data. It is calculated entirely from the endmember properties. The data points at ~24 and ~29 GPa are not captured by the model curve. This fact could be due to a number of factors, but most likely arises from some inadequacy in the adopted CN-speciation model. The internal energy constraint is what drives the temperatures on the model curve higher for these two data points and consequently lowers the calculated density.

When considering figure 33 it should be borne in mind that the endmember EOS properties of $CaMgSi_2O_6$ liquid are entirely consistent with shock compression measurements to ~38 GPa (fig. 16) but that the EOS parameters for $CaAl_2Si_2O_8$ liquid only approximate the shock Hugoniot at $P < 15$ GPa (fig. 22) and fail miserably to do so at higher pressure. The high-pressure EOS parameters for $CaAl_2Si_2O_8$ are derived entirely from molecular dynamics simulations. Perhaps the agreement between the datum at ~34 GPa and the model Hugoniot is fortuitous, or perhaps the MD results have uncovered an inconsistency with the shock studies on molten $CaAl_2Si_2O_8$. Only further experimental work and molecular dynamics simulations will resolve this issue, and such work will also serve to better constrain mixing models and melt CN-speciation for this important eutectic composition.

Komatiite and MORB liquids.—In figure 34, data on the shock compression of a komatiitic composition liquid (Miller and others, 1991) are plotted. Data from Rowan (ms, 1993) on molten MORB is plotted in figure 35.

The komatiite composition of Miller and others (1991) can be approximately represented as a liquid in the system $MgSiO_3$-Al_2O_3-Ca_2SiO_4-Fe_2SiO_4 with proportions 76 percent, 9 percent, 8 percent, and 8 percent respectively. The CN-speciation in this melt at elevated pressures should probably reflect the behavior of the dominant melt component, $MgSiO_3$. As an approximation, the f^V, P^V, f^{VI}, and P^{VI} derived above for $Mg_2Si_2O_6$ liquid (table 2) are adopted and a CN-speciation model is applied to the sum of Si+Al in the system. Reference pressure EOS parameters are calculated from Part II and high-pressure parameters (V_2, V_3, V_4) are optimized from the experimental data. The calculated shock Hugoniot along with an internally consistent set of shock temperatures are plotted in figure 34. Agreement between experimental data and model Hugoniot is excellent except for the datum at ~36 GPa. Interestingly, the calculated (Al,Si)[V] for this point is ~18 percent of the total Si+Al, and perhaps this is an overestimate that causes the calculated melt density to be ~1 percent too high.

[7] Coefficients are calculated for 100 gm of $(CaMgSi_2O_6)_{0.64}$-$(CaAl_2Si_2O_8)_{0.36}$ liquid. There are 1.676 moles of oxides (SiO_2 + Al_2O_3 + MgO + CaO) in this amount of material. A linear combination of 0.64 moles of $CaMgSi_2O_6$ and 0.36 moles of $CaAl_2Si_2O_8$ has 4 moles of oxides, so each mixed coefficient is weighted by 1.676/4.

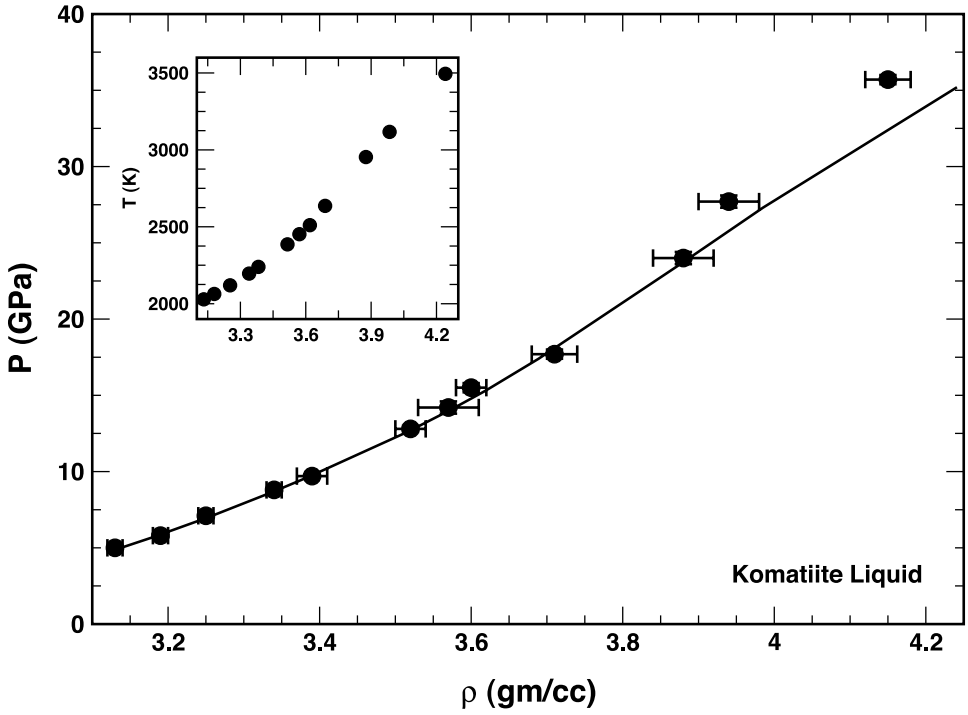

Fig. 34. Shock compression data (Miller and others, 1991) and calculated shock Hugoniot (solid curve) for liquid of komatiitic composition. Inset shows calculated shock temperatures plotted against calculated densities.

The datum at ~28 GPa is consistent with this notion as it is also displaced slightly to the left of the model curve, and the calculated (Al,Si)[V] is 5 percent of the total (at all other pressures CN > IV are negligible).

The MORB composition investigated by Rowan (ms, 1993) is a more chemically complex natural analogue of the $(CaMgSi_2O_6)_{0.64}$-$(CaAl_2Si_2O_8)_{0.36}$ liquid studied by Rigden and others (1984, 1988). As an approximation, the CN-speciation model of the latter is assumed for this natural composition liquid and appropriate values of f^V, P^V, f^{VI}, and P^{VI} are reported in table 2. Reference pressure EOS parameters are calculated from Part II; all iron is assumed to be reduced. High-pressure EOS parameters (V_2, V_3, V_4) are optimized from the experimental data along with an internally consistent set of shock temperatures by satisfying simultaneously the density and internal energy constraints. The resultant parameter values and model results are presented in table 2 and figure 35. Although the data themselves are not as internally consistent as other shock compression results on silicate liquids, the model Hugoniot faithfully captures the trend of the points, including the "incompressible"-like limiting behavior at elevated pressure. The verticality of the model Hugoniot at pressures > 15 GPa is interpreted here to be caused by an increase in shock temperature. The average CN of (Al,Si) steadily increases at $P > 15$ GPa, so along an isotherm, configurational collapse should cause the density of the melt to continue to increase with pressure. To match the internal energy of the shock however, the temperature must increase (see inset in fig. 35) and this increase offsets the effect of compression and of configurational collapse, causing the liquid to appear to be incompressible.

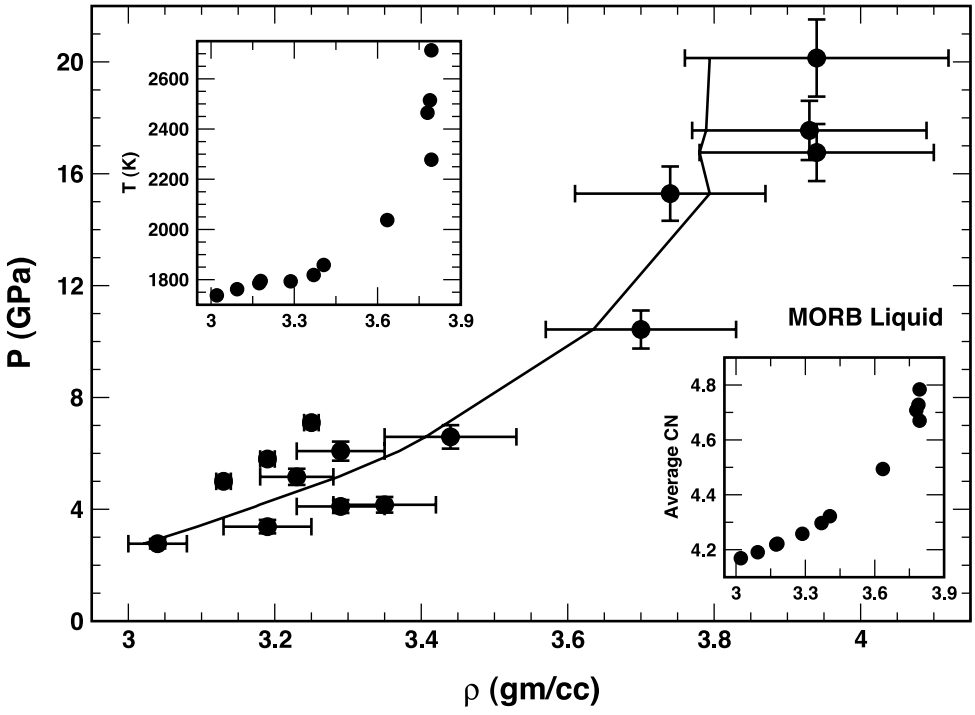

Fig. 35. Shock compression data (Rowan, ms, 1993) and calculated shock Hugoniot (solid curve) for liquid of MORB composition. Left inset shows calculated shock temperatures plotted against calculated densities. Right inset shows calculated average (Al,Si) CN plotted against calculated density.

The shock compression results on both komatiite and MORB composition melts demonstrate that the reference pressure parameters of Part II are applicable to natural composition melts and that values of high-pressure EOS parameters can be optimized to model these data. The results are especially encouraging because they lend some support to the notion that inferences of melt CN-speciation inferred from studies of simple system liquids can be carried over and applied to natural compositions to better understand the effects of configurational collapse on the densities of these melts at elevated pressure.

DISCUSSION

The analysis of shock compression data, molecular dynamics simulations and mineral fusion curves developed in this paper demonstrates that these data sets can be modeled using the liquid EOS developed in Part I. In particular, the variation of molar volume as a function of pressure in liquids that exhibit extreme variation in compressibility can be accommodated successfully as can liquids whose volumetric properties are dominated by configurational effects associated with coordination number transformations. Additionally, the analysis of these data sets establishes that the reference pressure model parameterization developed in Part II can generally be made internally consistent with the higher-pressure constraints. There are however, important exceptions to this generalization.

The model reference pressure molar volumes of Mg_2SiO_4 and $Mg_2Si_2O_6$ at the fusion temperatures of forsterite and enstatite are 6.9 percent and 3.5 percent larger than values inferred from either (1) the Clapyron slope of each melting curve, or (2)

density estimates calculated from molecular dynamics simulations. This discrepancy points to a failure in the volume of mixing model of Part II when extrapolated to melts in the MgO-SiO_2 binary, especially to Mg-rich liquids in this system. Furthermore, the sound speed mixing model from Part II (from which is calculated the compressibility of the melt) fails for Mg_2SiO_4 liquid (table 2). In the Part II calibration data set there are no constraints on densities or sound speeds of liquids with compositions within MgO-SiO_2. It is an interesting exercise to attempt to refit the model density calibration of Part II by imposing constraints on the liquid volumes for these high Mg/Si melts as inferred from the analysis developed here. The resultant model does not represent the reference pressure volume data set at the level of accuracy attained previously, implying that there is a non-linear volume of mixing effect associated with highly-magnesian silicate liquids. Further experimental investigation is warranted as well as additional molecular dynamics simulations.

The model calibration of Part II also fails to account for the properties of pure SiO_2 liquid. Two factors are important here. Firstly, the volumetric properties of SiO_2 liquid are dominated by configurational effects (Part I). Secondly, the structure of $Si^{IV}O_2$ liquid is different than the structural environment of $Si^{IV}O_2$ in a multicomponent silicate melt, as the addition of alkali and alkali-earth oxides are known from spectroscopic studies to depolymerize the liquid (for example, Mysen, 1988; Stebbins, 1995; Wolf and McMillan, 1995).

The modeled volumetric consequences of configurational collapse associated with (Al,Si)[IV] → (Al,Si)[V] coordination change in the melt show some interesting systematics (table 2). For $Mg_2Si_2O_6$, $CaMgSi_2O_6$, and $CaAl_2Si_2O_8$ liquid the transformation induces ~11 percent increase in melt density, irregardless of the pressure dependence of the coordination shift. For SiO_2 and $Na_2Si_4O_9$ liquid the effect is ~17 percent and for $NaAlSiO_4$, $NaAlSi_2O_6$, and $NaAlSi_3O_8$ liquid it is ~27 percent. It is tempting to associate the percentage collapse with the intrinsic volume of the oxygen coordination polyhedra about the cation, but this treatment would be an over simplification. The molecular dynamics simulations discussed above document that changes in CN of the alkali and alkali earth cations accompany CN changes for Al and Si. Additionally, the long-range (beyond nearest neighbor) structure of the melt must respond to short-range structural changes (Xue and others, 1991), so the volumetric response is the cumulative effect of both contributions. The analysis developed here argues for a greater configurational collapse in highly polymerized melts (SiO_2) and melts of the alkali metal silicates and less so in depolymerized melts of the orthosilicactes. Perhaps these constraints might prove useful to the interpretation of volume changes associated with "Q-species" reactions, which have been called upon as a mechanism for pressure-induced coordination number transformations (Xue and others, 1991; Wolf and McMillan, 1995).

Model density changes associated with (Al,Si)[V] → (Al,Si)[VI] are not as well constrained from MD work, largely because the abundance of (Al,Si)[IV] is not high enough in most of the systems studied to adequately assess the effect on density. The best estimates can be made on $CaAl_2Si_2O_8$ and SiO_2 liquids, where the effect is 10 percent and 5 percent respectively.

Except as noted above, for liquid compositions analyzed in this paper there is agreement between the modeled reference pressure volumetric quantities of Part II and available constraints on melt density at elevated pressure. This agreement suggests that it may be possible to obtain an internally consistent set of high-pressure model EOS parameters that permit densities of multicomponent silicate liquids to be estimated at pressures up to ~40 GPa. An exercise of this kind requires development of parameter mixing relations and some systematic approach to modeling the compositional dependence of configurational contributions to the liquid volume. Fortunately,

additional experimental constraints on the densities of multicomponent melts at elevated pressure are available. These are static compression studies performed in both piston cylinder and multi-anvil apparatus, where density of the liquid is estimated using the mineral sink-float method. In the next and final paper in this series, these data will be analyzed in combination with the data sets reviewed here with the objective of obtaining mixing relations for the higher order parameters of the proposed EOS and a practical algorithm to use for magmatic composition liquids.

ACKNOWLEDGMENTS

Thoughtful discussions with Victor Kress and Frank Spera helped enormously in developing the arguments presented in this paper. Material support for this investigation was generously provided by the National Science Foundation (OCE-9977416 and EAR-9980518) and The University of Chicago.

References

Agee, C. B., 1992a, Isothermal compression of molten Fe_2SiO_4: Geophysical Research Letters, v. 19, p. 1169-1172.

——— 1992b, Thermal expansion of molten Fe_2SiO_4 at high pressure: Geophysical Research Letters, v. 19, p. 1173-1176.

——— 1998, Crystal-liquid density inversions in terrestrial and lunar magmas: Physics of the Earth and Planetary Interiors, v. 107, p. 63-74.

Akimoto, S. I., Komada, E., and Kushiro, I., 1967, Effect of pressure on the melting of olivine and spinel polymorph of Fe_2SiO_4: Journal of Geophysical Research, v. 72, p. 679-686.

Allen, M. P., and Tildesley, D. J., 1987, Computer Simulation of Liquids: Oxford, Clarendon Press, 385 p.

Anderson, D. L., 1989, Theory of the Earth: Boston, Blackwell Scientific Publications, 366 p.

Andrault, D., Bouhifd, M. A., Itié, J. P., and Richet, P., 1995, Compression and amorphization of $(Mg,Fe)_2SiO_4$ olivines: An X-ray diffraction study up to 70 GPa: Physics and Chemistry of Minerals, v. 22, p. 99-107.

Angell, C. A., Cheeseman, P. A., and Kadiyala, R. R., 1987, Diffusivity and thermodynamic properties of diopside and jadeite melts by computer simulation studies: Chemical Geology, v. 62, p. 83-92.

Angel, R. J., and Hugh-Jones, D. A., 1994, Equations of state and thermodynamic properties of enstatite pyroxenes: Journal of Geophysical Research, v. 99, p. 19777-19783.

Anovitz, L. M., and Blencoe, J. G., 1999, Dry melting of albite: American Mineralogist, v. 84, p. 1830-1842.

Bacon, J. F., Hasapis, A. A., and Wholley, J. W., Jr., 1960, Viscosity and density of molten silica and high silica content glasses: Physics and Chemistry of Glasses, v. 1, p. 90-98.

Bell, P. M., and Roseboom, E. H., Jr., 1969, Melting relationships of jadeite and albite to 45 kilobars with comments on melting diagrams of binary systems at high pressures: Mineralogical Society of America Special Paper, v. 2, p. 151-161.

Belonoshko, A. B., and Dubrovinsky, L. S., 1996, Molecular and lattice dynamics study of the MgO-SiO_2 system using a transferable interatomic potential: Geochimica et Cosmochimica Acta, v. 60, p. 1645-1656.

Berman, R. G., 1988, Internally-consistent thermodynamic data for minerals in the system Na_2O-K_2O-CaO-MgO-FeO-Fe_2O_3-Al_2O_3-SiO_2-TiO_2-H_2O-CO_2: Journal of Petrology, v. 29, p. 445-522.

Berman, R. G., and Brown, T. H., 1985, Heat capacity of minerals in the system Na_2O-K_2O-CaO-MgO-FeO-Fe_2O_3-Al_2O_3-SiO_2-TiO_2-H_2O-CO_2: representation, estimation, and high temperature extrapolation: Contributions to Mineralogy and Petrology, v. 89, p. 168-183.

Birch, F., 1966, Compressibility; elastic constants, *in* Clark, S. P., Jr., Handbook of Physical Constants: Memoir of the Geological Society of America, v. 97, p. 97-173.

Birch, F., and LeComte, P., 1960, Temperature-pressure plane for albite composition: American Journal of Science, v. 258, p. 209-217.

Boettcher, A. L., Burnham, C. W., Windom, K. E., and Bohlen, S. R., 1982, Liquids, glasses, and the melting of silicates to high-pressures: Journal of Geology, v. 90, p. 127-138.

Bottinga, Y., 1985, On the isothermal compressibility of silicate liquids at high pressure: Earth and Planetary Science Letters, v. 74, p. 350-360.

Bouhifd, M. A., Andrault, D., Fiquet, G., and Richet, P., 1996, Thermal expansion of forsterite up to the melting point: Geophysical Research Letters, v. 23, p. 1143-1146.

Boyd, F. R., and England, J. L., 1962, Mantle minerals: Carnegie Institution of Washington Yearbook, v. 61, p. 107-112.

——— 1963, Effect of pressure on the melting of diopside, $CaMgSi_2O_6$, and albite, $NaAlSi_3O_8$, in the range up to 50 kilobars: Journal of Geophysical Research, v. 68, p. 311-323.

Boyd, F. R., England, J. L., and Davis, B. T. C., 1964, Effects of pressure on the melting and polymorphism of enstatite, $MgSiO_3$: Journal of Geophysical Research, v. 69, p. 2101-2109.

Brodholt, J., Patel, A., and Refson, K., 1996, An ab initio study of the compressional behavior of forsterite: American Mineralogist, v. 81, p. 257-260.

Bryce, J. G., Spera, F. J., and Stein, D. J., 1997, Dependence of self diffusivity on P and T in molten $NaAlSi_2O_6$: Comparison of laboratory and molecular dynamics experiments: Geophysical Research Letters, v. 24, p. 711-714.

——— 1999, Pressure dependence of self-diffusion in the $NaAlO_2$-SiO_2 system: Compositional effects and mechanisms: American Mineralogist, v. 84, p. 345-356.

Cameron, M., Sueno, S., Prewitt, C. T., and Papike, J. J., 1973, High-temperature crystal chemistry of acmite, diopside, hedenbergite, jadeite, spodumene, and Ureyite: American Mineralogist, v. 58, p. 594-618.

Carmichael, I. S. E., and Ghiorso, M. S., 1986, Oxidation-reduction relations in basic magma: a case for homogeneous equilibria: Earth and Planetary Science Letters, v. 78, p. 200-210.

Chen, C. H., and Presnall, D. C., 1975, The system Mg_2SiO_4 – SiO_2 at pressures up to 25 kbars: American Mineralogist, v. 60, p. 398-406.

Chen, G. Q., Ahrens, T. J., and Stolper, E. M., 2002, Shock-wave equation of state of molten and solid fayalite: Physics of the Earth and Planetary Interiors, v. 134, p. 35-52.

Davis, B. T. C., and England, J. L., 1964, The melting of forsterite up to 50 kilobars: Journal of Geophysical Research, v. 69, p. 1113-1116.

Diefenbacher, J., McMillan, P. F., and Wolf, G. H., 1998, Molecular dynamics simulations of $Na_2Si_4O_9$ liquid at high pressure: Journal of Physical Chemistry B, v. 102, p. 3003-3008.

Dingwell, D. B., 1992, Density of some titanium-bearing silicate liquids and the compositional dependence of the partial molar volume of TiO_2: Geochimica et Cosmochimica Acta, v. 56, p. 3403-3407.

Downs, R. T., Zha, C. S., Duffy, T. S., and Finger, L. W., 1996, The equation of state of forsterite to 17.2 GPa and effects of pressure media: American Mineralogist, v. 81, p. 51-55.

Duffy, T. S., and Wang, Y., 1998, Pressure-volume-temperature equations of state, *in* Hemley, R. J., editor, Ultrahigh-pressure Mineralogy: Physics and Chemistry of the Earth's Deep Interior, Reviews in Mineralogy, v. 37, p. 425-457.

Fabrichaya, O. B., and Sundman, B., 1997, The assessment of thermodynamic parameters in the Fe-O and Fe-Si-O systems: Geochimica et Cosmochimica Acta, v. 61, p. 4539-4555.

Farges, F., 1997, Coordination of Ti^{4+} in silicate glasses: A high-resolution XANES spectroscopy study at the Ti *K* edge: American Mineralogist, v. 82, p. 36-43.

Finger, L. W., and Ohashi, Y., 1976, The thermal expansion of diopside to 800 °C and a refinement of the crystal structure at 700 °C: American Mineralogist, v. 61, p. 303-310.

Gasparik, T., 1996, Melting experiments on the enstatite-diopside join at 70-224 kbar, including the melting of diopside: Contributions to Mineralogy and Petrology, v. 124, p. 139-153.

Ghiorso, M. S., 1999, On the stability relations of hydrous minerals in water-undersaturated magmas: American Mineralogist, v. 84, p. 1506-1511.

——— 2004a, An Equation of State for Silicate Melts. I. Formulation of a General Model: American Journal of Science, v. 304, p. 637–678.

——— 2004b, An Equation of State for Silicate Melts. IV. Calibration of a multicomponent mixing model to 40 Gpa: American Journal of Science, v. 304, p. 811–838.

Ghiorso, M. S., and Kress, V. C., 2004, An Equation of State for Silicate Melts. II. Calibration of volumetric properties at 10^5 Pa: American Journal of Science, v. 304, p. 679–751.

Goldsmith, J. R., 1980, The melting and breakdown reactions of anorthite at high pressures and temperatures: American Mineralogist, v. 65, p. 272-284.

Hariya, Y., and Kennedy, G. C., 1968, Equilibrium study of anorthite under high pressure and high temperature: American Journal of Science, v. 266, p. 193-203.

Hazen, R. M., 1976, Effects of temperature and pressure on the crystal structure of forsterite: American Mineralogist, v. 61, p. 1280-1293.

——— 1977, Effects of temperature and pressure on the crystal structure of ferromagnesian olivine: American Mineralogist, v. 62, p. 286-295.

Hazen, R. M., and Finger, L.W., 1978, Crystal structures and compressibilities of pyrope and grossular to 60 kbar: American Mineralogist, v. 63, p. 297-303.

Herzberg, C. T., 1987a, Magma density at high pressure Part 1: The effect of composition on the elastic properties of silicate melts, *in* Mysen, B. O., editor, Magmatic Processes: Physiochemical Principles: Geochemical Society Special Publication, v. 1, p. 25-46.

——— 1987b, Magma density at high pressure Part 2: A test of the olivine floatation hypothesis, *in* Mysen, B. O., editor, Magmatic Processes: Physiochemical Principles: Geochemical Society Special Publication, v. 1, p. 47-58.

Hsu, L. C., 1967, Melting of fayalite up to 40 kilobars: Journal of Geophysical Research, v. 72, p. 4235-4244.

Hudon, P., Jung, I. H., and Baker, D. R., 2002, Melting of β-quartz up to 2.0 GPa and thermodynamic optimization of the silica liquidus up to 6.0 Gpa: Physics of the Earth and Planetary Interiors, v. 130, p. 159-174.

Hugh-Jones, D., 1997, Thermal expansion of $MgSiO_3$ and $FeSiO_3$ ortho- and clinopyroxenes: American Mineralogist, v. 82, p. 689-696.

Hugh-Jones, D. A., and Angel, R. J., 1994, A compressional study of $MgSiO_3$ orthoenstatite up to 8.5 Gpa: American Mineralogist, v. 79, p. 405-410.

Hugoniot, H., 1889, Sur la propagation du mouvement dans les corps et spécialement dans les gaz parfaits. Deuxième Partie. Chapitre v., Sur les discontinuities qui se maniffestent dans la propagation du movement: Journal de l"Ecole polytechnique, v. 58, p. 68-125.

Irifune, T., and Ohtani, E., 1986, Melting of pyrope $Mg_3Al_2Si_3O_{12}$ up to 10 GPa: Possibility of a pressure-induced structural change in pyrope melt: Journal of Geophysical Research, v. 91, p. 9357-9366.

Isaak, D. G., Anderson, O. L., Goto, T., and Suzuki, I., 1989, Elasticity of single-crystal forsterite measured to 1700 K: Journal of Geophysical Research, v. 94, p. 5895-5906.

Kanzaki, M., 1990, Melting of silica up to 7 Gpa: Journal of the American Ceramic Society, v. 73, p. 3706-3707.
Kato, T., and Kumazawa, M., 1985a, Stability of Phase B, a hydrous magnesium silicate, to 2300 °C at 20 Gpa: Geophysical Research Letters, v. 12, p. 534-535.
——— 1985b, Effect of high pressure on the melting relation in the system Mg_2SiO_4-$MgSiO_3$ Part I. Eutectic relation up to 7 Gpa: Journal of the Physics of the Earth, v. 33, p. 513-524.
——— 1986, Melting and phase relations in the system Mg_2SiO_4 – $MgSiO_3$ at 20 GPa under hydrous conditions: Journal of Geophysical Research, v. 91, p. 9351-9355.
Kress, V. C., Williams, Q., and Carmichael, I. S. E., 1988, Ultrasonic investigation of melts in the system Na_2O-Al_2O_3-SiO_2: Geochimica et Cosmochimica Acta, v. 52, p. 283-293.
Kubicki, J. D., and Lasaga, A. C., 1991, Molecular dynamics simulations of pressure and temperature effects on $MgSiO_3$ and Mg_2SiO_4 melts and glasses: Physics and Chemistry of Minerals, v. 17, p. 661-673.
Kudoh, Y., and Takeda, H., 1986, Single crystal X-ray diffraction study on the bond compressibility of fayalite, Fe_2SiO_4 and rutile, TiO_2 under high pressure: Physica B, v. 139/140, p. 333-336.
Kudoh, Y., and Takéuchi Y., 1985, The crystal structure of forsterite Mg_2SiO_4 under high pressure up to 149 kb: Zeitschrift für Kristallographie, v. 171, p. 291-302.
Lange, R. A., 2003, The fusion curve of albite revisited and the compressibility of $NaAlSi_3O_8$ liquid with pressure: American Mineralogist, v. 88, p. 109-120.
Lange, R. A., and Carmichael, I. S. E., 1987, Densities of Na_2O-K_2O-CaO-MgO-FeO-Fe_2O_3-Al_2O_3-TiO_2-SiO_2 liquids: New measurements and derived partial molar properties: Geochimica et Cosmochimica Acta, v. 51, p. 2931-2946.
——— 1990, Thermodynamic properties of silicate liquids with emphasis on density, thermal expansion and compressibility, *in* Nicholls, J., and Russell, J. K., editors, Modern Methods of Igneous Petrology: Understanding Magmatic Processes, Reviews in Mineralogy, v. 24, p. 25-64.
Lange, R. A., and Navrotsky, A., 1992, Heat capacities of Fe_2O_3-bearing silicate liquids: Contributions to Mineralogy and Petrology, v. 110, p. 311-320.
Lange, R. A., de Yoreo, J. J., and Navrotsky, A., 1991, Scanning calorimetric measurement of heat capacity during incongruent melting of diopside: American Mineralogist, v. 76, p. 904-912.
Leger, J. M., Redon, A. M., and Chateau C., 1990, Compressions of synthetic pyrope, spessartine and uvarovite garnets up to 25 GPa: Physics and Chemistry of Minerals, v. 17, p. 161-167.
Levien, L., and Prewitt, C. T., 1981, High-pressure structural study of diopside: American Mineralogist, v. 66, p. 315-323.
Lindsley, D. H., 1966, P-T projection for part of the system kalsilite-silica: Carnegie Institution of Washington Yearbook, v. 65, p. 244-247.
——— 1967, Pressure-temperature relations in the system FeO-SiO_2: Carnegie Institution of Washington Yearbook, v. 66, p. 226-230.
Liu, Q., and Lange, R. A., 2001, The partial molar volume and thermal expansivity of TiO_2 in alkali silicate melts: Systematic variation with Ti coordination: Geochimica et Cosmochimica Acta, v. 65, p. 2379-2393.
Matsui, M., 1996, Molecular dynamics simulation of structures, bulk moduli, and volume thermal expansivities of silicate liquids in the system CaO-MgO-Al_2O_3-SiO_2: Geophysical Research Letters, v. 23, p. 395-398.
Matsui, T., and Manghnani, M. H., 1985, Thermal expansion of single-crystal forsterite to 1023 K by Fizeau interferometry: Physics and Chemistry of Minerals, v. 12, p. 201-210.
Meagher, E. P., 1975, The crystal structures of pyrope and grossularite at elevated temperatures: American Mineralogist, v. 60, p. 218-228.
Miller, G. H., Stolper, E. M., and Ahrens, T. J., 1991, The equation of state of a molten komatiite 1. Shock wave compression to 36 GPa: Journal of Geophysical Research, v. 96, p. 11831-11848.
Morgan, N. A., and Spera, F. J., 2001a, Glass transition, structural relaxation, and theories of viscosity: A molecular dynamics study of amorphous $CaAl_2Si_2O_8$: Geochimica et Cosmochimica Acta, v. 65, p. 4019-4041.
——— 2001b, A molecular dynamics study of the glass transition in $CaAl_2Si_2O_8$: Thermodynamics and tracer diffusion: American Mineralogist, v. 86, p. 915-926.
Morse, S. A., 1980, Basalts and Phase Diagrams: New York, Springer-Verlag, 493 p.
Mysen, B. O., 1988, Structure and Properties of Silicate Melts: New York, Elsevier, 354 p.
Nekvasil, H., and Carroll, W., 1996, Experimental constraints on the compositional evolution of crustal magmas: Transactions of the of the Royal Society of Edinburgh-Earth Sciences, v. 87, p. 139-146.
Nevins, D., and Spera, F. J., 1998, Molecular dynamics simulations of molten $CaAl_2Si_2O_8$: Dependence of structure and properties at pressure: American Mineralogist, v. 83, p. 1220-1230.
Ohtani, E., 1979, Melting relation of Fe_2SiO_4 up to 200 kbar: Journal of the Physics of the Earth, v. 27, p. 189-208.
Ohtani, E., and Kumazawa, M., 1981, Melting of forsterite Mg_2SiO_4 up to 15 GPa: Physics of the Earth and Planetary Interiors, v. 27, p. 32-38.
Ohtani, E., Irifune, T., and Fujino, K., 1981, Fusion of pyrope at high pressures and rapid crystal growth from the pyrope melt: Nature, v. 294, p. 62-64.
Olinger, B., 1977, Compression studies of forsterite (Mg_2SiO_4) and enstatite ($MgSiO_3$), *in* Manghnani, M. H., and Akimoto, S. I., editors, High Pressure Research. Applications in Geophysics: San Diego, Academic Press, p. 325-334.
Plymate, T. G., and Stout, J. H., 1990, Pressure-volume-temperature behavior of fayalite based on static compression measurements at 400° C: Physics and Chemistry of Minerals, v. 17, p. 212-219.
Presnall, D., and Walter, M. J., 1993, Melting of forsterite, Mg_2SiO_4, from 9.7 to 16.5 GPa: Journal of Geophysical Research, v. 98, p. 19777-19783.

Presnall, D. C., and Gasparik, T., 1990, Melting of enstatite ($MgSiO_3$) from 10 to 16.5 GPa and the forsterite (Mg_2SiO_4) - majorite ($MgSiO_3$) eutectic at 16.5 GPa: Implications for the origin of the mantle: Journal of Geophysical Research, v. 95, p. 15771-15777.

Ralph, R. L., Hazen, R. M., and Finger, L.W., 1982, Cell parameters of orthoenstatite at high temperature and pressure: Carnegie Institution of Washington, Yearbook 81, 376-379.

Richet, P., 1993, Melting of forsterite and spinel, with implications for the glass transition of Mg_2SiO_4 liquid: Geophysical Research Letters, v. 20, p. 1675-1678.

Richet, P., and Bottinga, Y., 1984a, Anorthite, andesine, wollastonite, diopside, cordierite and pyrope: thermodynamics of melting, glass transitions, and properties of the amorphous phases: Earth and Planetary Science Letters, v. 67, p. 415-432.

——— 1984b, Glass transitions and thermodynamic properties of amorphous SiO_2, $NaAlSi_nO_{2n+2}$ and $KAlSi_3O_8$: Geochimica et Cosmochimica Acta, v. 48, p. 453-470.

——— 1986, Thermochemical properties of silicate glasses and liquids: A review: Reviews in Geophysics, v. 24, p. 1-25.

Richet, P., Bottinga, Y., Denielou, L., Petitet, J. P., and Tequi, C., 1982, Thermodynamic properties of quartz, cristobalite and amorphous SiO_2: Drop calorimetry measurements between 1000 K and 1800 K and a review from 0 K to 2000 K: Geochimica et Cosmochimica Acta, v. 46, p. 2639-2658.

Richet, P., Mysen, B. O., and Ingrin, J., 1998, High-temperature X-ray diffraction and Raman spectroscopy of diopside and pseudowollastonite: Physics and Chemistry of Minerals, v. 25, p. 401-414.

Rigden, S. M., Ahrens, T. J., and Stolper, E. M., 1984, Densities of liquid silicates at high pressures: Science, v. 226, p. 1071-1074.

——— 1988, Shock compression of molten silicate: Results for a model basaltic composition: Journal of Geophysical Research, v. 93, p. 367-382.

——— 1989, High-pressure equation of state of molten anorthite and diopside: Journal of Geophysical Research, v. 94, p. 9508-9522.

Rowan, L. R., ms, 1993, Equation of state of molten Mid-Ocean Ridge Basalt: Ph.D. thesis, California Institute of Technology, 86 p.

Rustad, J. R., Yuen , D. A., and Spera, F. J., 1990, Molecular dynamics of liquid SiO_2 under high pressure: Physical Rreview A, v. 42, p. 2081-2089.

——— 1991a, Molecular dynamics of amorphous silica at very high pressures (135 GPa): Thermodynamics and extraction of structures through analysis of Voronoi polyhedra: Physical Review B, v. 44, p. 2108-2121.

——— 1991b, The sensitivity of physical and spectral properties of silica glass to variations of interatomic potentials under high pressure: Physics of the Earth and Planetary Interiors, v. 65, p. 210-230.

Sack, R. O., and Ghiorso, M. S., 1998, Thermodynamics of feldspathoid solutions: Contributions to Mineralogy and Petrology, v. 130, p. 256-274.

Saxena, S. K., Chatterjee, N., Fei, Y., and Shen, G., 1993, Thermodynamic Data on Oxides and Silicates. An assessed data set based on thermochemistry and high pressure phase equilibrium: New York, Springer-Verlag, 428 p.

Scarfe, C. M., and Takahashi, E., 1986, Melting of garnet peridotite to 13 GPa and the early history of the upper mantle: Nature, v. 322, p. 354-356.

Shinmei, T., Tomioka, N., Fujino, K., Kuroda, K., and Irifune, T., 1999, In situ X-ray diffraction study of enstatite up to 12 GPa and 1473 K and equations of state: American Mineralogist, v. 84, p. 1588-1594.

Shiraishi, Y., Ikeda, K., Tamura, A., and Saitô, T., 1978, On the viscosity and density of the molten FeO-SiO_2 system: Transactions of the Japanese Institute of Metallurgy, v. 19, p. 264-274.

Skinner, B. J., 1956, Physical properties of end-members of the garnet group: American Mineralogist, v. 41, p. 428-436.

——— 1966, Thermal expansion, *in* Clark, S. P., Jr., Handbook of Physical Constants: Memoir of the Geological Society of America, v. 97, p. 75-96.

Smith, P., ms, 2003, The melting curve of nepheline: Ph.D. Dissertation, University of Cambridge, 256 p.

Stebbins, J. F., 1991, NMR evidence for five-coordinated silicon in a silicate glass at atmospheric pressure: Nature, v. 351, p. 638-639.

——— 1995, Dynamics and structure of silicate and oxide melts: Nuclear magnetic resonance studies, *in* Stebbins, J. F., McMillan, P. F., and Dingwell, D. B., Structure, dynamics and properties of silicate melts: Reviews in Mineralogy, v. 32, p. 191-246.

Stebbins, J. F., and Farnan, I., 1992, Effects of high temperature on silicate liquid structure: A multinuclear NMR study: Science, v. 255, p. 586-589.

Stebbins, J. F., and Sykes, D., 1990, The structure of NaAlSi3O8 liquids at high pressure: new constraints from NMR spectroscopy: American Mineralogist, v. 75, p. 943-946.

Stebbins, J. F., Carmichael, I. S. E., and Weill, D. E., 1983, The high temperature liquid and glass heat contents and the heats of fusion of diopside, albite, sanidine and nepheline: American Mineralogist, v. 68, p. 717-730.

Stebbins, J. F., Carmichael, I. S. E., and Moret, L. K., 1984, Heat capacities and entropies of silicate liquids and glasses: Contributions to Mineralogy and Petrology, v. 86, p. 131-148.

Stein, D. J., and Spera, F. J., 1995, Molecular dynamics simulations of liquids and glasses in the system $NaAlSiO_4$-SiO_2: Methodology and melt structures: American Mineralogist, v. 80, p. 417-431.

——— 1996, Molecular dynamics simulations of liquids and glasses in the system $NaAlSiO_4$-SiO_2: Physical properties and transport mechanisms: American Mineralogist, v. 81, p. 284-302.

Sumino, Y., 1979, The elastic constants of Mn_2SiO_4, Fe_2SiO_4 and Co_2SiO_4, and the elastic properties of olivine group minerals at high temperature: Journal of the Physics of the Earth, v. 27, p. 209-238.

Suzuki, I., Seya, K., Takei, H., and Sumino, Y., 1981, Thermal expansion of fayalite, Fe_2SiO_4: Physics and Chemistry of Minerals, v. 7, p. 60-63.

Tanaka, H., 2000, General view of a liquid-liquid phase transition: Physical Review B, v. 62, p. 6968-6976.
Tangeman, J., and Xirouchakis, D., 1999, High-temperature heat capacity and thermodynamic properties for end-member titanite ($CaTiSiO_5$): Physics and Chemistry of Minerals, v. 28, p. 167-176.
Tequi, C., Robie, R. A., Hemingway, B. S., Neuville, D. R., and Richet, P., 1991, Melting and thermodynamic properties of pyrope ($Mg_3Al_2Si_3O_{12}$): Geochimica et Cosmochimica Acta, v. 55, p. 1005-1010.
Thiéblot, L., Roux, J., and Richet, P., 1998, High-temperature thermal expansion and decomposition of garnets: European Journal of Mineralogy, v. 10, p. 7-15.
Tribaudino, M., Precipe, M., Bruno, M., and Levy , D., 2000, High-pressure behavior of Ca-rich *C2/c* clinopyroxenes along the join diopside-enstatite ($CaMgSi_2O_6$-$Mg_2Si_2O_6$): Physics and Chemistry of Minerals, v. 27, p. 656-664.
Vinet, P., Ferrante, J., Smith, J. R., and Rose, J. H., 1986, A universal equation of state for solids: Journal of Physics C: Solid State Physics, v. 19, p. L467-L473.
Vinet P., Smith, J. R., Ferrante J., and Rose J. H., 1987, Temperature effects on the universal equation of state of solids, Physical Review B, v. 35, p. 1945-1953.
Vinet, P., Rose, J. H., Ferrante, J., and Smith, J. R., 1989, Universal features of the equation of state of solids: Journal of Physics: Condensed Matter, v. 1, p. 1941-1963.
Waff, H. S., 1975, Pressure-induced coordination changes in silicate liquids: Geophysical Research Letters, v. 2, p. 193-196.
Walker, D., Agee, C. B., and Zhang, Y., 1988, Fusion curve slope and crystal/liquid buoyancy: Journal of Geophysical Research, v. 93, p. 313-323.
Wasserman, E. A., Yuen, D. A., Rustad, J. R., 1993a, Compositional effects on the transport and thermodynamic properties of MgO-SiO_2 mixtures using molecular dynamics: Physics of the Earth and Planetary Interiors, v. 77, p. 189-203.
——— 1993b, Molecular dynamics study of the transport properties of perovskite melts under high temperature and pressure conditions: Earth and Planetary Sciences Letters, v. 114, p. 373-384.
Waterweise, T., Chatterjee, N. D., Dierdorf, I., Göttlicher, J., and Kroll, H., 1995, Experimental and thermodynamic study of homogeneous and heterogeneous equilibria in the system $NaAlSiO_4$-SiO_2: Contributions to Mineralogy and Petrology, v. 121, p. 61-73.
Weill, D. F., Hon, R., and Navrotsky, A., 1980, The igneous system $CaMgSi_2O_6$-$CaAl_2Si_2O_8$-$NaAlSi_3O_8$; variations on a classic theme by Bowen, *in* Hargraves, R. B., editor, Physics of Magmatic Processes: Princeton, New Jersey, Princeton University Press, p. 49-92.
Will, G., Hoffbauer, W., Hinze, E., and Lauterjung, J., 1986, The compressibility of forsterite up to 300 kbar measured with synchrotron radiation: Physica B, v. 139/140, p. 193-197.
Williams, D. W., and Kennedy, G. C., 1969, Melting curve of diopside to 50 kilobars: Journal of Geophysical Research, v. 74, p. 4359-4366.
Williams, Q., Knittle, E., Reichlin, R., Martin, S., and Jeanloz, R., 1990, Structural and electronic properties of Fe_2SiO_4-fayalite at ultrahigh pressures: Amorphization and gap closure: Journal of Geophysical Research, v. 95, p. 21549-21563.
Wolf, G. H., and McMillan, P. F., 1995, Pressure effects on silicate melt structure and properties, *in* Stebbins, J. F., McMillan, P. F., and Dingwell, D. B., editors, Structure, Dynamics and Properties of Silicate Melts: Reviews in Mineralogy, v. 32, p. 505-561.
Xue, X., Stebbins, J. F., Kanzaki, M., McMillan, P. F., and Poe, B., 1991, Pressure-induced silicon coordination and tetrahedral structural changes in alkali oxide-silica melts up to 12 GPa: NMR, Raman, and infrared spectroscopy: American Mineralogist, v. 76, p. 8-26.
Yagi , T., Ida Y., Sato Y., and Akimoto S. I., 1975, Effect of hydrostatic pressure on the lattice parameters of Fe_2SiO_4 olivine up to 70 kbar: Physics of the Earth and Planetary Interiors, v. 10, p. 348-354.
Yagi, T., Akaogi, M., Shimomura, O., Suzuki, T., and Akimoto, S. I., 1987, In situ observation of the olivine-spinel phase transformation in Fe_2SiO_4 using synchrotron radiation: Journal of Geophysical Research, v. 92, p. 6207-6213.
Yang, H., and Ghose, S., 1994, Thermal expansion, Debye temperature and Grüneisen parameter of synthetic (Fe,Mg)SiO_3 orthopyroxenes: Physics and Chemistry of Minerals, v. 20, p. 575-586.
Yoneda, A., 1996, Complete thermodynamic analysis on Hugoniots: Physics of the Earth and Planetary Interiors, v. 96, p. 129-134.
Zha, C. S., Duffy, T. S., Downs, R. T., Mao, H. K., and Hemley, R. J., 1996, Sound velocity and elasticity of single crystal forsterite to 16 GPa: Journal of Geophysical Research, v. 101, p. 17535-17545.
Zhang, J., Liebermann, R. C., Gasparik, T., Herzberg, C. T., and Fei, Y., 1993, Melting and subsolidus relations of SiO_2 at 9-14 GPa: Journal of Geophysical Research, v. 98, p. 19785-19793.
Zhang, L., 1998, Single crystal hydrostatic compression of (Mg, Mn, Fe, Co)$_2SiO_4$ olivines: Physica, v. 25, p. 308-312.
Zhang, L., Ahsbahs, H., Hayner, S. S., and Kutoglu, A., 1997, Single-crystal compression and crystal structure of clinopyroxene up to 10 GPa: American Mineralogist, v. 82, p. 245-258.
Zhang, L., Ahsbahs, H., and Kutoglu, A., 1998, Hydrostatic compression and crystal structure of pyrope to 33 GPa: Physics and Chemistry of Minerals, v. 25, p. 301-307.
Zhao, Y., Schiferl, D., and Shankland, T. J., 1995, A high P-T single-crystal X-ray diffraction study of thermoelasticity of $MgSiO_3$ orthoenstatite: Physics and Chemistry of Minerals, v. 21, p. 393-398.
Zhou, Y., and Miller, G. H., 1997, Constraints from molecular dynamics on the lquidus and solidus of the lower mantle: Geochimica et Cosmochimica Acta, v. 61, p. 2957-2976.